

UNIVERSITÁ DEGLI STUDI DI PADOVA

ALBERTO MENEGHIN

**Three-objective optimization
studies of an S-duct**

DIPARTIMENTO DI INGEGNERIA INDUSTRIALE

MSC IN AEROSPACE ENGINEERING

MSC THESIS

Academic Year: 2019-2020

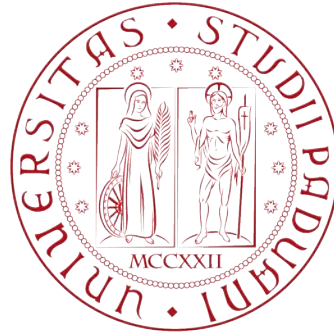
Supervisors:

Prof. Ernesto BENINI

Dr. Timoleon KIPOUROS

April 2020

UNIVERSITÁ DEGLI STUDI DI PADOVA



MSC IN AEROSPACE ENGINEERING

MSC THESIS

Academic Year: 2019-2020

ALBERTO MENEGHIN

Three-objective optimization studies of an S-duct

Supervisors:

Prof. Ernesto BENINI

Dr. Timoleon KIPOUROS

April 2020

© Università degli Studi di Padova, 2020.

Abstract

Dipartimento di Ingegneria Industriale

MSc in Aerospace Engineering

Three-objective optimization studies of an S-duct

by Alberto MENEGHIN

Nowadays the CFD analysis has become one of the most reliable tool that an engineer can use to study the evolution of the flow field. Furthermore, thanks to the evolution of the computer and the increasing computing power, Multi-Objective Optimisation problem can be now solved in less time. In this work the CFD analysis and the MOO are combined. In particular the MOO is focused on the optimisation of an S-duct intake while the CFD analysis is a study of the interaction between different s-duct, obtained by the MOO, with the rotor 67. The S-duct intake create inlet distorsions to the fan and many studies have been done to replicate these inlet distorsions. In literature total pressure and swirl distorsion are analysed separatly but in reality the two distorsions coesist together and the main problem of the automatic generation of inlet distorsions is recreate the two distorsions combined. On the other hand, in this thesis a full cfd simulation is conducted. Since the distorsions involve swirl and total pressure a single blade simulation does not describe the full phenomenon but instead a full annulus simulation is required. The first CFD simulation presented in Chapter 7 focus on the S-duct intake studied by Delot but adapted to the geometrical requirement of the fan. This simulation shows the evolution of the two counter-rotating vortices and that the performance of the transonic fan drastically decrease. The two counter-rotating vortices, under the influence of the rotational speed of the fan, merge together generating a single vortex that negatively affect the velocity field. This simulation will be used as reference. In Chapter 6 three MOO are presented. The main difference from the previous studies conducted, is that the first two optimisations have a new objective function that has been created. This new function, called Symmetry Maximum Error (S.M.E.) and described in Chapter 4, has the goal to minimise the total pressure difference between the

upper and the lower part of the S-duct. The last optimisation instead was done by [1]. In Chapter 8 are reported the results from the different CFD analysis with the optimised S-ducts. The results show that different S-ducts provide better inlet conditions for the fan. In particular different vortices structure, position, strength and distance are analysed. The results show that the optimisation of the S.M.E. increased the performance of the fan and reduce the total pressure losses on the S-duct.

SOMMARIO

Il lavoro condotto durante questi sei mesi presso l'Università di Cranfield è incentrato sull'analisi dell'interazione tra una presa dinamica a forma di S e un fan transonico. In questo studio, il fan transonico viene fornito dalla NASA ed è il test case R67, mentre le differenti geometrie dell'S-duct sono state ottenute tramite un processo di ottimizzazione. La prima geometria analizzata è la S-duct scalata di Delot ed è stata utilizzata come punto di riferimento per le altre geometrie. Dalle simulazioni CFD riportate nel Capitolo 7 si può notare come i due vortici creati dall'S-duct si fondano, sotto l'influenza del campo di moto del rotore, e creino un singolo vortice che ruota in senso orario. Oltre alla geometria di Delot, altre otto geometrie sono state analizzate. Queste ultime sono state ottenute tramite un processo di ottimizzazione utilizzando una nuova funzione oggetto appositamente creata per ridurre le distorsioni in ingresso. Questa nuova funzione oggetto ha lo scopo di minimizzare la differenza di pressione totale tra la parte superiore ed inferiore della presa dinamica all'AIP ed è descritta nel Capitolo 4. Nel Capitolo 6 sono riportate le otto differenti geometrie ottenute dall'ottimizzazione. Infine nel Capitolo 8 sono riportati i risultati delle diverse simulazioni CFD con le otto S-duct. I risultati ottenuti dimostrano come diversi tipi di vortici influenzano il campo di moto del rotore. In particolare numero, taglia e distanza dei vortici sono elementi determinanti per le prestazioni del rotore.

Acknowledgements

I would like to thank my supervisor Dr. Timoleon Kipouros, for the advice provided during the project and to gave me the opportunity to work in the challenging field of Design Engineering. A big thank you goes to Mattia, Luca and Andrea without whom this experience wouldn't have been special.

I would like to express my gratitude to Prof. Ernesto Benini, who made this amazing experience in Cranfield possible. A special thanks goes to my family that support my studies. I would to thanks my girlfriend Elisa, to have supported and helped me in difficult moments despite the distance and always will. I would like to thanks all my gamer friends that helped me to relax and have some fun. I would to the thanks the Aeroclub of Padova for teaching me how to fly.

Contents

List of Figures	xiii
List of Tables	xix
Abbreviations	xxi
Symbols	xxiii
1 S-duct state-of-the-art	1
1.1 S-duct flow physics	1
1.1.1 Total Pressure Losses	2
1.1.2 Swirl	3
1.1.3 DC60	6
1.2 S-duct Prior Studies	7
1.2.1 Experimental Research	7
1.2.2 CFD	10
1.3 S-duct Future Studies	13
1.3.1 Boundary Layer Ingestion	13
2 Axial Compressor state-of-the-art	15
2.1 Axial Compressor	16
2.1.1 Velocities Triangles	17
2.1.2 Isentropic and Polytopic Efficiency	18
2.1.3 Compressor Map	20
2.2 Transonic Axial Compressor	22
2.2.1 Shock Waves	22
2.2.2 Transonic Compressors Aerodynamics	24
2.2.3 Off-Design Shock Wave Structure	27
2.2.4 Transonic Compressor Losses	28
2.3 Rotor 67	28
3 Optimisation	31
3.1 Problem Formulation	32
3.2 Single and Multi-objectives problems	34

3.2.1	Deterministic Optimisation Problem	34
3.2.2	Concept of Dominance and Pareto Front	35
3.3	Optimization Algorithms	36
3.3.1	Metaheuristic Algorithms	37
3.3.2	Tabu Search	38
4	S-Duct case of study	41
4.1	Geometry	41
4.2	Parameterization	43
4.3	Mesh	46
4.4	CFD Analysis	49
4.5	Optimization Loop	49
4.6	Objective Functions	49
4.6.1	Pressure Losses	51
4.6.2	DC60	51
4.6.3	Symmetry Maximum Error (S.M.E.)	51
5	NASA R67 Computational Analysis	53
5.1	Single Blade Validation	54
5.1.1	Geometry and Mesh Creation	54
5.1.2	Simulation Set-Up	55
5.1.3	Validation's Results	56
5.2	Full Annulus Validation	60
6	Analysis of the Optimisation Results	65
6.1	Baseline	65
6.2	Optimisation with CP and S.M.E. Results	66
6.3	Optimisation with DC60 and S.M.E. Results	71
6.4	Optimisation with CP and Swirl Results	75
7	S-duct and R67 Interaction	79
7.1	S-duct and R67 Simulation Set-Up	79
7.2	Baseline and R67 interaction	81
7.2.1	S-duct Baseline	82
7.2.2	Ogive Interaction with S-duct Baseline	82
7.2.3	R67 Interaction with S-duct Baseline	84
8	S-duct Optimisation and R67 Interaction	89
8.1	CP/S.M.E. optimisation and R67 interaction	89
8.1.1	S-duct Best CP	90
8.1.2	Ogive Interaction with S-duct CP Best	91
8.1.3	R67 Interaction with S-duct CP Best	93
8.1.4	S-duct S.M.E. Best and Trade	97
8.1.5	Ogive Interaction with S-duct S.M.E. Best and Trade	98
8.1.6	R67 Interaction with S-duct S.M.E. Best and Trade	98

8.2	DC60/S.M.E. optimisation and R67 interaction	99
8.2.1	S-duct Best DC	100
8.2.2	Ogive Interaction with S-duct DC Best	101
8.2.3	R67 Interaction with S-duct DC Best	102
8.2.4	S-duct Best S.M.E.	103
8.2.5	Ogive Interaction with S-duct S.M.E. Best	104
8.2.6	R67 Interaction with S-duct SME Best	105
8.2.7	S-duct Trade Off	107
8.2.8	Ogive Interaction with S-duct Trade Off	108
8.2.9	R67 Interaction with S-duct Trade Off	108
8.3	CP/Swirl Optimisation and R67 interaction	110
8.3.1	S-duct Best Swirl	110
8.3.2	Ogive Interaction with S-duct Swirl Best	110
8.3.3	R67 Interaction with S-duct Swirl Best	112
8.3.4	S-duct Trade Off	113
8.3.5	Ogive Interaction with S-duct Trade Off	113
8.3.6	R67 Interaction with S-duct Trade Off	115
9	Conclusions	119

List of Figures

1.1	S-duct in the engine research building	1
1.2	Flow separation in an S-duct	2
1.3	Rappresentation of swirl angle	3
1.4	Swirl Classification	4
1.5	Bulk Swirl Rappresentation	4
1.6	Paired Swirl development in an S-duct	5
1.7	Example of Ground vortex	6
1.8	Tightly-Wound Vortex Generation	6
1.9	Example of DC60	7
1.10	Schematic representation of Wellborn experiment	8
1.11	S-duct pressure contour on planes A, B, C, D and E	9
1.12	Scheme of Delot experiment	10
1.13	View of Marco's run set up	12
1.14	Pressure contours for distorted (left) and clean (right) model near peak condition	12
1.15	Aircraft wake cinetic energy	13
1.16	Expamplable of new project concept using BLI	14
2.1	Turbojet and Turbofan schematic view	16
2.2	Multistage axial compressor	17
2.3	Absolute and relative flow angles in a compressor stage	18
2.4	Absolute and relative states of gas across a compressor rotor and stator	19
2.5	Definition of Polytropic Efficiency	20
2.6	Example of Compressor Map	21
2.7	Example of Compressor Map with inlet distorsion	21
2.8	Oblique shock with the wave angle and flow turning angle	23
2.9	theta beta M relation	24
2.10	Transonic and supersonic flow over a subsonic profile	25
2.11	Shock wave in a supersonic profile	26
2.12	Section profiles of an transonic compressor	27
2.13	Shock wave pattern in a supersonic compressor in different operating condition	27
2.14	Tip leakage vortex	29
2.15	Rotor 67	29

3.1	Rappresentation of the Design Space	33
3.2	Scheme of an Optimization Problem	34
3.3	Example of MOO with constraints	35
3.4	Example of non-dominated objective functions	36
3.5	Posteriori Method and Pareto Front	38
3.6	MOTS memories	39
3.7	Flow diagram of the MOTS algorithm	40
4.1	S-duct Scheme	42
4.2	S-duct parallelepipedic lattice	44
4.3	Difference between baseline and deformed geometry	45
4.4	Overview of Parameterization	47
4.5	Overview of the s-duct mesh	47
4.6	Inlet and Outlet Surface Mesh	48
4.7	Symmetry plane mesh of the S shape	48
4.8	MOTS loop	50
4.9	AIP mesh points	52
5.1	Geometry Frontal View	54
5.2	Mesh of the passage	55
5.3	Compressor ratio with different mesh	57
5.4	Isoentropic Efficiency with different mesh	57
5.5	Pressure and Relative Mach Blade Loading at different span location	58
5.6	Comparison between contours of M_{rel} of experimental and CFD near peak	59
5.7	Contour of M_{rel} near choking condition	60
5.8	Performance of the NASA rotor 67	60
5.9	Full Annulus	61
5.10	Ogive's mesh	61
5.11	Full annulus simulation set-up	62
5.12	Comparison between full annulus simulation, single channel simu- lation and experimental data	63
6.1	Baseline AIP contour	66
6.2	Baseline Total Pressure and Mach Number	66
6.3	CP Best AIP Contour	67
6.4	S.M.E. Best AIP Contour	67
6.5	Trade AIP Contour	68
6.6	Baseline and Results S-bends	68
6.7	Cross-Section CP Best(Left) S.M.E. Best(Mid) Trade Off (Right) .	69
6.8	CP Best Total Pressure and Mach Number	70
6.9	S.M.E. Best Total Pressure and Mach Number	70
6.10	Trade Total Pressure and Mach Number	70
6.11	DC60 Best AIP Contour	71
6.12	S.M.E. Best AIP Contour	71

6.13	Trade AIP Contour	72
6.14	Baseline and Results S-bends	72
6.15	Cross-Section DC Best(Left) S.M.E. Best(Mid) Trade Off (Right)	73
6.16	DC Best Total Pressure and Mach Number	74
6.17	S.M.E. Best Total Pressure and Mach Number	74
6.18	Trade Total Pressure and Mach Number	74
6.19	Swirl Best AIP Contour	75
6.20	Trade Off AIP Contour	75
6.21	Cross-Section SW Best(Left) Trade Off (Right)	76
6.22	Swirl Best Total Pressure and Mach Number	77
6.23	Trade Off Total Pressure and Mach Number	77
7.1	Marco's Configuration	80
7.2	New Configuration	80
7.3	Compressor Map for the Clean Flow and the Baseline	81
7.4	Vorticity of the S-duct Baseline	82
7.5	Velocity Streamline	83
7.6	Velocity Streamline through the Ogive (Left) and at the Outlet (Right)	83
7.7	Inlet Velocity Contour (Left) and Outlet Velocity Contour (Right)	84
7.8	Total Pressure Contour at the Inlet (Left) and Outlet(Right) of the Ogive	84
7.9	Theta Reference and Blade Number	85
7.10	Inlet Mach Number Clean Conditions	85
7.11	Inlet Mach Number Baseline	85
7.12	Streamwise(Top Left),Blade to Blade Abs (Top Right), Spanwise(Bot Left), Crf Abs(Bot Right)	86
7.13	Flow Angle Abs(Top Left),Blade to Blade Rel(Top Right), Flow Angle Rel(Bot Left), Crf Rel(Bot Right)	86
7.14	Velocity Components	87
7.15	Velocity Components in Blade-To-Blade Plane	87
7.16	Blade to Blade Contour	88
8.1	Compressor Map Comparison Between Baseline and Optimisation Results	90
8.2	Vorticity of the S-duct Best CP	90
8.3	Velocity Streamline	91
8.4	Velocity Streamline through the Ogive (Left) and at the Outlet (Right)	92
8.5	Inlet Velocity Contour (Left) and Outlet Velocity Contour (Right)	92
8.6	Total Pressure Contour at the Inlet (Left) and Outlet(Right) of the Ogive	92
8.7	Inlet Mach Number Clean Conditions	93
8.8	Inlet Mach Number CP Best	93

8.9	Streamwise(Top Left),Blade to Blade Abs (Top Right), Spanwise(Bot Left), Crf Abs(Bot Right)	94
8.10	Streamwise(Top Left),Blade to Blade Abs (Top Right), Spanwise(Bot Left), Crf Abs(Bot Right) Clean Flow	95
8.11	Flow Angle Abs(Top Left),Blade to Blade Rel(Top Right), Flow Angle Rel(Bot Left), Crf Rel(Bot Right)	95
8.12	Flow Angle Abs(Top Left),Blade to Blade Rel(Top Right), Flow Angle Rel(Bot Left), Crf Rel(Bot Right) Clean Flow	96
8.13	Blade to Blade Contour CP Best	97
8.14	Vorticity Trade(Left) and S.M.E Best(Right)	97
8.15	Streamline Inlet and Outlet S.M.E Best(Left) and Trade(Right)	98
8.16	Velocity Inlet and Outlet S.M.E Best(Left) and Trade(Right)	98
8.17	Total Pressure Inlet and Outlet S.M.E Best(Left) and Trade(Right)	98
8.18	Mach Abs and Rel S.M.E Best(Left) and Trade(Right)	99
8.19	Blade-to-Blade span=0.2,0.5 and 0.8 S.M.E Best(Left) and Trade(Right)	99
8.20	Compressor Map Comparison Between Baseline and Optimisation Results	100
8.21	Vorticity of the S-duct Best DC	100
8.22	Velocity Streamline	101
8.23	Inlet Velocity Contour (Left) and Outlet Velocity Contour (Right)	101
8.24	Total Pressure Contour at the Inlet (Left) and Outlet(Right) of the Ogive	102
8.25	Inlet Mach Number DC Best	102
8.26	Blade-to-Blade span=0.2,0.5 and 0.8 DC best	103
8.27	Vorticity of the S-duct Best S.M.E.	103
8.28	Velocity Streamline	104
8.29	Inlet Velocity Contour (Left) and Outlet Velocity Contour (Right)	105
8.30	Total Pressure Contour at the Inlet (Left) and Outlet(Right) of the Ogive	105
8.31	Inlet Mach Number SME Best	106
8.32	Streamwise(Top Left),Blade to Blade Abs (Top Right), Spanwise(Bot Left), Crf Abs(Bot Right)	106
8.33	Flow Angle Abs(Top Left),Blade to Blade Rel(Top Right), Flow Angle Rel(Bot Left), Crf Rel(Bot Right)	106
8.34	Blade-to-Blade span=0.2,0.5 and 0.8 S.M.E. best	107
8.35	Vorticity of the S-duct Trade Off	107
8.36	Velocity Streamline	108
8.37	Inlet Velocity Contour (Left) and Outlet Velocity Contour (Right)	108
8.38	Total Pressure Contour at the Inlet (Left) and Outlet(Right) of the Ogive	109
8.39	Inlet Mach Number Trade Off	109
8.40	Blade-to-Blade span=0.2,0.5 and 0.8 Trade Off	109
8.41	Vorticity of the S-duct Best Swirl	110
8.42	Velocity Streamline	111
8.43	Inlet Velocity Contour (Left) and Outlet Velocity Contour (Right)	111

8.44	Total Pressure Contour at the Inlet (Left) and Outlet(Right) of the Ogive	112
8.45	Inlet Mach Number Swirl Best	112
8.46	Streamwise(Top Left),Blade to Blade Abs (Top Right), Spanwise(Bot Left), Crf Abs(Bot Right)	113
8.47	Flow Angle Abs(Top Left),Blade to Blade Rel(Top Right), Flow Angle Rel(Bot Left), Crf Rel(Bot Right)	113
8.48	Blade-to-Blade span=0.2,0.5 and 0.8 Trade Off	114
8.49	Vorticity of the S-duct Trade Off	114
8.50	Velocity Streamline	115
8.51	Inlet Velocity Contour (Left) and Outlet Velocity Contour (Right) .	115
8.52	Total Pressure Contour at the Inlet (Left) and Outlet(Right) of the Ogive	116
8.53	Inlet Mach Number Trade Off	116
8.54	Streamwise(Top Left),Blade to Blade Abs (Top Right), Spanwise(Bot Left), Crf Abs(Bot Right)	116
8.55	Flow Angle Abs(Top Left),Blade to Blade Rel(Top Right), Flow Angle Rel(Bot Left), Crf Rel(Bot Right)	117
8.56	Blade-to-Blade span=0.2,0.5 and 0.8 Trade Off	117

List of Tables

1.1	Davide's Results Swirl.	12
1.2	Davide's Results DC60.	12
2.1	Nasa Rotor 67 Specifications.	30
4.1	S-Duct baseline geometry parameters.	42
4.2	Overall geometry parameters.	43
4.3	Boundary Conditions.	49
5.1	Comparison of different type of mesh implemented	55
5.2	CFX-Pre Set-up parameters	56
5.3	Comparison of different type of mesh implemented	58
5.4	Single channel and full annulus simulation features	62
5.5	Single channel and full annulus simulations' comparison (Near Stall)	62
5.6	Single channel and full annulus simulations' comparison (Near Peak)	62
5.7	Single channel and full annulus simulations' comparison (Near Choke)	63
6.1	Baseline Results.	66
6.2	CP and S.M.E. Results.	67
6.3	DC60 and S.M.E. Results.	71
6.4	CP and Swirl Results.	75
7.1	Clean and Distorted Flow.	82
8.1	Baseline and Optimisation Performance Near Peak.	89
8.2	Baseline and Optimisation Performance Near Peak.	99
8.3	Baseline and Optimisation Performance Near Peak.	110

Abbreviations

AIP	Aerodynamics Interface Plane
CDF	Cumulative Distribution Function
CFD	Computational Fluid Dynamics
MOO	Multi-Objective Optimisation
MOTS	Multi-Objective Tabu Search
NIPC	Non-Intrusive Point-Collocation
NISP	Non-Intrusive Spectral-Projection
ODE	Ordinary Differential Equation
PC	Polynomial Chaos
PDF	Probability Density Function
RANS	Reynolds-Averaged Navier-Stokes equations
SOO	Single-Objective Optimisation

Symbols

I_n	Wiener-Askey polynomial chaos of order n
M_∞	free-stream Mach number
p	pressure
R	universal gas constant
Re	Reynolds number
V_∞	free-stream velocity
X	general second order random process
W	weighting function
γ	specific heat ratio
δ_{ij}	Kronecker delta
Φ	generic polynomial basis
μ	mean
Ψ	Hermite polynomial basis
ρ	density
σ	standard deviation
ξ	Gaussian standard random variable
ζ	generic random variable

*Dedicated to Nonno Bruno, Nonno Narciso, Nonna
Rosa, Nonna Olinda, Papá Giorgio and Mamma
Natalina...*

Chapter 1

S-duct state-of-the-art

1.1 S-duct flow physics



FIGURE 1.1: S-duct in the engine research building.

An serpentine inlet or commonly called S-duct is a type of jet engine intake duct used in several types of military aircraft, like the Lockheed Martin F-22 Raptor, and civil trijet aircraft, like the Dassault Falcon 8X. In the civil field the S-duct represents a design solution approached by some aircraft manufacturers to get less drag and lowering the engine position compared to straight through design. This particular intake also allows a shorter fin and a rudder closer to longitudinal axis. On the other hand, due to his bendend shape, engine performances are compromised and inlet distortions are genereted. The latter can be categorised

as: Total Pressure, Swirl Angle and Total Temperature. The Total Temperature distortion is not analysed in this thesis since it is relevant only for military aircraft.

1.1.1 Total Pressure Losses

The definition of the total pressure is: the pressure value when the fluid element is brought to rest isentropically [2]. The total pressure for an incompressible flow can be defined as:

$$P_{tot} = P_{static} + \frac{1}{2}\rho v^2 \quad (1.1)$$

and the total pressure losses are described with the Pressure Recovery (PR) parameter:

$$PR = \frac{P_{tot,out}}{P_{tot,in}} \quad (1.2)$$

The total pressure losses are caused by the cross-section growth and by the duct bends. These two zones lead to flow separation and cause a reverse flow and vortices formation. The flow separation has been studied for many years and it is a common aerodynamics phenomenon that occurs in diffusing channel. The phenomenon is due to the boundary layer detachment off the walls, because the flow experiences an adverse pressure gradient in increasing cross-section area. As a result, the vortices generated convey the low-energy region towards the center, reducing both magnitude and uniformity pressure distribution leading to pressure losses. The flow detachment, in diffusing S-duct, is placed right after the first bend and it occupies a wide downstream region generating a big wake, as proved by Wellborn's experiments [3]. We have to clarify that this downstream region is generated, not only by the growing area, but also by the curved centerline.

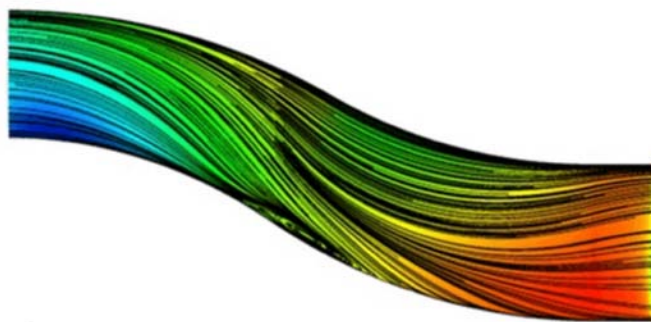


FIGURE 1.2: Flow separation in an S-duct.

1.1.2 Swirl

Swirl is a parameter that determines the distortion of the flow. In fact, considering cylindrical coordinates it is possible to divide the velocity vector in the tangential and the axial components and the swirl is defined as follow:

$$\alpha = \arctan \frac{V_{\theta,AIP}}{V_{z,AIP}} \quad (1.3)$$

If it has the same rotation direction of the compressor it is considered positive.

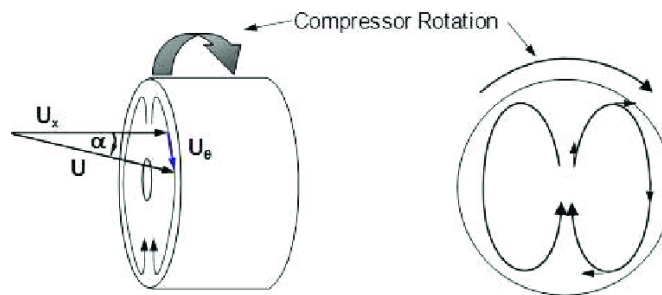


FIGURE 1.3: Representation of swirl angle.

As Fig.1.3 shows, the swirl physically represents the angular deviation between the local velocity vector and the normal vector, both referred to the AIP plane. El-Sayed in [4] affirm how the swirl phenomenon might cause severe problems in the aircraft engine, such as vibration and surge. In aeronautics, there are four different types of swirl that could affect a flow within an S-pipe and these are briefly described below:

- Bulk Swirl
- Paired Swirl
- Tightly-Wound Vortex
- Cross-Flow Swirl

Bulk Swirl:The bulk swirl develops when the entire flowfield spins in one direction about the compressor axis; the swirl is called co-rotating swirl if flow rotates in the same direction of the engine, otherwise it is named counter-rotating swirl. This distortion is defined as “the circumferential mean value of the flow angle for each constant radius” [5]. The generation of the Bulk swirl can be internal or external to the duct, but the former circumstance is more important for the project;

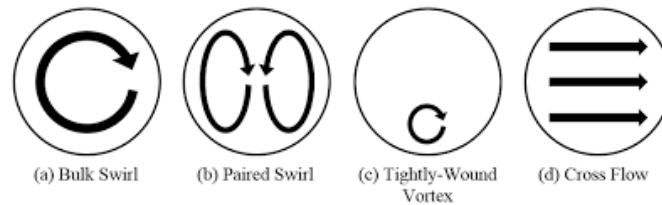


FIGURE 1.4: Swirl Classification.

it occurs when the “inlet flow experienced a non-axisymmetric total-pressure gradient, normal to angle plane, which combines with static-pressure gradient of the S-bend flow” [6]. Figure 1.5 displays how the sideslip flow separation at the inlet causes a wide lowenergy region that starts to rotate. His intensity mainly depends on geometric parameters and flow conditions.

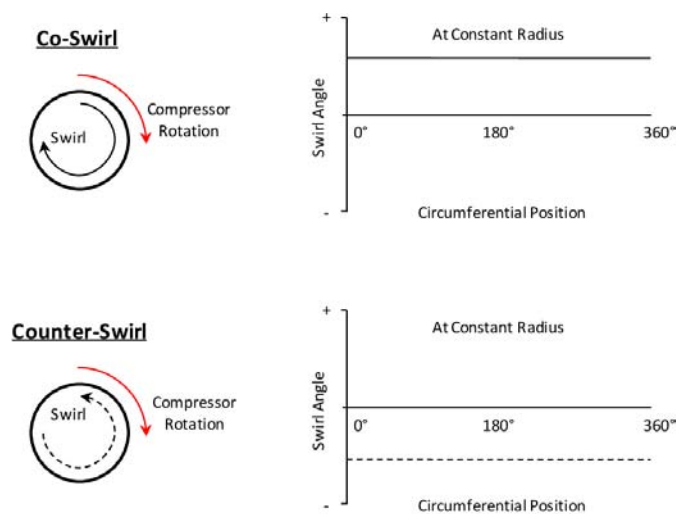
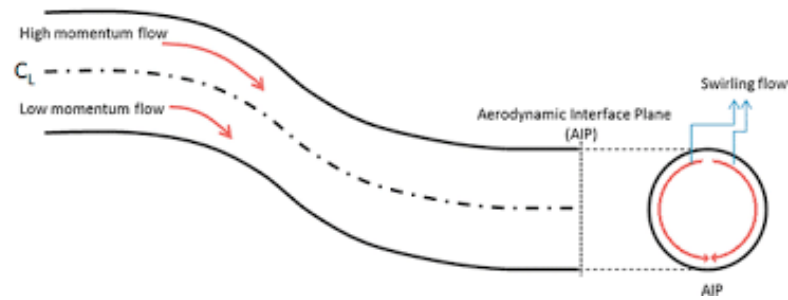


FIGURE 1.5: Bulk Swirl Representation.

Paired Swirl: This type of swirl is the most important because it is the most common swirl that takes place in a bent duct. The paired swirl consists of two or more paired vortices rotating in opposite directions. If the vortices have the same magnitude, the swirl is called twin swirl, otherwise simply offset paired swirl. To explain the physics behind this type of swirl there are two alternatives. The first is due to the vorticity vector that is turned by the duct shape, which creates a flow rotation at the end. The second explanation is due to the pressure gradient and the momentum. Referring to figure 1.6(a) we can see that in the low area there is an increasing static pressure due to the growing of the radius and the balancing of the centrifugal forces.



(a) High momentum and Low momentum flow in an S-duct.



(b) Paired Swirl in an S-duct.

FIGURE 1.6: Paired Swirl development in an S-duct.

Now we have to consider the boundary layer conditions that influence the velocity of the flow. This velocity is equal to zero at the walls, and it is maximum in the flow core, so even the momentum distribution is either not uniform. There is a blending of a high velocity and low velocity and this is the reason of the two counter-rotating vortices. When the high velocity flow, that is in the core of the duct, is going through the bend it tries to maintain his path, thanks to the higher momentum, until it finds the upper wall. On the other hand, the low velocity, that is located near the walls, whenever it finds the adverse pressure gradient region, slips around the walls towards the inside part of the bend.

Tightly-Wound Vortex: It is commonly known as inlet-ground vortex for its characteristic of attaching to airplane surfaces or to the ground. This type of swirl is highly energetic and it is generated by several mechanisms such as tip vortices, leading-edge extensions and near-static operations in ground proximity.

Cross-flow swirl: This kind of swirl is similar to the paired one, except for the presence of a uniform velocity in cross-flow direction. It is common to find this type of swirl in straight inlet ducts with the flow directions normal to the motion



FIGURE 1.7: Example of Ground vortex.

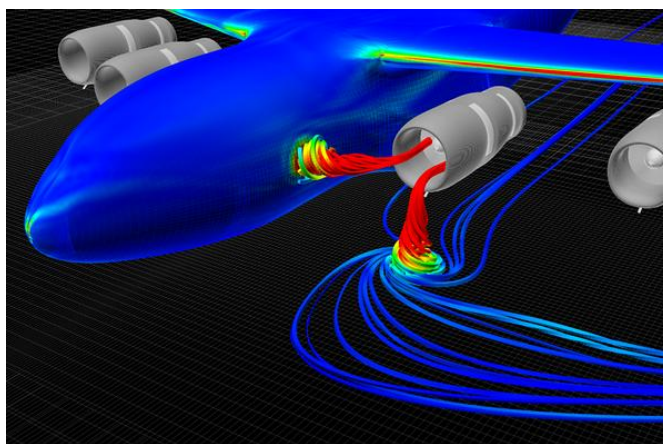


FIGURE 1.8: Tightly-Wound Vortex Generation.

of the aircraft. Lift fans, turboshaft and turboprop with bifurcated intake ducts usually suffer this type of swirl.

1.1.3 DC60

The $DC\theta$ is a distortion parameter that represents the variation of the total pressure across the engine face. It has been derived by Rolls Royce and used extensively in the European fighter programs Tornado (Stocks and Bissinger, 1981) and Eurofighter (Bissinger and Jost, 2000) as reported by [7]. It's important to define this parameter because in this way we can quantify the total pressure distortion at the AIP. It is defined as follows:

$$DC\theta = \frac{P_{tot,AIP} - P_{tot,\theta}}{q_{f,AIP}} \quad (1.4)$$

Where $P_{tot,\theta}$ is the minimum mean total pressure of all sectors of the extent in the AIP (so it correspond to the worst sector), $P_{tot,AIP}$ and $q_{f,AIP}$ are the mean total pressure and the dynamic head, respectively, at AIP. θ is the angular value of the sector and 60° is the value that is most used.



FIGURE 1.9: Example of DC60.

1.2 S-duct Prior Studies

Nowadays s-duct intake represents an important topic both for military and civil applications; several research in the last decades has been performed to better understand and map flowfield characterization in order to reduce flow distortions and improve duct performances. In the early studies, information about the flowfield has been obtained only by prototype test. Then with the progresses in computational analysis we are now able to simulate the flow with mathematical models, facilitating S-duct studies. Thanks to the CFD we can easily compare experimental results with the mathematical models.

1.2.1 Experimental Research

In order to determine the behaviour of the flow field throughout and at exit of s-ducts, several experimental campaigns have been conducted over the years. The whole history of experimental test is well described in [8] and in this paragraph we will consider only the major events.

- John R Weske: One of the very first experimental research was conducted by Weske. He studied the pressure and velocity field at the exit of elbow shaped

ducts with the final aim of improving the knowledge on aircraft intakes design parameters. The main finding was that the most influential parameter for the pressure drop downstream of the ducts was, more than the offset, the ratio between the exit and the inlet duct radius.

- John R Henry: He studied the effects of flow separation and skin friction on the pressure recovery in 1944, elaborating results from previous experimental investigations.
- P Bansod and RW Guo: The presence of the two contra-rotating vortices at the exit of s-shaped intakes was investigated in detail only later, with the works of Bansod and Guo on simplified models of engine inlets.

All of the above reported experimental investigations have the goal to build a more concrete knowledge of the complex aerodynamic phenomena of s-shaped ducts. Most of this studies were conducted with simplified models, thick boundary layer and incompressible flow. Moreover, the duct's radius was constant, so it did not involve the diffusion phenomena throughout the duct, hence reducing the presence of separation. A consistent breakthrough in the physical knowledge of the s-duct aerodynamics was achieved thanks to the experimental and computational campaigns performed by Wellborn [9] in the 1993. In these studies, both the effects of compressibility and diffusion were taken into account. All of the tests were performed at NASA Lewis Research Center. The experiment is well-described in

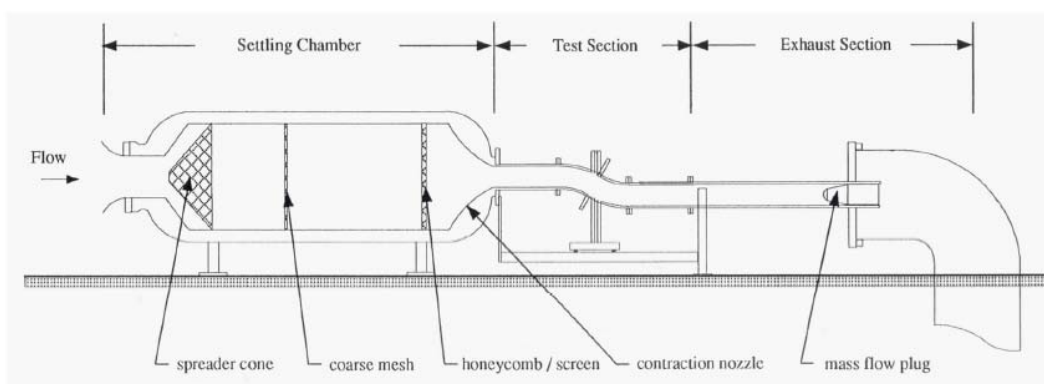


FIGURE 1.10: Schematic representation of Wellborn experiment.

[8]. After passing through a bell mouth intake the flow moved to a settling chamber to be then expanded and accelerated in a convergent nozzle. The contraction ratio of the latter was chosen in order to achieve low turbulence intensity and uniform

flow. A constant area section then guided the flow directly into the duct. A double circular arc diffusing duct was designed (Fig.1.10), with the aim to develop and study a complex three dimensional velocity field and flow separation. Visualization techniques and pressure measurements were used to investigate the flow. 220 pressure transducers at different stream-wise and circumferential positions were used to register the wall static pressure throughout the duct. Three- and five-hole probes were used to measure total pressure, static pressure and flow direction at different planes (planes A, B, C, D and E in Fig.1.11) for numerous radial and circumferential positions. The inlet Mach number was set to 0.6 and the Reynolds number of the inlet free-stream at $2.6 \cdot 10^6$. The study demonstrated the strong coupling between the boundary layer and the flow at the core of the duct. A vast separated region downstream of the first bend was observed. Furthermore, the curvature of the duct was found to be responsible for the generation of pressure-driven secondary flow, which eventually induce the creation of the two contra-rotating vortices downstream.

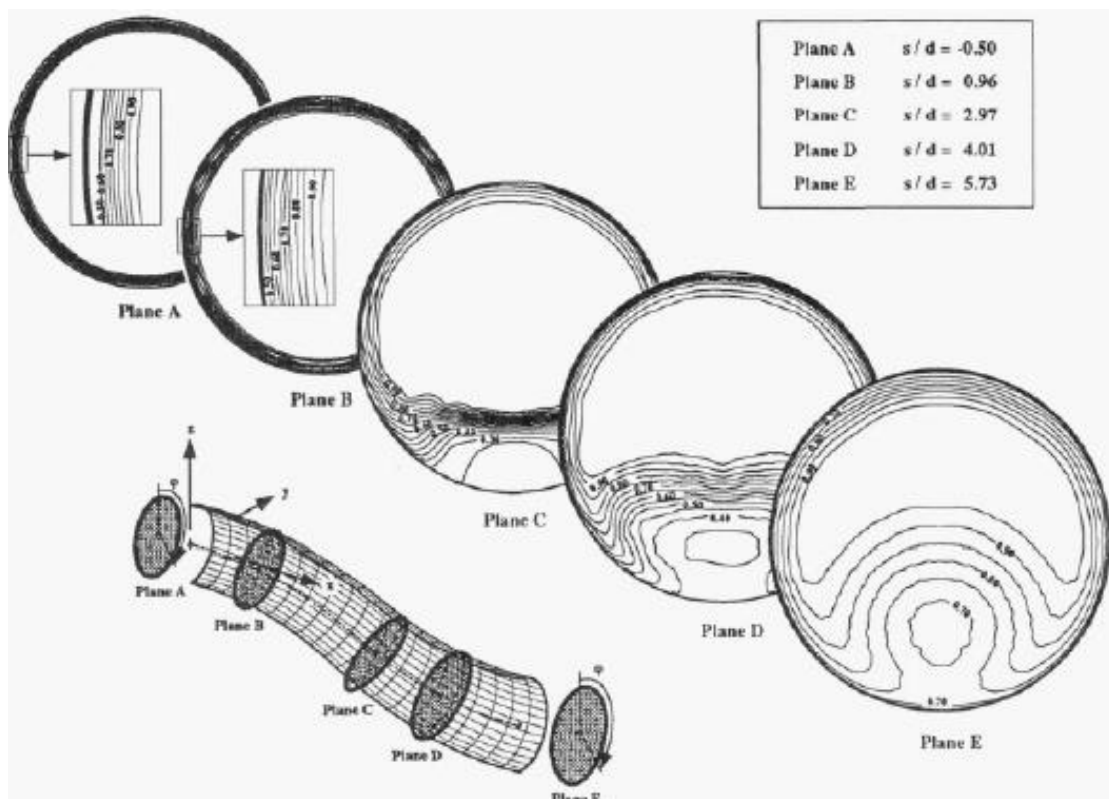


FIGURE 1.11: S-duct pressure contour on planes A, B, C, D and E.

1.2.2 CFD

Computational fluid dynamics (CFD) is the rapidly evolving science of numerically solving the equations of fluid motion to produce quantitative predictions and/or analyses of fluid flow phenomena. When used appropriately, CFD is often ideal for parametric studies or flow-physics investigations that would otherwise be impractical or impossible via entirely theoretical or experimental efforts.

Delot CFD analysis

The Delot analysis, conducted in 2006 are the starting point to understand how to simulate a flow in a s-duct. Delot based her study on Wellborn's S-duct geometry carrying out several computational tests for defining the best set up that best reproduce real flow. She compared several meshes, solver codes and turbulence models; the project stated that Fluent solver best matches the separate region and well predicts low pressure region. For the purpose of our analysis, it is crucial to remind an important statement that she postulated after her research: the fluent solver well represents the separated region and the low pressure region, but the PR coefficient is higher than the one of the real flow.

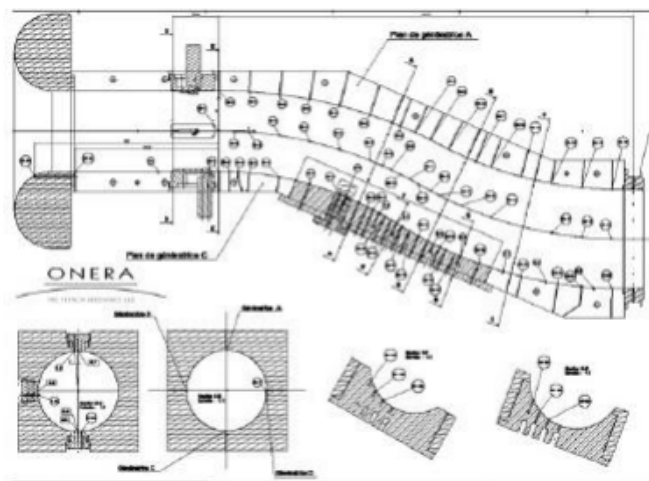


FIGURE 1.12: Scheme of Delot experiment.

Recent CFD analysis

In order to understand the simulation done, in this thesis we have to analyze the previous work done by Marco Barison [10], Enrico Manca [11], L. Guglielmi [6], Rigobello Aurora [12], R. Tridello [13], Alessio D' Ambros [14], Davide Dal Magro

[1] and Marco Tridente [15]. Marco Tridente, Alessio D'Ambros and Davide Dal Magro are by far the most important and the most recent sources.

- Alessio D'Ambros:

His research consisted in the optimization of the Wellborn's geometry considering two objective functions: the pressure losses ($1 - PR$) and the swirl. It is important to remind how this author proceeded: the geometry management has been controlled with the Free-Form Deformation (FFD) technique, whereas the analysis of the flow has been performed using the steady-state computational fluid dynamics (CFD). Furthermore, the exploration of the design space has been achieved utilising the heuristic optimization algorithm Tabu Search (MOTS). As a matter of fact, the two most important results of this work are, on one hand the huge reduction of the value of swirl and, on the other hand the parametrization that D'Ambros implemented. In fact, with respect to the previous studies, he had the intuition of changing the position of the controls points and this variation was the cause of the good results obtained.

- Davide Dal Magro

His research improved Alessio D'Ambros work finding a new objective function: the DC60 that reduce the pressure distorsion at the AIP using the same heuristic optimization algorithm Tabu Search (MOTS). He then perform studies on input uncertainties changing from a non robust to a robust optimization and using as input the velocity, with a gaussian distribution and a standard deviation of 10. To quantify the uncertainties he used two non intrusive polynomial chaos techniques: the non intrusive point collocation and the non intrusive spectral projection. In the end, Davide cooperated with Marco Tridente to join the s-duct with the rotor 67. In order to do that he scaled up the Delot s-duct and then perform two non robust optimization, the first one with the CP and the swirl as objective functions, the second one with the CP and the DC60 as objective functions.

- Marco Tridente

His research consisted in the study of rotor 67 performance. He created various mesh and then perform steady state simulation to validate the model. After that he studied the influence of the s-duct flow on the full annulus using Davide's s-ducts. To study the whole system he had to create also the ogiva

TABLE 1.1: Davide's Results Swirl.

	CP	Improvement	SWIRL	Improvement
Baseline	0,048042	-	4,73307	-
CP best	0,043898	8,626%	3,233	31,68159%
Swirl best	0,048298	-0,533%	2,511	46,9437%

TABLE 1.2: Davide's Results DC60.

	CP	Improvement	DC60	Improvement
Baseline	0,048042	-	0,48911	-
CP best	0,0438	8,82769%	0,0761	84,4392%
D60 best	0,044232	7,93056%	0,00017	99,9656%

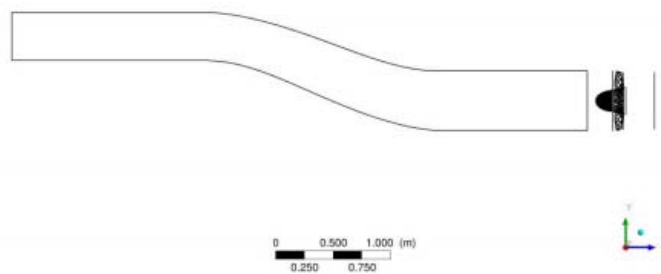


FIGURE 1.13: View of Marco's run set up.

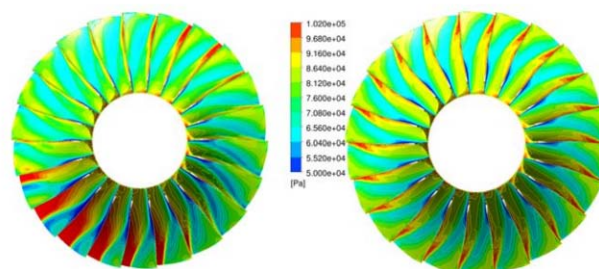


FIGURE 1.14: Pressure contours for distorted (left) and clean (right) model near peak condition.

mesh. In total he studied 7 geometries and he decided to simulate just one speed line, and not the entire compressor map; because the simulation was highly time-demanding. The speed line that was taken into account was the 95% of the rotational speed. The results from the simulation underlined how the inlet condition on the fan are distorted and this lead to deterioration of the rotor overall performance. In the end he observed that the distortion is located on the left lower part of the rotor as you can see in Fig. 1.14

1.3 S-duct Future Studies

To advance in the propulsion performance and to reduce emissions new technologies have to be studied. To do this Other than the transonic fan, that has high performance, the Boundary Layer In-gesting studies has recently attract the attention of many aeronautics companies.

1.3.1 Boundary Layer Ingestion

The Boundary Layer Ingestion is so important because it can reduce fuel burn in jet engines, thus reducing emissions and the cost of operating the aircraft. With BLI, an airplane's engine is located near the rear of the aircraft. Thanks to the presence of the fuselage and the wings the inflow of the engine is distorted and this lead to re-energize the aircraft wake. This gives us the opportunity to waste less kinetic energy.

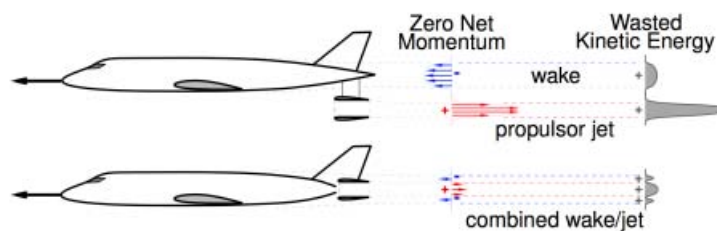


FIGURE 1.15: Aircraft wake kinetic energy.



FIGURE 1.16: Exampble of new project concept using BLI.

Chapter 2

Axial Compressor state-of-the-art

Most modern passenger and military aircraft are powered by gas turbine engines, which are also called jet engines. There are several different types of jet engines, but all jet engines have some parts in common. Typically every jet engine is composed by:

- Intake or duct: that capture and drive the air to the compressor;
- Axial Compressor: that compress the flow;
- Combustion Chamber: that mix the air and the fuel and burned;
- Axial Turbine: that converts the flow of the fluid into rotating mechanical energy;
- Nozzle: that increase the kinetic energy of the flow at the expense of its pressure and internal energy.

The most common propulsive system used in the civil aviation is the turbofan, which is characterized by a big fan in front of the compressor. This required that part of the energy of the turbine is used to move a fan instead of producing thrust in the nozzle. Having a big fan leads to increase the mass flow rate breathed reducing the specific thrust but increasing the propulsive efficiency.

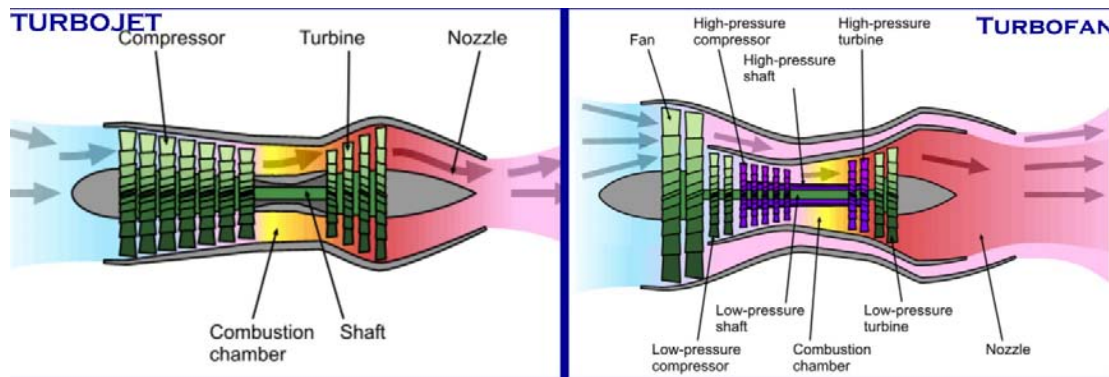


FIGURE 2.1: Turbojet and Turbofan schematic view.

2.1 Axial Compressor

Compressors and fans provide mechanical compression for the air stream that enters a gas turbine engine. Thermodynamically, their function is to increase the fluid pressure, efficiently. The shaft power to drive the compressor typically is produced by expanding gases in the turbine. There are three types of compressors:

- radial-flow
- mixed-flow
- axial-flow

In the first one the fluid path undergoes a 90° turn from the axial direction. These machines are sometimes referred to as centrifugal machines. The second one is an hybrid between the axial and the radial-flow machines. In the third one, the fluid path is predominantly along the axis rotation of the shaft. In aircraft gas turbine engines, the axial-flow compressors and turbines enjoy the widest application and development due to its ability on working with large mass flow and the high efficiency. To achieve a large pressure rise, axial-flow compressors and fans need to be staged thus becoming a multistage machinery, or compression system. The single stage is composed by a rotor and a stator where the rotor blade imparts angular momentum to the fluid, while the following stator blade row removes the angular momentum from the fluid. Sometimes more stator blades are used, in particular:

- The IGV (inlet guide vanes) that are placed in front of the compressor. They are designed to add swirl in the direction of rotor motion to lower the Mach number of the flow relative to the rotor blades, and thus improve the aerodynamic performance of the rotor.

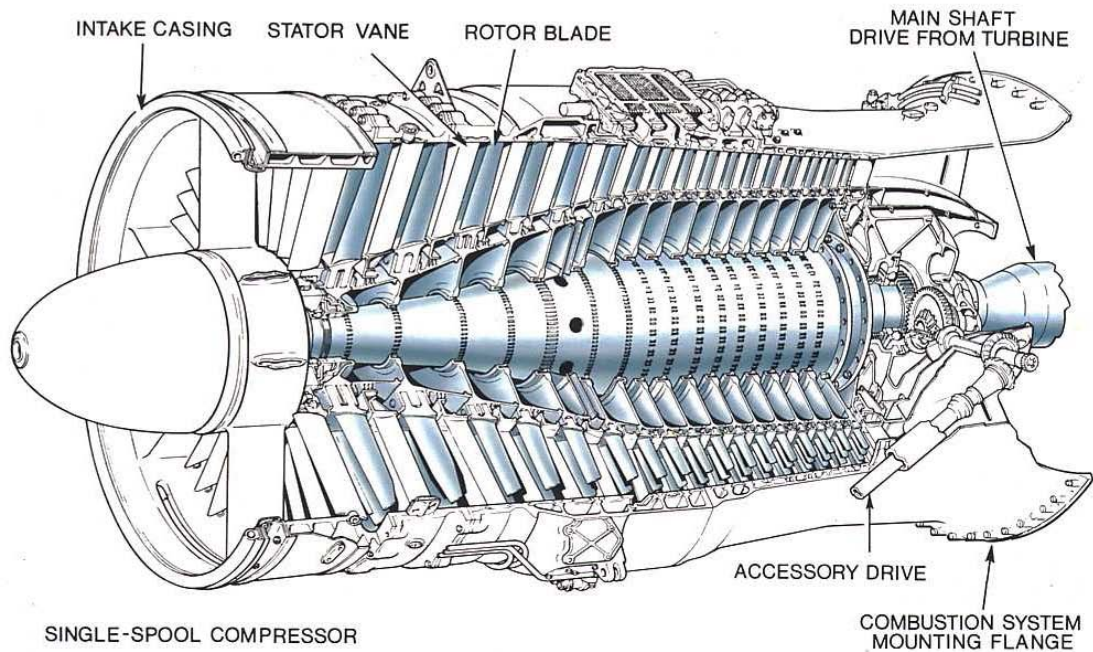


FIGURE 2.2: Multistage axial compressor.

-The OGV (outlet guided vanes) that are placed downstream of the last stage. They are designed to reduce the swirl of the fluid before it enters in the channel for the combustion chamber.

2.1.1 Velocities Triangles

In order to better understand how the energy is exchanged within a stage, it is important to analyse the triangles of velocity. Referring to Figure 2.3, we can define section 1 as the inlet, section 2 as the outlet of the rotor and section 3 the outlet of the stator. In all sections there is a triangle of velocity where:

- c is the absolute flow velocity
- ω is the relative flow velocity
- U is the tangential blade speed ($U = \omega \wedge r$)

and the relation that exists is:

$$\vec{c} = \vec{\omega} + \vec{U} \quad (2.1)$$

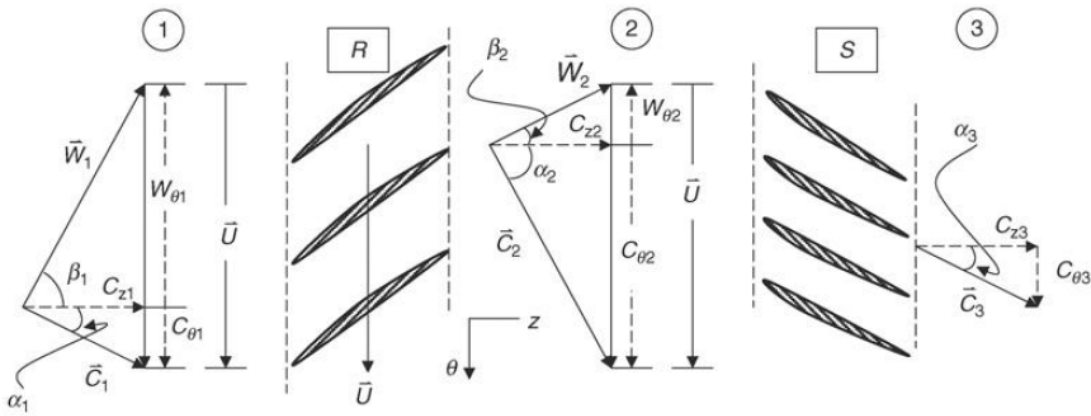


FIGURE 2.3: Absolute and relative flow angles in a compressor stage.

The flow angles are measured with respect to the axial direction, or axis of the machine, and are labeled as α and β , which correspond to the absolute and relative flow velocity vectors c and ω , respectively. One method of accounting for positive and negative swirl velocities is through a convention for positive and negative flow angles. It can be observed that the absolute velocity vector upstream of the rotor has a swirl component in the direction of the rotor rotation. Hence, the absolute flow angle α_1 is considered positive.

The triangle of velocity can be plotted in the T-S diagram shown in Figure 2.4 using also the assumption that the axial velocity maintains a constant value throughout the stages. Through the rotor the mechanical energy of the shaft is transformed into fluid enthalpy increasing the absolute velocity, static and total temperature. But to satisfy equation 2.1, the relative velocity must decrease and as a consequence the static pressure increases. After the rotor the flow passes through the stator and, since the entire work of the stage is done by the rotor, the total temperature is conserved. Hence the blades of the stator act as a diffuser for the absolute velocity. Consequently, there is only a loss of total pressure due to the friction of the fluid with the blade.

2.1.2 Isentropic and Polytropic Efficiency

To better understand the performance of a compressor it is really useful to introduce the isentropic efficiency. This is calculated as:

$$\eta_{is} = \frac{L_{is}}{L} = \frac{h_{2is}^0 - h_1^0}{h_2^0 - h_1^0} \quad (2.2)$$

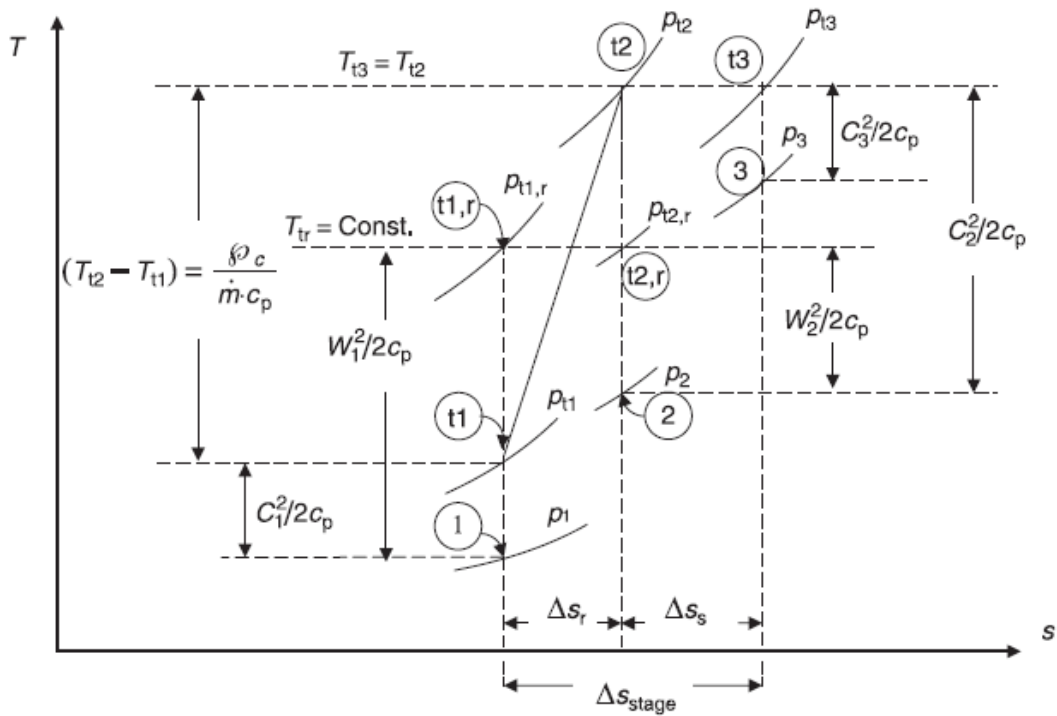


FIGURE 2.4: Absolute and relative states of gas across a compressor rotor and stator.

and it is called total-to-total efficiency. The isentropic efficiency considers only the start and end states of the compression and expansion processes and it pays no attention to the actual paths the compression and expansion processes take. In fact, the higher the exit temperature is, the higher the real work is and, since it is at the denominator of equation 2.2, the lower the efficiency is. Since the work is not a thermodynamic property and depends on the actual path, the polytropic analysis endeavours to account for the path taken during the compression and expansion processes in determining the actual work. In a polytropic process, the compression or expansion process takes place in small steps (infinitesimally small steps). Calculating the work for the polytropic process involves the summation of the work for each step. It is calculated as follow:

$$\eta_{pol} = \frac{dh_{is}}{dh} = \frac{dp/\rho}{cp dT} \quad (2.3)$$

That can be transform into:

$$\eta_{pol} = \frac{k}{k-1} \frac{\ln\left(\frac{p_2^0}{p_1^0}\right)}{\ln\left(\frac{T_2^0}{T_1^0}\right)} \quad (2.4)$$

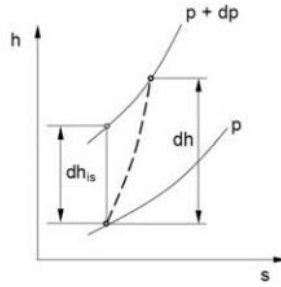


FIGURE 2.5: Definition of Polytropic Efficiency.

2.1.3 Compressor Map

Compressor pressure ratio plotted against the mass flow rate through the compressor is the compressor performance map. A compressor operates over a large range of flow and speed delivering a stable head/pressure ratio. As state in [16] and referring to figure 2.6, the surge point in a compressor occurs when the compressor back pressure is high and the compressor can not pump against this high head causing the flow to separate and reverse its direction. Surge is a reversal of flow and is a complete breakdown of the continuous steady flow through the whole compressor. The phenomenon of surging should not be confused with the stalling of a compressor stage. Stalling is the breakaway of the flow from the suction side of the blade aerofoil thus causing an aerodynamic stall. A multi-stage compressor may operate stably in the unsurged region with one or more of the stages stalled, and the rest of the stages unstalled. A decrease in the mass flow rate, an increase in the rotational speed of the impeller, or both can cause the compressor to surge. The curves that present a vertical asymptote are iso-velocity line. This asymptote is the choke limit. The compressor choke point is when the flow in the compressor reaches Mach 1 at the blade throat, a point where no more flow can pass through the compressor. This phenomenon is often known in the industry as “Stone Walling”. In the end, there are the isoefficiency lines that

represent the efficiency of the compressor. Although uniform inlet conditions are

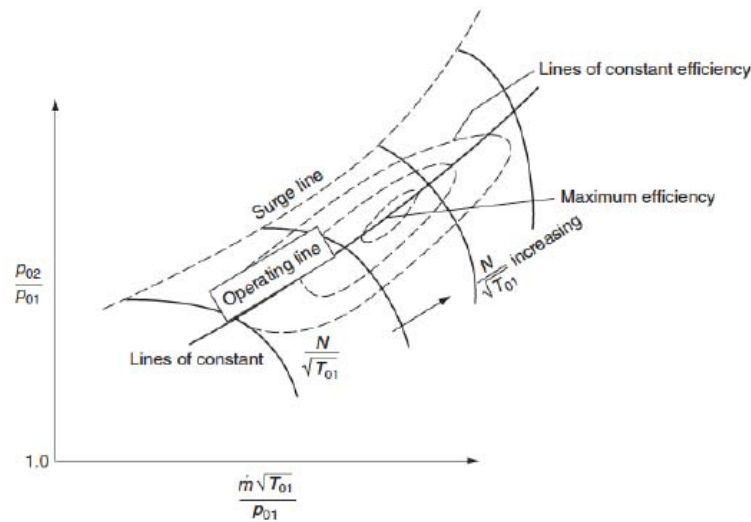


FIGURE 2.6: Example of Compressor Map.

highly desirable and system designers attempt to insure distortion-free flow entering compressors, situations frequently arise in which substantial total pressure, velocity, and angle variations exist at the compressor inlet. Aircraft gas turbines are particularly prone to inlet distortion problems due to changes in aircraft attitude and the effect of the airframe on the inlet flow conditions, but industrial installations may also suffer from inlet distortion in cases where poorly designed bends have been installed upstream of the compressor. Many research reveal that the inlet distortion both deteriorates the performance of the fan resulting in reduction of total pressure ratio, efficiency and stall margin of the transonic compressor.

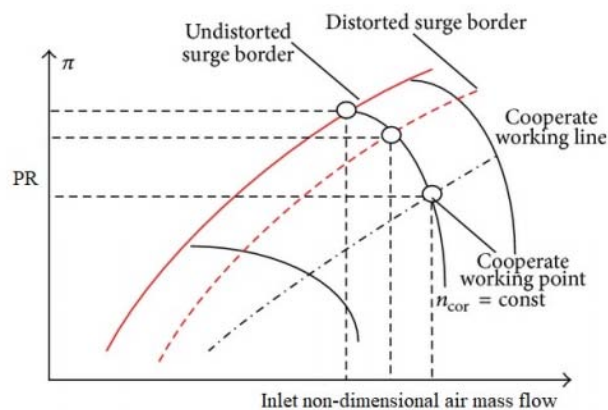


FIGURE 2.7: Example of Compressor Map with inlet distortion.

2.2 Transonic Axial Compressor

In modern gas turbine engines requirements for high performance and compactness have become very tight leading the technological development towards the reduction of cost and increased safety. Because of this it is mandatory for compressor stages to operate at the highest values of both efficiency and pressure ratio as possible. As a matter of fact high efficiency implies a low fuel consumption, while a high pressure ratio helps to decrease the number of stages and the cross-sectional area of the engine: as a consequence size and weight can be reduced. Transonic axial flow compressors are fundamental to achieve the task as they make it possible to maximize pressure ratios per stage unit. A modern transonic fan stage produces a stage pressure ratio of 1.6. This type of compressors have tip blade speed up to 500 m/s. This gives an higher specific work and the increased rotational speed has brought relative mach number levels in the transonic regime, with peaks of up to about 1.7. The resulting flow field is really complex: while the inner sections of rotor blade operate at relatively high subsonic Mach numbers, proceeding towards the tip, relative speeds increase up to supersonic values featuring highly three-dimensional inviscid/viscous structures, strong shock boundary layer interaction and intense tip clearance effects [17]. In this way a single compressor rotor can achieve pressure ratios even higher than two. However the isentropic efficiency results slightly penalized by the presence of the shock wave that dominates the passage in the outer part of the blade. Despite the slightly lower efficiency, transonic compressors remain the most efficient solution, especially for aircraft engines, thanks to their compactness. Therefore, considerable research efforts are being spent, both numerically and experimentally, to improve efficiency and stall margin at peak efficiency and near stall operation. In next section it will be briefly described the shock wave theory to better understand the interaction between the shocks and the blade.

2.2.1 Shock Waves

The shock wave, or shock, is a type of propagating disturbance that moves faster than the local speed of sound in the medium. The shock wave propagates through a medium but is characterized by an abrupt, nearly discontinuous, change in pressure, temperature, and density of the medium and since it is a no-work process the

total temperature and enthalpy remains constants (in normal shock). The shock wave can be divided into:

- Normal shock wave
- Oblique shock wave
- Bow shock

Normal shock wave can be seen as a special case of an oblique shock wave. This wave is normal to the flow and causes a sudden deceleration; static pressure, temperature, density, and entropy rise; Mach number and total pressure drop across the wave. Compression Mach waves may coalesce to form an oblique shockwave. Figure 2.8 shows a schematic drawing of an oblique shock flow with a representative streamline that abruptly changes direction across the shock. The shock wave angle with respect to upstream flow is called β and the flow-turning angle is θ . The flow is resolved into a normal and a tangential direction to the shock wave. From the equation of continuity along the tagential direction, it is possible to ob-

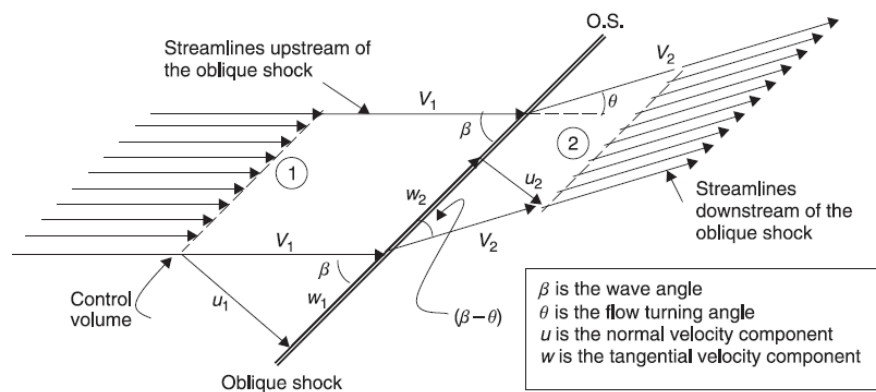


FIGURE 2.8: Oblique shock with the wave angle and flow turning angle.

tain that $\omega_1 = \omega_2$, so the tangential component of the velocity remains constant and the Mach number downstream of the shock wave depends only by the normal component of the upstream Mach and the two angle β and θ as proven by equation 2.5.

$$M_2^2 = \frac{M_{n,2}}{\sin(\beta - \theta)} \quad (2.5)$$

From the continuity equation and with the constancy of the tangential components, the $\theta - \beta - M$ relation can be obtain.

$$\tan \theta = 2 \cot \beta \frac{M_1^2 \sin \beta - 1}{M_1^2(\gamma + \cos(2\beta)) + 2} \quad (2.6)$$

and in relates the deflection angle as a function only of the inlet mach and β . The function can also be plotted giving the $\theta - \beta - M$ graph reported in figure 2.9. Once set the θ and the Mach there are two β angle possible solution. This is

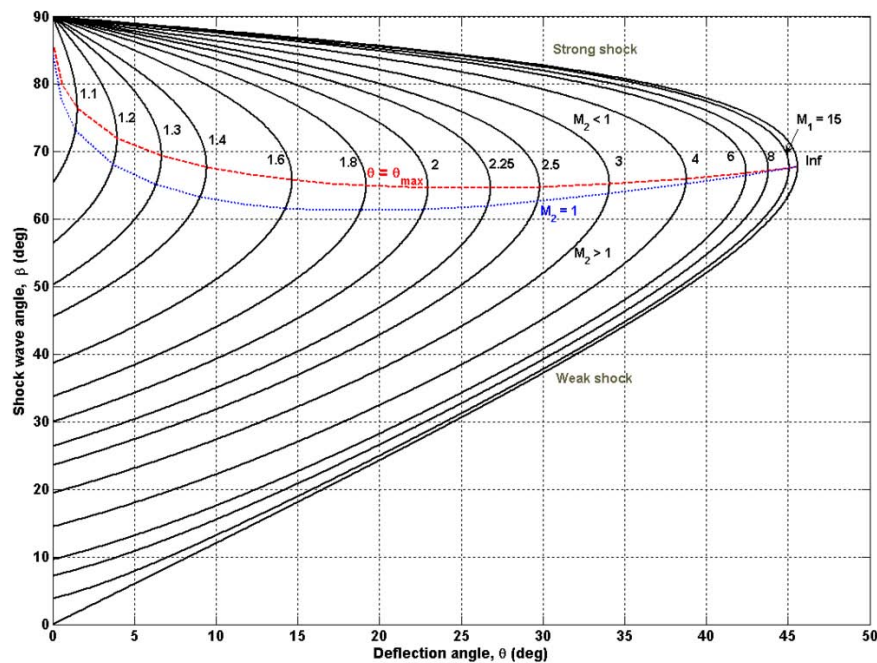


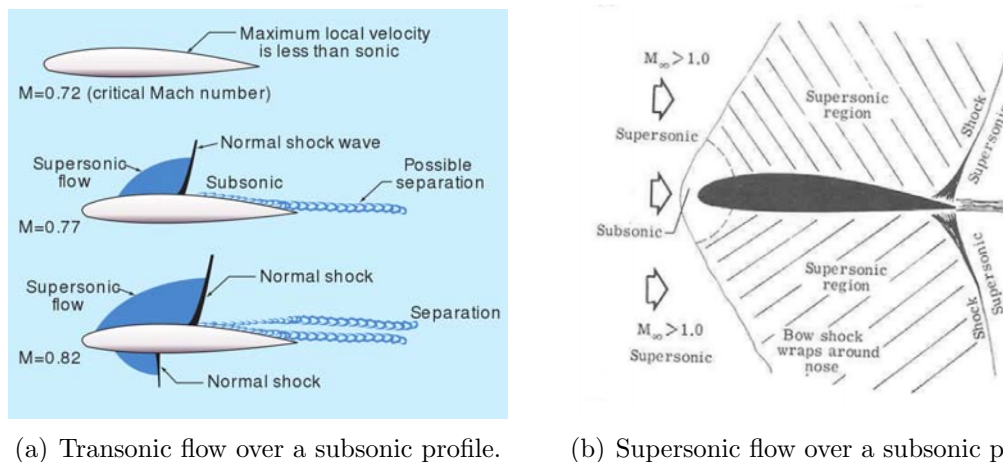
FIGURE 2.9: θ - β - M relation.

related with the concept of strong and weak shock, above the red line the shock is strong and under the red line is weak. This line connects all the maximum deflection angle of each iso-Mach line; in fact for every Mach number there is a maximum value of θ . If $\theta > \theta_{max}$ a bow shock generates detached, from a certain distance δ , from the body. The blue line is called sonic line because it divides the graph into two zone ($M < 1$ and $M > 1$).

2.2.2 Transonic Compressors Aerodynamics

The Aerodynamic of the transonic compressor is profoundly different from the subsonic one and in the last decades many research have been conducted. As

already pointed out to reach higher pressure ratio high tip speed becomes mandatory leading to supersonic relative Mach number near the tip. Because of this, the outer part of the annulus experiences strong shock waves that a subsonic profiles can't handle well. In fact, if a subsonic profile is invested by a flow with Mach over 0.7-0.75 it is going to accelerate due to his rounded leading edge creating a sonic bubble leading to a normal shock. However the absolute Mach number is restricted under the unity, more precisely 0.7 is usually cited as the Mach number limit in front of the fan to avoid choking in the intake. If the relative Mach continue to grow reaching supersonic value there is the creation of the bow shock detached from the profile. Figure 2.10(a) highlights that there are two different zone: one subsonic in which the shock is almost normal, hence the reduction of the Mach is consistent, while the supersonic one is far from the leading edge because the shock is too weak. A supersonic blade profoundly differs from a subsonic one. The



(a) Transonic flow over a subsonic profile.

(b) Supersonic flow over a subsonic profile.

FIGURE 2.10: Transonic and supersonic flow over a subsonic profile.

leading edge of the profile has to be as sharp as possible to have an oblique shock attached to the blade as much as possible, because a normal and detached shock would bring higher losses. The radius will be limited by mechanical integrity considerations only. Even the thickness of the blade is limited to a minimum dictated by mechanical constraint, in order to interfere the least possible with the supersonic flow. Then the supersonic profiles are highly staggered to allow the relative flow to enter smoothly into the blade passage, reaching 60 with respect to the axial direction. A distinguishing detail of a supersonic profile is the camber line that is straight up to 60 – 70% of the chord, while the remaining part is slightly curved. To better understand this choice it is important to analyse the path that the fluid undergoes. A fluid particle before entering the cascade crosses a series of oblique

shocks, detaching and compressing the flow. However the prediffusion performed by these fronts is gentle, because, thanks to the viscosity of the fluid, shocks fade as they propagate upstream the compressor [17]. The biggest contribution to the pressure rise is given by the much more intense shock passage between the two blades. As can be notice in figure 2.11 this shock is almost normal to the incoming flow, hence the shock is "stronger" than the oblique one. The normal shock leads to a dissipative diffusion process that decelerate the relative flow downstream to subsonic velocities. After the analysis it is possible to unveil why the transonic

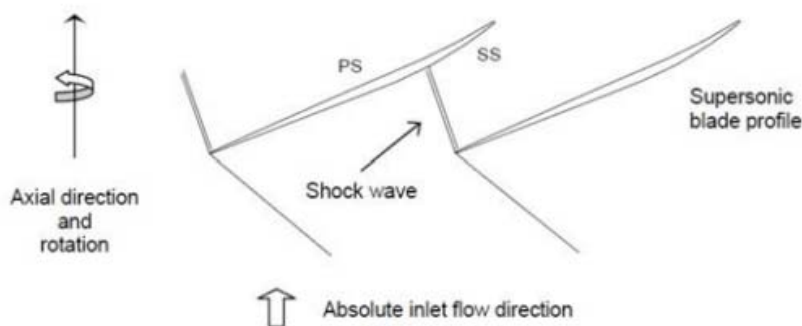


FIGURE 2.11: Shock wave in a supersonic profile.

compressor has this particular blade shape:

- Suction side: is almost flat to prevent a large expansion of the flow that would lead to an even high even higher Mach number in front of the passage shock and therefore a large entropy production. In this first part the the diffusion is only due to the presence of the shock. Sometimes the suction surface is even negatively cambered to avoid such problem, even if the flow capacity is reduced. After the shock the suction side become a conventional cambered airfoil because the Mach number is lower than unity.
- Hub to Tip: the profiles are less and less cambered because over the outboard sections of the rotor dominates the shock system (the adiabatic efficiency is reduced) while in the inner section the flow is still subsonic. This results in growing pressure ratio from hub to tip giving two zone dominated by two diffusion mechanism.

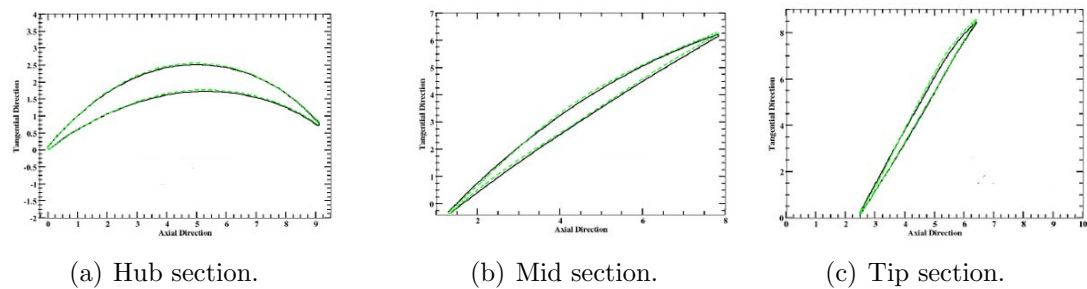


FIGURE 2.12: Section profiles of a transonic compressor.

2.2.3 Off-Design Shock Wave Structure

The shock pattern in Figure 2.11 represents the normal operating condition of the transonic compressor. However this shock wave pattern change as the operating condition varies. In fact if the back pressure is changed, keeping the rotation speed constant, the shock wave patten transforms as shown in Figure 2.13. Two different operating condition arise: one called near surge (stall) and the last one called near choking.

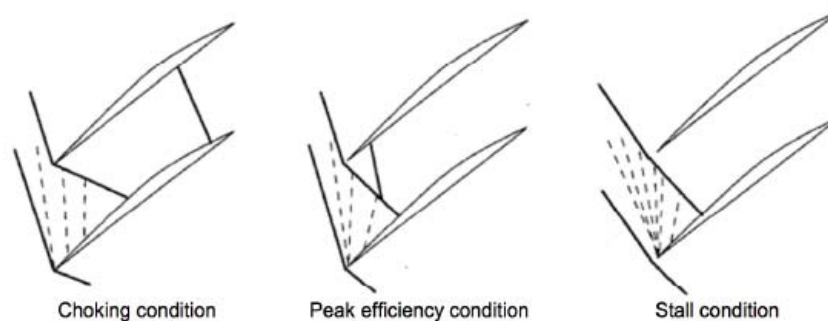


FIGURE 2.13: Shock wave pattern in a supersonic compressor in different operating condition.

- At low back pressure the flow is chocked, the massflow increase and shock fronts departing from the leading edge are rather oblique. This wave enters the blade passage and impinges well back on the suction side: therefore even if shock losses are rather low the interaction leads to the complete separation of the flow. Thanks to the presence multiple shock fronts, shock losses are not high, however as the absolute velocity is very high, profile losses lower considerably both efficiency and pressure ratio.

- At "medium" back pressure the flow is at his peak efficiency and occurs when the shock is just inside the rotor.
- At hight back pressure the flow is stalled, the massflow decrease and the shock is ejected from the passage channel and becomes almost normal to the incoming flow. Shock losses and supersonic turning are inevitably high: mass flow rate rapidly falls together with efficiency, even if pressure ratio remains high.

2.2.4 Transonic Compressor Losses

The interaction between the rotor's blades and the shock wave leads to aerodynamic losses but if its shape is accurately controlled these losses are not so hight. What cannot be controlled and it is difficult to measure are the indirect losses caused by the shock. These are for example the interaction with the boundary layer, the tip leakage vortex and, more generally, with secondary flows. The most important is the tip leakage vortex since the transonic compressor are unshrouded and highly loaded machines. The pressure imbalance is so hight, between pressure and suction side, that drives the flow from one side to the other, through the tip gap region as shown in Figure 2.14. The result is the formation of a vortex that increases aerodynamic losses and could lead to blockage near the casing and instabilities. This interaction is retained to be one of the principal phenomena bringing to stall in transonic compressors. In fact, the vortex is forced to slow down passing through the shock front and if the deceleration is too strong the vortex might break down. Another type of losses are the hub corner losses. This loss is positioned near the suction side of the blade hub and it is related with a viscous effect of the boundary layer, by which the flow migrates towards the tip wall.

2.3 Rotor 67

The Rotor 67 (R67) developed by NASA is a transonic low aspect-ratation fan. This fan will be used to better understand the interaction between the s-duct and the fan. The main thecnical data, referred to the design operative point, are reported

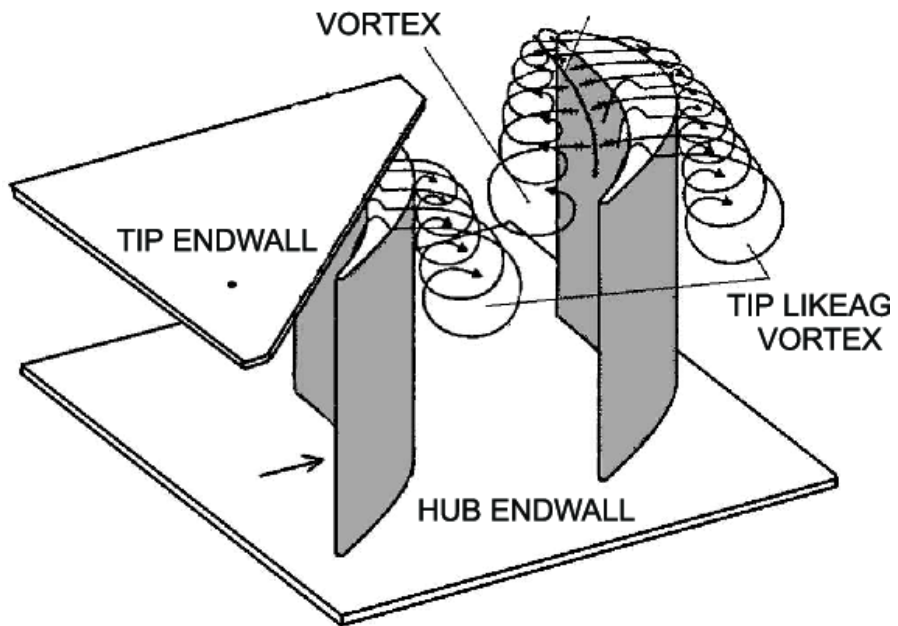


FIGURE 2.14: Tip leakage vortex.

in table. It was decided to use this fan because it has been widely studied and many blade optimization have been done.



FIGURE 2.15: Rotor 67.

TABLE 2.1: Nasa Rotor 67 Specifications.

Properties	Value
Design Rotational Speed	16043[<i>rpm</i>]
Number of Blades	22
Total Pressure Ratio	1.63
Mass Flow Rate	33.25 [$\frac{kg}{s}$]
Tip Velocity	429 [$\frac{m}{s}$]
$M_{relinlet}$	1.38
Shroud Tip	0.1016 [<i>cm</i>]

Chapter 3

Optimisation

This chapter is meant to give basic knowledge of optimisation problems. The latter can be found in many fields of studies, especially Engineering and Economy fields. To give a simple example let's consider a salesman who has to sell goods to customers in different cities. The optimisation problem lies in finding the shortest route that passes through every city. The more cities are introduced, the more complicated and highly non-linear the problem will become. Apart from this, also the boundary conditions have to be taken into account and the problem gets more complicated. To solve an optimisation problem we can use general automated design techniques that are implemented in cycles (loops). In computer programming, a loop is a sequence of instructions that are continually repeated until a certain condition is reached. Cycles are generally composed of three main processes: *design analysis*, *results evaluation* and *new design creation*. As stated in [18] the *design analysis* process is to determine the response of a specified design when it is subjected to a certain combination of input parameters. An example is to find the output pressure recovery of an S-duct as a result of certain fluid property inputs at the inlet area. The *results evaluation* process is used to verify if the last design is optimum and in the end the *new design creation* process is used to create a new design for the next iteration. To do the last two steps efficient algorithms are required in order to reduce the computational cost. Also an important evaluation of manufacturing constraints has to be done. For example we know that a really thin rotor blade offers good performance but under a certain thickness the blade will break. In a numerical optimisation, the design variables are those parameters that can be changed in the system while the code is searching for the best design that minimize or maximize one or more

specific characteristics called objective functions. In mathematical terms, a simple deterministic optimisation problem can be stated as follows: given an independent variable $x \in \mathbb{R}$ called design variable, and an objective function $f(x)$, the goal of a optimisation cycle is to automatically change the design variable in order to find a certain x^* such that $f(x^*)$ is a global minimum or maximum (it depends on the problem we are analysing). In a more general case, x can be a design vector of design variables $\mathbf{x} = (x_1, \dots, x_n) \in \mathbb{R}^n$. The optimisation is called *single-objective* (SOO) if only one objective function is present, otherwise is called *multi-objective* optimisation (MOO). It has to be underline also that a global optimum design might even not exist for complex problems: in these situations a *decision maker* comes into play by choosing one solution that may be of particular interest with respect to the others.

3.1 Problem Formulation

One of the difficult part of an optimisation process is the selection of design variables, constraints, objectives, models and uncertainties. The design variables are entities that can change the shape or properties of the model within a specified range during a sensitivity or optimization design study. The design variables that are created affect only the shape of the model. As a very simple example, consider a rectangular wing with a pre-defined airfoil. It can be defined by deciding on the values of the following two design variables:

$$(b, c) \tag{3.1}$$

Placing these variables along orthogonal axes defines a design space, or set of all possible design options. Each point in the design space corresponds to a chosen design, as illustrated in Fig. 3.1 The design variables are often bounded, so they usually have an upper and a lower limit. In the end they can be continuous, discrete or boolean. In our case of studies the control points of a parametrized S-duct can be considered design variables. After this the constraints have to be decided. A constraint is a condition that must be satisfied to make the design feasible and is imposed by the designer. Constraints can be either hard constraints, which set conditions for the variables that are required to be satisfied, or soft constraints, which have some variable values that are penalized in the objective function if, and based on the extent that, the conditions on the variables are not satisfied.

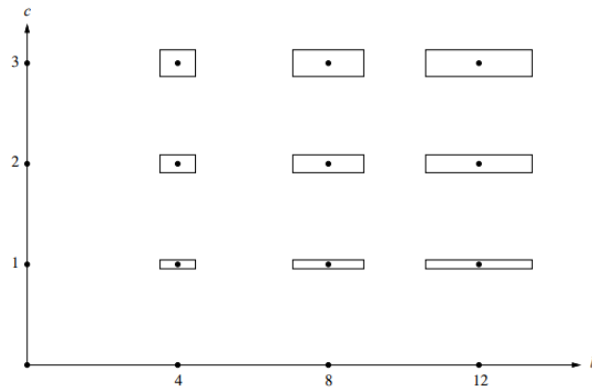


FIGURE 3.1: Representation of the Design Space.

Examples of constraints in a S-duct design can be related to manufacturing. Or, if after an iteration, the result of one or more objective functions exceed a certain value. The objective function is a mathematical equation that describes the output target. The latter corresponds to the maximization or minimization of profits or losses with respect to production. It then uses the correlation of variables to determine the value of the final outcome. Many solution methods have only one single objective function. But other methods allow multi-objective optimization, such as the calculation of a Pareto front. If the designer wants to avoid the MOO he can create a new objective function based on the previous one and use a weighted sum where each weight describes the influence of every objective function. In the end the optimization has to be chosen. Optimization models can be classified in terms of the nature of the objective function and the nature of the constraints. Special forms of the objective function and the constraints give rise to specialized algorithms that are more efficient. From this point of view, there are four types of optimization problems, of increasing complexity.

- Unconstrained: Is an optimization problem where the objective function can be of any kind (linear or nonlinear) and there are no constraints.
- Linear: Is an optimization problem with an objective function that is linear in the variables, and all constraints are also linear
- Quadratic: Is an optimization problem with an objective function that is quadratic in the variables (i.e. it may contain squares and cross products of the decision variables), and all constraints are linear.

- **Nonlinear:** Is an optimization problem with an objective function that is an arbitrary nonlinear function of the decision variables, and the constraints can be linear or nonlinear

These models can also be empirical models or theoretical models. The selection of the model determines the accuracy of the solution and the computational cost.

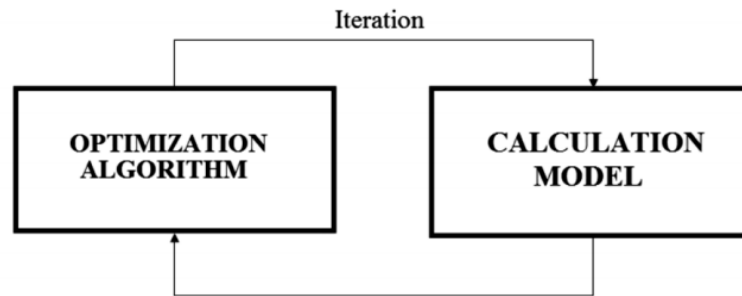


FIGURE 3.2: Scheme of an Optimization Problem.

3.2 Single and Multi-objectives problems

Once we set all the design variables, constraints, objectives and the models, the designer has to choose how many objectives function wants to study. With only one objective function the goal will be to minimise or maximise function; with two or more the designer has to choose a trade off solution. Based on this, single and multi-objectives optimisation problem can be expressed in a deterministic mathematical problem.

3.2.1 Deterministic Optimisation Problem

Definig an objective function $f(\mathbf{x})$, where $\mathbf{x} \in \mathbb{X}$ represents vector of design variables. A *single-objective* minimisation problem is formulated as:

$$\begin{cases} f(\mathbf{x}^*) \leq f(\mathbf{x}) & \forall \mathbf{x} \in \mathbb{X} \\ s.to & g(\mathbf{x}) \leq 0, h(\mathbf{x}) = 0 \end{cases} \quad (3.2)$$

where $g(\mathbf{x})$ and $h(\mathbf{x})$ are constraints vectors and \mathbb{X} is the design space. A deterministic *multi-objective* minimisation problem can be formulated as

$$\begin{cases} \min_{\mathbf{x}} [f_1(\mathbf{x}); f_2(\mathbf{x}); \dots f_m(\mathbf{x})] & \forall \mathbf{x} \in \mathbb{X} \\ \text{s.t.} & g(\mathbf{x}) \leq 0, h(\mathbf{x}) = 0 \end{cases} \quad (3.3)$$

where, like before, $g(\mathbf{x})$ and $h(\mathbf{x})$ are constraints vectors and \mathbb{X} is the design space. In the first system is important to underline that the objective function is only one and there's no uncertainties input ζ . On the other hand, in the second system a set of objective functions are minimise or maximise $[f_1(\mathbf{x}); f_2(\mathbf{x}); \dots f_m(\mathbf{x})]$ where $\mathbf{x} \in \mathbb{X}$ represents a vector of design variables. The MOO has the problem that it does not ensure that all the objective functions are minimized. In Fig.3.3 we can see an example of multi objective optimisation where x_1 and x_2 are the two objective functions.

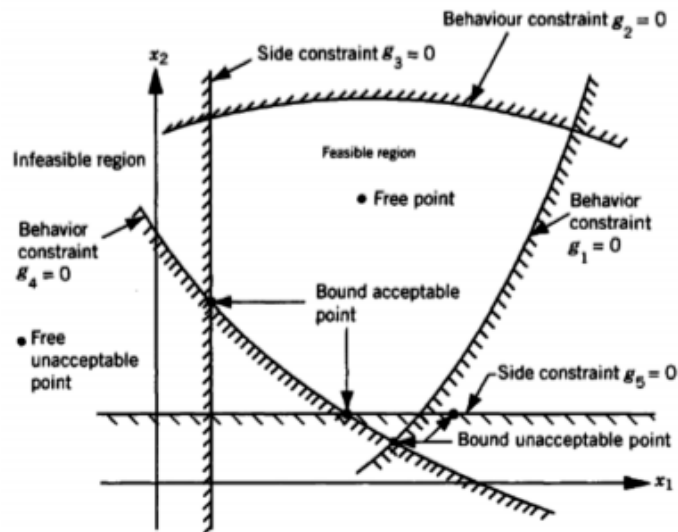


FIGURE 3.3: Example of MOO with constraints.

3.2.2 Concept of Dominance and Pareto Front

To affirm that a solution **A** dominates the solution **B** the following statements have to be verified:

- The solution **A** is not worse than the solution **B** in each objective function. What just asserted means that $f_j(A) \leq f_j(B) \forall j = 1, \dots, m$ where m is the number of the objective functions.
- The solution **A** is strictly better than the solution **B**, in at least one objective function. As a consequence, this means that $f_k(A) < f_k(B)$ for at least one k in $1, \dots, m$.

If none of these statements are verified, this means that both (**A** and **B**) are non-dominated solutions. The non-dominated solutions have the characteristic that if one objective function improves, the other has to become worse. In the Fig.3.4 we have a clear example where the points 6,5 and 3 are non-dominated points. The mathematical set that contains all the non-dominated solutions is called Pareto Front.

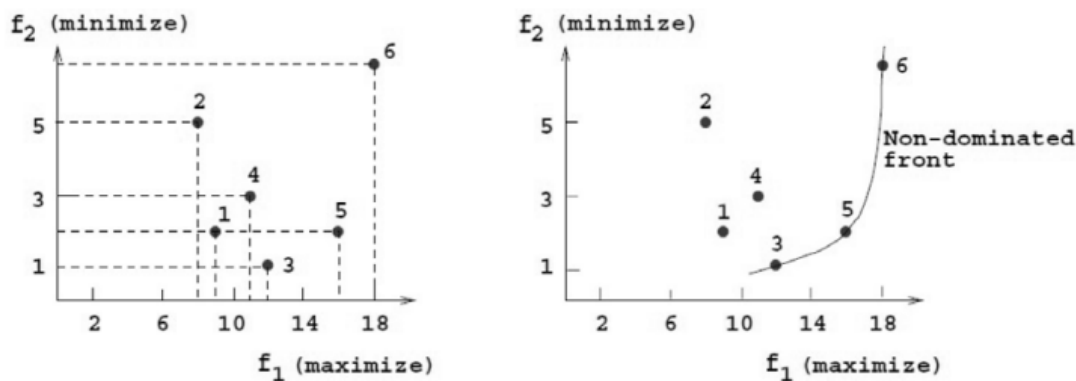


FIGURE 3.4: Example of non-dominated objective functions.

3.3 Optimization Algorithms

In order to find better solutions, the choice of the algorithm covers an important role. In fact, the aim of the algorithm is to decide how to change the decision variable. The most know algorithms are the exact algorithms. These algorithms always solve an optimization problem to optimality finding the exact mathematical solution. To find the exact mathematical solution is not easy and sometimes

impossible. For some application there are exact algorithm but the best known exact algorithms require exponential time. Another type of algorithm are heuristic algorithms. Heuristic means to find or to discover by trial and error. These algorithms is designed to solve a problem in a faster and more efficient fashion than traditional methods by sacrificing optimality, accuracy, precision, or completeness for speed. They are most often employed when approximate solutions are sufficient and exact solutions are necessarily computationally expensive. In the end there are the metaheuristic algorithms. Metaheuristics generally perform better than simple heuristics. The metaheuristic can be considered as a "master strategy that guides and modifies other heuristics to produce solutions beyond those that are normally generated in a quest for local optimality" [19]. In addition, all metaheuristic algorithms use a certain tradeoff of randomization and local search.

3.3.1 Metaheuristic Algorithms

In our thesis we are going to use the metaheuristic algorithms. Two major components of any metaheuristic algorithms are: intensification and diversification, or exploitation and exploration [20]. Diversification means to generate diverse solutions so as to explore the search space on a global scale, while intensification means to focus on the search in a local region knowing that a current good solution is found in this region. A good balance between intensification and diversification should be found during the selection of the best solutions to improve the rate of algorithm convergence. The selection of the best ensures that solutions will converge to the optimum, while diversification via randomization allows the search to escape from local optima and, at the same time, increases the diversity of solutions. A good combination of these two major components will usually ensure that global optimality is achievable [21]. To intensify and differentiate the design space, the algorithm has to make a decision that can be based on:

- non-preference methods: The new design is chosen randomly, without any strategy.
- priori method: All the designs have been already chosen without waiting the results of the simulations. The main problem with this type of method is that it may have too optimistic or too pessimistic expectations, because the decision maker unknowns the results.

- posteriori method: The new design is chosen after every iteration analysing the results. In order to do that, it is created a Pareto-optimal set but the main drawback is the computational cost that is requested.

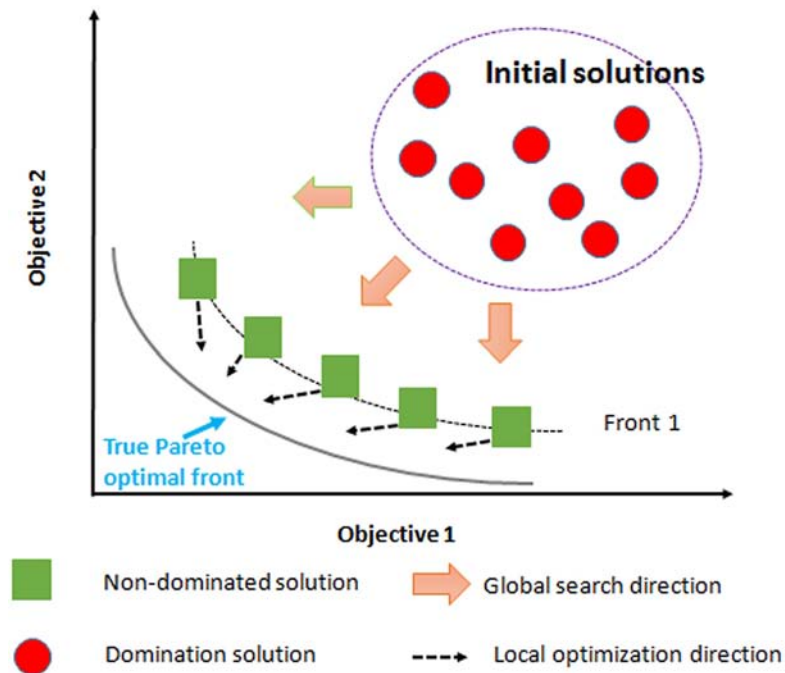


FIGURE 3.5: Posteriori Method and Pareto Front.

- interactive methods: These methods allow the user to interact with the simulation and guide the solution.

A posteriori method will be used in our optimisation. In literature exist many metaheuristic algorithms for optimization, such as Simulated Annealing, Genetic Algorithms, Differential Evolution ecc.. In this thesis we are going to use the Tabu Search algorithm.

3.3.2 Tabu Search

Tabu search was developed by Fred Glover in the 1970s, but his seminal book was published much later in 1997. The search history is a major component of the method and uses memory. In essence, Tabu search can be considered as an intensive local search, and the appropriate use of search history avoids revisiting local solutions by recording recently tried solutions in tabu lists. Over a large

that is decided by the user. Then the optimiser evaluate all the objective functions for all the non tabu points. The point x_{i+1} that has better objective function will be the new starting point for the next iteration. If during the evaluation on the new points created, more than one is a non-dominated point, one of them will be chosen randomly, while the other will be recorded in the Medium Term Memory.

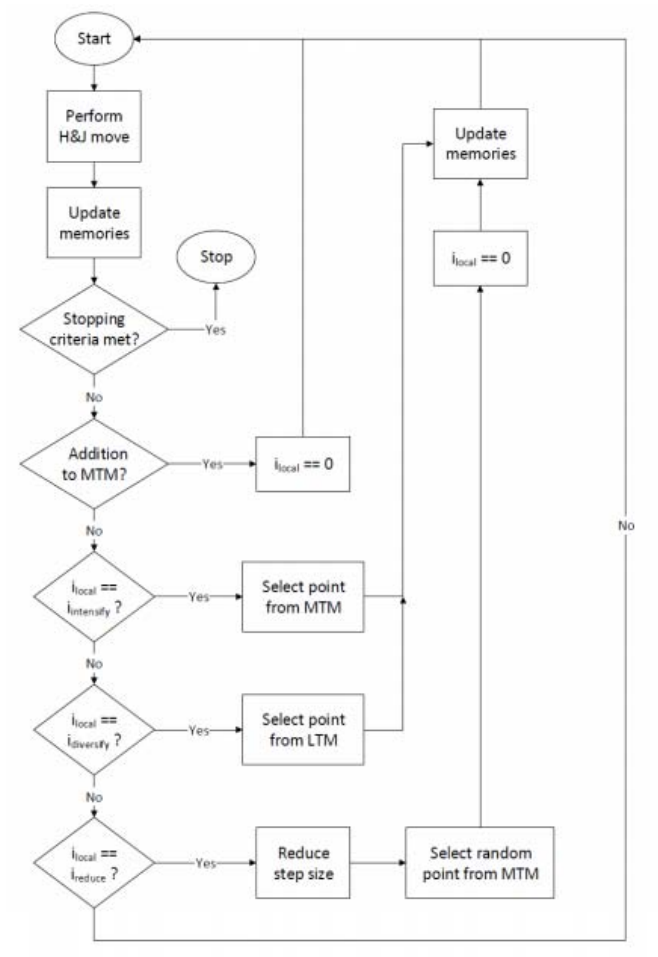


FIGURE 3.7: Flow diagram of the MOTS algorithm.

Chapter 4

S-Duct case of study

The aim of this work is to find a way to reduce the computational cost of the s-duct and rotor 67 coupled system. As we know the total pressure distortion caused by the s-duct does not allow us to study only one blade of the rotor 67 but instead we have to simulate the full annulus. In order to do that, as already discovered in Marco's work [15], a symmetry studies of the total pressure at the AIP of the s-duct has to be done. Hence a new objective function has to be created and as starting point it will be used the geometry studied from Davide's [1] and Marco's [15] works. The code and the optimisation loop are the ones used in [14] and in this chapter the geometry of the baseline, the parameterization, the mesh and the CFD parameters will be analysed.

4.1 Geometry

The geometrical model implemented as baseline configuration was designed as defined in Wellborn experiment and scaled up to adapt it to the rotor 67 geometry. The duct centerline is defined by two planar circular arcs with same radii, R , and subtended angles, $\theta_{max}/2$. Its coordinates are defined by the following equations: for $0 \leq \theta \leq \theta/2$

$$x_{cl} = R \sin \theta \tag{4.1}$$

$$y_{cl} = R \cos \theta - R \tag{4.2}$$

$$z_{cl} = 0 \tag{4.3}$$

for $\theta/2 \leq \theta \leq \theta_{max}$

$$x_{cl} = 2R \sin(\theta_{max}/2) - R \sin(\theta_{max} - \theta) \quad (4.4)$$

$$y_{cl} = 2R \cos(\theta_{max}/2) - R \cos(\theta_{max} - \theta) \quad (4.5)$$

$$z_{cl} = 0 \quad (4.6)$$

The radius of the section perpendicular to the centerline is a function of θ :

$$\frac{r}{r_1} = 1 + 3 \left(\frac{r_2}{r_1} - 1 \right) \left(\frac{\theta}{\theta_{max}} \right)^2 - 2 \left(\frac{r_2}{r_1} - 1 \right) \left(\frac{\theta}{\theta_{max}} \right)^3 \quad (4.7)$$

where r_1 and r_2 are the inlet and the outlet radius respectively. Both centerline and radius distribution are a function of the arc angle θ . The value of θ_{max} , R , r_1 and r_2 are the same of the Delot experiment but scaled up with a factor of 3.1295.

To obtain more accurate results there are:

TABLE 4.1: S-Duct baseline geometry parameters.

Parameter	Value
θ_{max}	60°
R	$0.6650m \cdot 3.1295$
r_1	$0.0665m \cdot 3.1295$
r_2	$0.0820m \cdot 3.1295$

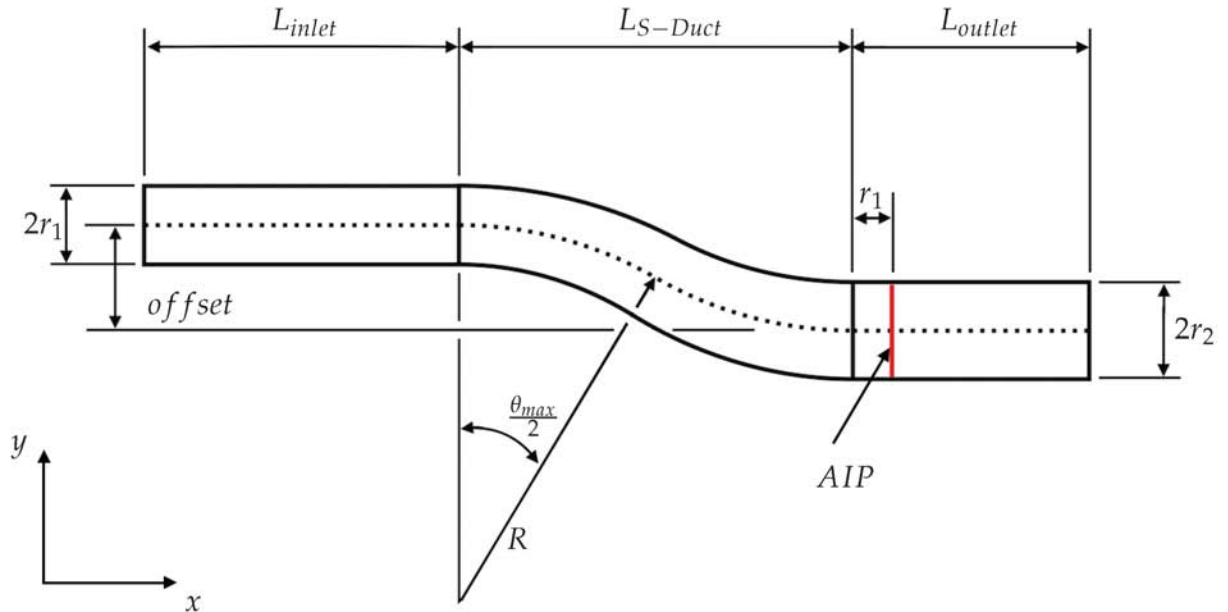


FIGURE 4.1: S-duct Scheme.

- at the inlet, a cylindrical duct eight times longer than the inlet radius. Its purpose is to ensure uniform inlet conditions;
- at the outlet, a cylindrical duct six times longer than the outlet radius. Its purpose is to guarantee that the outlet conditions do not have any influence on the upstream flow.

In the table 4.2 all the value of the main parameters are reported. In the end

TABLE 4.2: Overall geometry parameters.

Parameter	Value
Offset	$2R(1 - \cos(\theta_{max}/2))$
L_{SDuct}	R
L_{inlet}	$8r_1$
L_{outlet}	$6r_1$
$L_{AIP} = L_{inlet} + L_{SDuct} + r_1$	$9r_1 + R$
$L_{TOT} = L_{inlet} + L_{SDuct} + L_{outlet}$	$14r_1 + R$

only half of the s-duct has been simulated due to the simmetrical flow dicover by Wellborn [?] and Delot [?].

4.2 Parameterization

In this research it has been used the same parameterization of the Wellborn S-duct studied by D'Ambros [14]. The reasons behind this choice are mainly two: first because this parameterization results in a great improvement of the previous ones. Second because it has been used in the previous work of [1],so we have the opportunity to compare the results. The entire parameterization is based on the Free Form Deformation (FFD) technique. In computer graphics, free-form deformation (FFD) is a geometric technique used to model simple deformations of rigid objects. It is based on the idea of enclosing an object within a cube or another hull object, and transforming the object within the hull as the hull is deformed. Deformation of the hull is based on the concept of so-called hyperpatches, which are three-dimensional analogs of parametric curves such as Bézier curves, B-splines, or NURBs. As visual example it can be viewed as the entire geometry that has to be parametrized that has been incorporated in a 3D lattice, and the latter is divided into regular sections, and the nodes of every section are

called control points. The points of the geometry are linked to the control points since their position is described by a weighted sum of the control points. Two simplifications have been made in order to improve the method:

- The S-duct has a symmetry plan (x-y),so only half S-duct has been simulated in order to reduce the computational cost.
- The inlet and the outlet cylindrical tube are fixed so it is not necessary to parameterize them.

The parallelepipedic lattice has been created from a planar rectangular plane. To

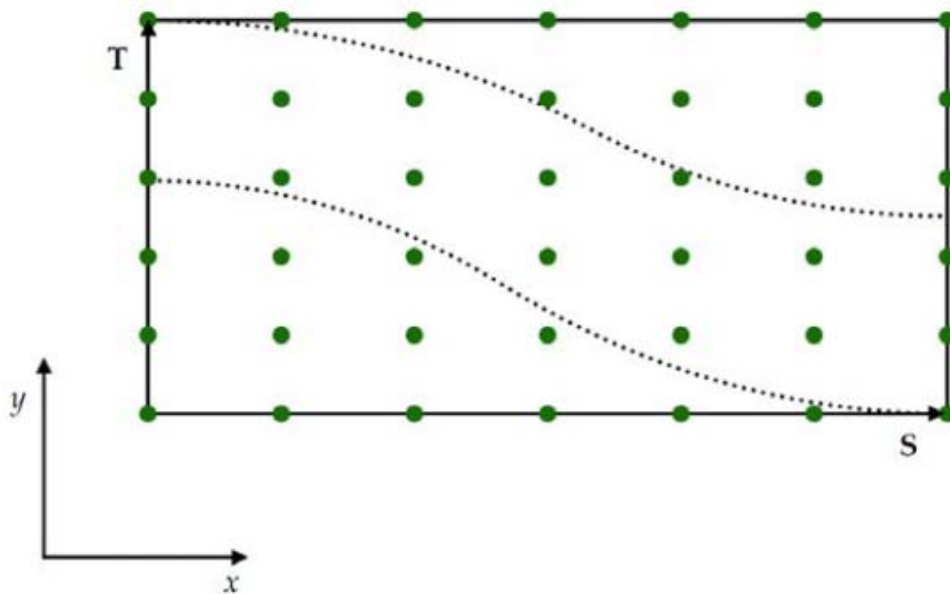


FIGURE 4.2: S-duct parallelepipedic lattice.

links the control points and the geometry the FFD method is mathematically described by the following equation:

$$X_{ffd} = \sum_{i,j=0}^{l,m} B_i(s)B_j(t)P_{ij} \quad (4.8)$$

Where:

- X_{ffd} is a vector containing the Cartesian coordinates of the displaced point;
- l, m are the number of control point in S and T direction respectively;

- $B_k(u)$ are the degree 3 Bernstein polynomials;
- s, t are the generic point coordinate in the S T system of reference ($0 \leq s \leq 1, 0 \leq t \leq 1$);
- P_{ij} is a vector containing the Cartesian coordinates of the control point.

Now selecting a S section, and moving the control points, in correspondence to the S-duct surface, the geometry obtained results similar to the baseline but not equal as shown in Figure 4.3. The main problem is that the control points do

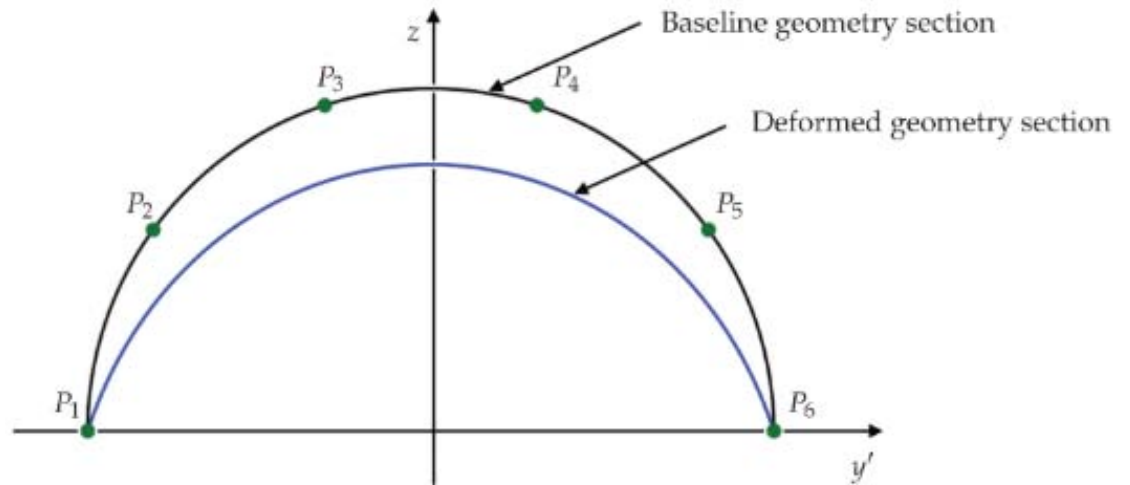


FIGURE 4.3: Difference between baseline and deformed geometry.

not interpolate the surface. To obtain a closer result, it is possible to invert the equation of a Bezier curve, since for a fixed section, the geometry can be described with a 1D FFD formulation (Bezier curve) as follows:

$$X_{ffd} = \sum_{i=0}^m B_j(t) P_i \quad (4.9)$$

But, as [14] discover, to invert the equation some constraints have to be imposed:

1. $y'_{p1} = -r$
2. $y'_{p6} = r$ tangency condition
3. $y'_{p1} = y'_{p2}$ symmetry condition
4. $y'_{p5} = y'_{p6}$ symmetry condition
5. $y'_{p3} = -y'_{p4}$ symmetry condition

6. $z'_{p3} = z'_{p4}$ tangency condition
7. $z'_{p2} = z'_{p5}$

In order to guarantee tangential condition at the inlet and at the outlet, the control points in the inlet section are copied and translated shortly after. The control points in the outlet section are copied and translated shortly before. The control points of the cross sections of the inlet and the outlet are fixed for manufacturing constraints. The degrees of freedom (dof) of the parameterization can be defined as follow:

- P1 and P6 that can only move along x-y, in order to respect the symmetry (2dof);
- P2 and P5 that, in order to respect the tangential conditions, they have the same x and y as
- P1 and P6. As a result, they only have one direction to move (1dof each);
- P4 and P5 are free to move (3dof each).

These above mentioned conditions can be applied to all the sections. Each cross-section at the end has twelve dof and so three cross section have been performed in the s-shape, and this means that l is equal to 7.

4.3 Mesh

Solving the continuous non-linear fluid-dynamics equations is not possible. So it is necessary to approximate the domain with nodes, connected in a cells network, and the equations are solved algebraically. The mesh can be divided in two types: unstructured and structured. The latter is the most difficult to build but since volumes are aligned with streamlines, it improves the solver convergence. To built the mesh, it was decided to use the one already created by D'Ambros [14]. The software used to generate the mesh every iteration is ICEM. The mesh has been created with the same topology as [14] and to create a structure mesh it was use the blocking technique. Due to the scaling up the number of mesh elements change from $1.8 \cdot 10^6$ to $3.2 \cdot 10^6$ An H-grid structure was imposed in the center of the

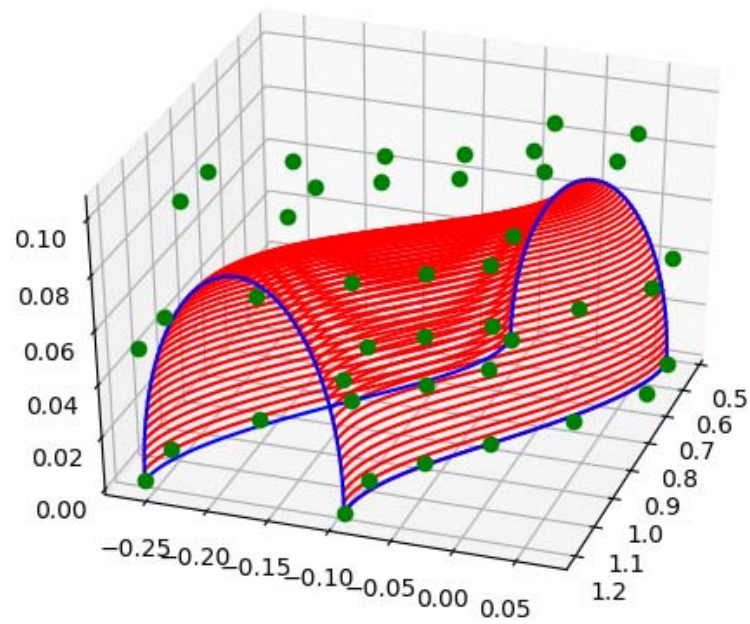


FIGURE 4.4: Overview of Parameterization.

duct section and an O-grid structure around the walls. This type of mesh allow to better simulate the detachment of the flow. In fact the mesh density grows near the wall as you can see in Figure 4.6 and in Figure 4.7.

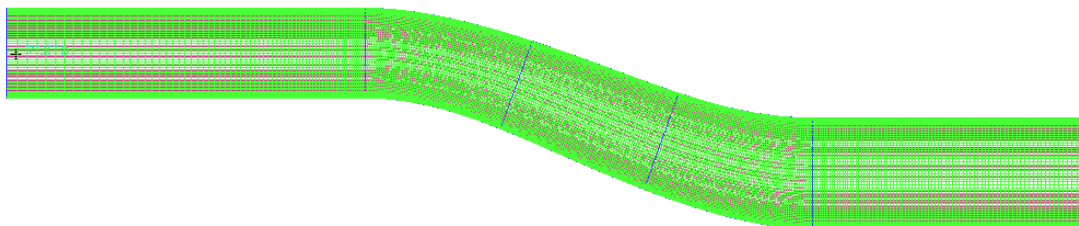


FIGURE 4.5: Overview of the s-duct mesh.

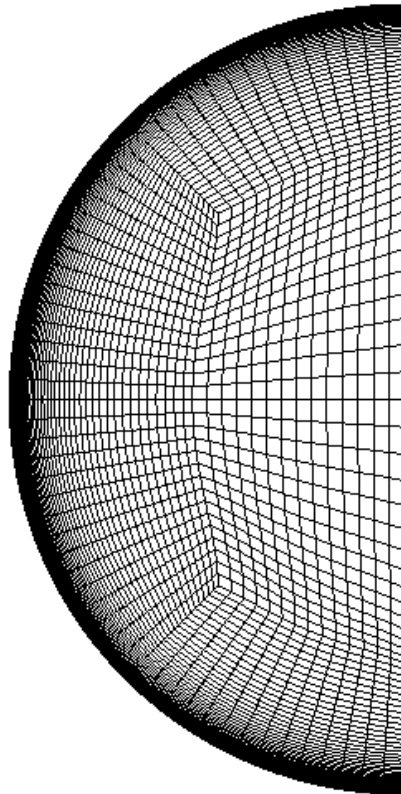


FIGURE 4.6: Inlet and Outlet Surface Mesh.

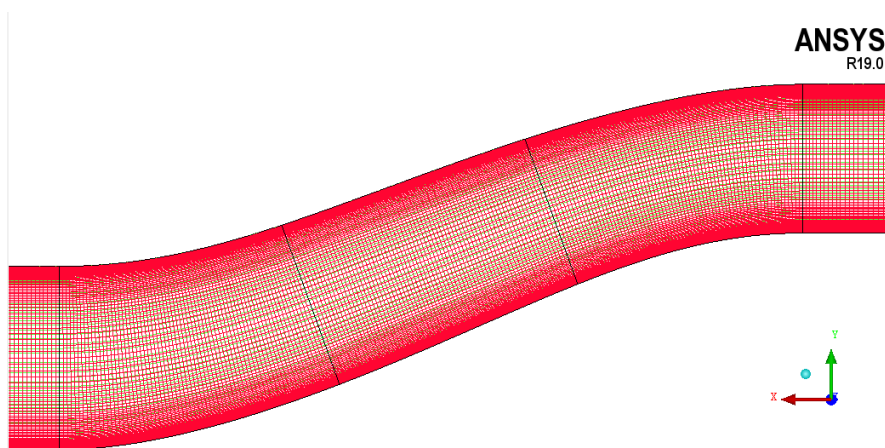


FIGURE 4.7: Symmetry plane mesh of the S shape.

4.4 CFD Analysis

The analysis were carried with the ANSYS Fluent solver. Due to the low computational cost it was decided to do a steady state RANS simulation and to better mach the experimental data the turbulence model that was chosen is the $K - \omega$ SST. The number of iterations is fixed to 200 with the first order and 500 with the second order, in this way the residuals can go below 10^{-5} . The boundary conditions are the one found by [1] due to the scaled up geometry and are reported in table 4.3.

TABLE 4.3: Boundary Conditions.

Parameter	Value
Inlet static pressure	77819 Pa
Inlet total pressure	106390Pa
Outlet static pressure	88822 Pa
Total temperature	288.2 K

4.5 Optimization Loop

In this section the optimization loop will be briefly discussed. The optimization starts with an initial design vector, then the initial geometry is parameterized, defining variable vector size and control points location. After, the geometry and its mesh are generated in ICEM. Then, the 3D model is imported in Fluent solver, the simulation is set up and run. In the end, the objective functions are evaluated from simulation results with a Python script, and provided the optimiser to generate a new design vector, closing the loop.

4.6 Objective Functions

As already said in Chapter 2, the MOTS allows to analyse more than one objective functions. Unlike previous work that use 3 types of objective function: pressure losses, swirl and DC60; in this work the pressure losses and the DC60 will remain but a new objective function to analyse the symmetry of the flowfield at the AIP

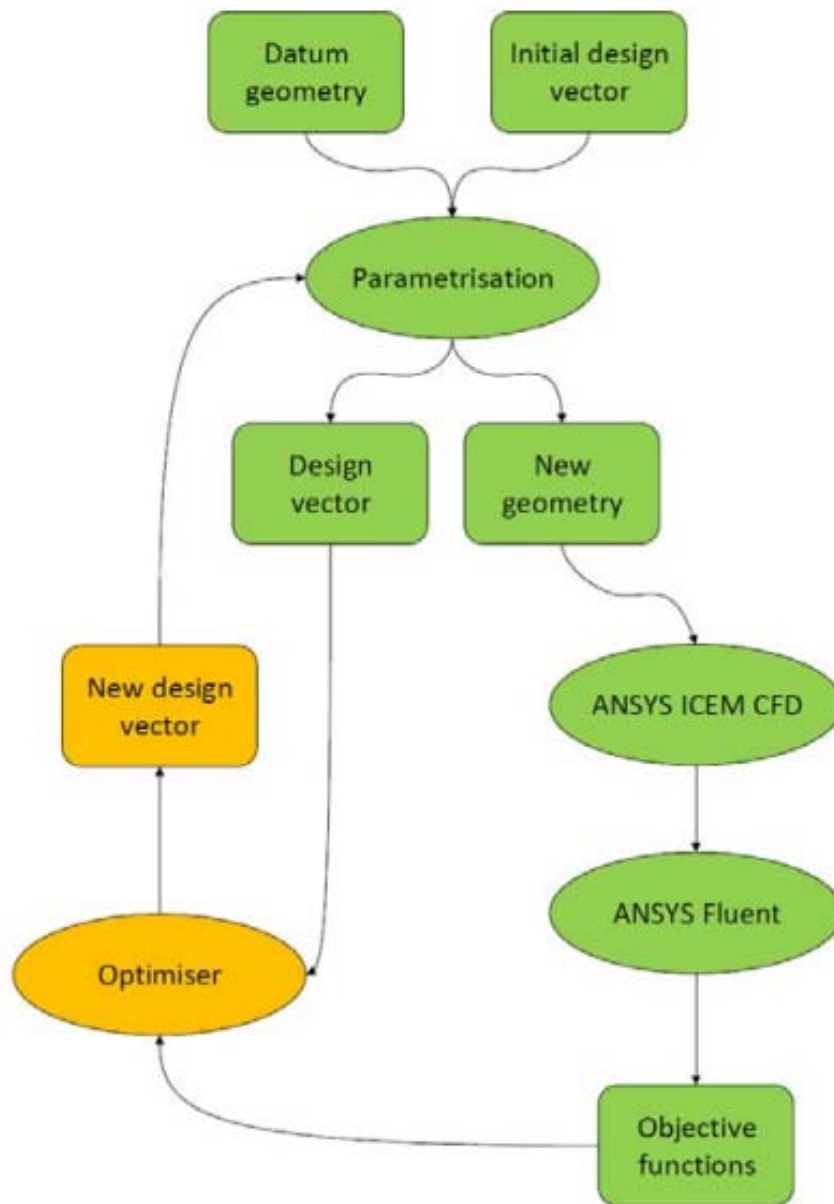


FIGURE 4.8: MOTS loop.

has to be created. This new objective function will be called Symmetry maximum error.

4.6.1 Pressure Losses

Total pressure losses have been already described in Chapter 1. This parameter describes these pressure drops and it is calculated with an area-averaged method.

$$PR = \frac{P_{tot,out}}{P_{tot,in}} \quad (4.10)$$

PR coefficient should be maximized for reducing pressure losses within the duct but the optimization problem is designed to minimize the goals, so the objective function has to be defined as follow:

$$CP = 1 - PR \quad (4.11)$$

4.6.2 DC60

The DC60 help to reduce the pressure distorsion and since it is defined as:

$$DC\theta = \frac{P_{tot,AIP} - P_{tot,\theta}}{q_{f,AIP}} \quad (4.12)$$

we can keep the DC60 as objective function to be minimize.

4.6.3 Symmetry Maximum Error (S.M.E.)

The Symmetry maximum error measures the difference of total pressure between every symmetric point of the S-duct mesh. The final ojective is to have the same blade loading for every 22 blade of the rotor and to reduce the vortices strenght. This task is really difficult to achieve since due to the S-duct at the AIP there will be always a Paired Swirl. The latter will strongly influence the flowfield because half of the fan will experience a co-rotating swirl and the other half will experience a counter-rotating swirl. Since the blade loading is heavily related to the inlet pressure profile and as proven by [15] the DC60 pressure distorsion help the symmetry, it was decided that the total pressure profile, and not the swirl, has to be symmetric. So the main objective is to have the same pressure profile between the top and the bottom. This can be achieve thanks to the mesh point by subtracting each symmetric point giving us a vector of pressure difference(or error). Since it is very expensive in term of computational time to reduce all the total

pressure difference between each point it was decided, after some testing, to reduce the maximum error of total pressure difference. To have a visual representation and to better understand the Symmetry maximum error objective function we can refer to Figure 4.9. The mesh at the AIP has 4480 nodes and it has been divided into two parts: the lower and the upper. Then the total pressure difference is calculated for each symmetric point, for example the two blue ones. After that it has been obtained a vector with 2240 total pressure differences. The absolute value of each difference has been taken and the maximum one has been extrapolated to be the objective function.

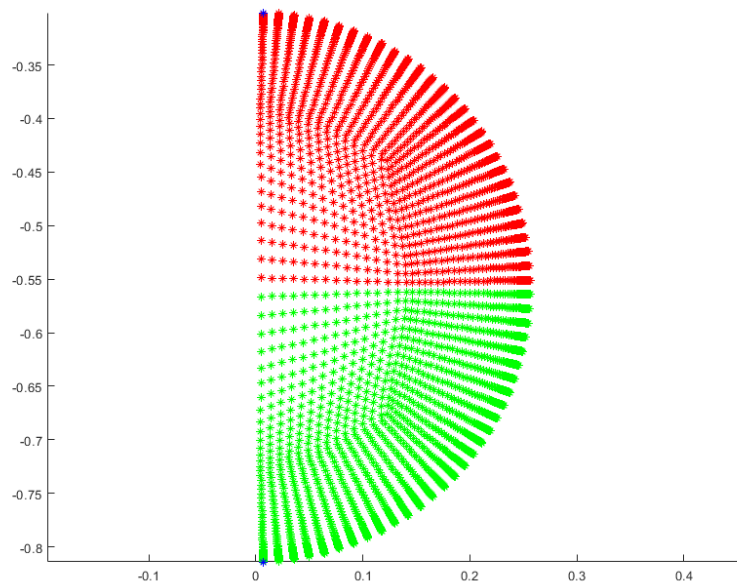


FIGURE 4.9: AIP mesh points.

Chapter 5

NASA R67 Computational Analysis

In this chapter it will be discussed the validation of the model carried out by Marco Tridente [15]. It is important to underline that this section briefly sums up the process and the results obtained by Marco. The validation process was done in two part:

- Validation of the single blade with different meshes
- Validation of the full annulus coupled with the ogive

The softwares used for every simulation are:

- CFX-TurboGrid for the generation of the mesh of the rotor
- CFX-Pre-Solver to set the parameters for the simulation
- CFX-Post to visualize the results and to do the post-processing
- SolidWorks to create the geometry of the ogive
- ANSYS workbench to create the mesh of the ogive

5.1 Single Blade Validation

5.1.1 Geometry and Mesh Creation

The geometry of the rotor was directly created in ANSYS CFX-Turbogrid, thanks to the coordinates of hub, shroud and profile (provided by NASA) that were properly formatted to act as input file for the the creation of the model. Then the

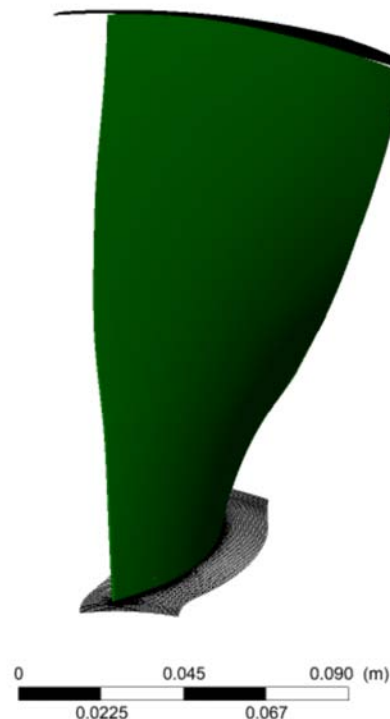


FIGURE 5.1: Geometry Frontal View.

computational grid was generated also in ANSYS CFX-Turbogrid. Three domains were created:

- Inlet: it keeps the fluid in his initial state
- Passage: it contains the blade itself
- Outlet: it captures what happens near the trailing edge and the effect of the wake

The passage domain is really complex since the simulation deeply depends on the mesh's quality. After the geometry creation and the tip gap setting, the topology

of hub and shroud were generated using the Automatic Topology and Meshing tool (ATM optimized). A number of intermediate layer were used to construct the 3D grid guiding the mesh through the spanwise. Many meshes were created in which the number of mesh elements varies to understand his influence on the results and, with a coarse mesh, save computational time.

TABLE 5.1: Comparison of different type of mesh implemented

	Number of Nodes
Coarse $k - \epsilon$	700k nodes
Coarse	900k nodes
Fine	1.8 mln nodes
Very Fine	2.0 mln nodes

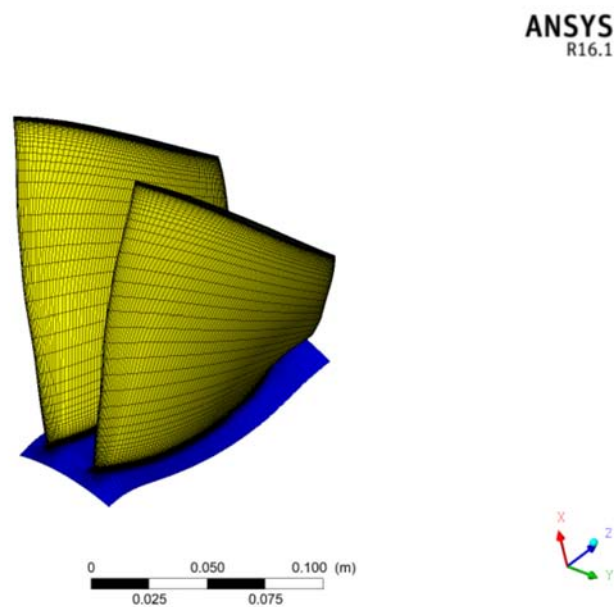


FIGURE 5.2: Mesh of the passage.

5.1.2 Simulation Set-Up

The software used to set-up the simulation was CFX-Pre-Solver. In the table below, all the main parameters are reported. The turbulence model used is the RANS(Reynolds Averaged Navier-Stokes Simulation), which is not that precise but the cost of the simulation is very lower. In particular, the model used is the SST $k - \omega$.

TABLE 5.2: CFX-Pre Set-up parameters

Ansys CFX Solver set-up		
Analysis Type	Steady State	
Domain	Domain Type	Fluid Domain
	Fluid and Particles Definition	Air Ideal Gas
	Reference Pressure	0 [atm]
	Domain Motion Option	Rotating
	Domain Motion Angular Velocity	-16043 [$revmin^{-1}$]
	Heat Transfer	Total Energy
	Turbulence Option	SST
	Wall Function	Automatic
	Wall Heat Transfer Model	High Speed
Boundary Condition	Hub	No Slip Wall
		Smooth Wall
		Adiabatic
	Shroud	Rotating Frame
		No Slip Wall
		C-R Wall
		Smooth Wall
		Adiabatic
		Rotating Frame
	Inlet	Subsonic
		Stat. Frame P_0
		101325 [Pa]
Normal to BC		
Stat. Frame T_0		
288.2 [K]		
Outlet	Frame Stationary	
	Subsonic	
	MFR or Pressure Variable	
Solver Control	Advection Scheme	High Resolution
	Turbulence Numerics	High Resolution
	No. Iteration	3200
	Timescale Control	Auto Timescale
	Convergence Criteria	MAX 1e-5

5.1.3 Validation's Results

In Figure 5.3 and 5.4 the results obtained with the 100% of the rotational speed are reported. In the x axis is reported the non-dimensional mass flow rate $\frac{\dot{m}}{m_{choke}}$. The experimental data almost match every model implemented but the error committed during the simulation varies from mesh to mesh. What has to be underline is the

optimal results obtained by the coarse mesh that are very close to the experimental one. In Table 5.3, it is important to notice that the coarse mesh with SST model

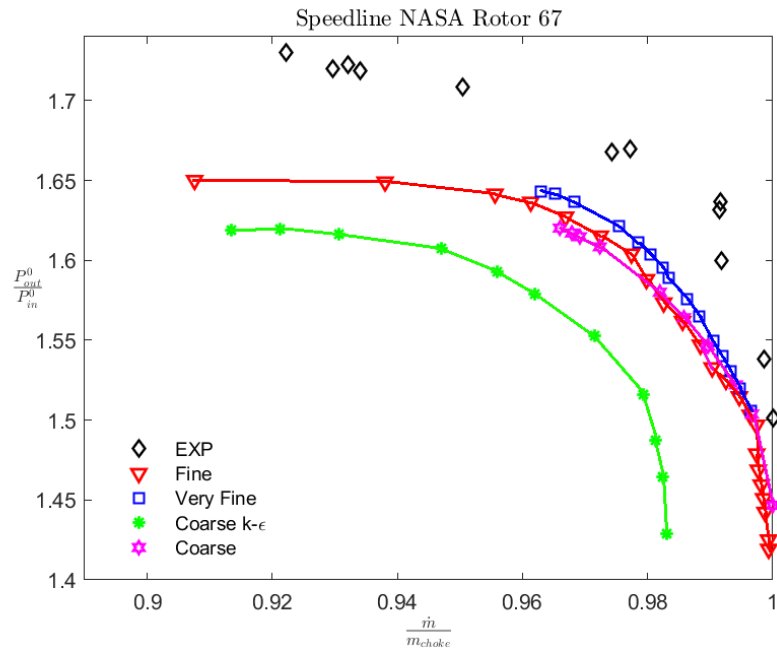


FIGURE 5.3: Compressor ratio with different mesh.

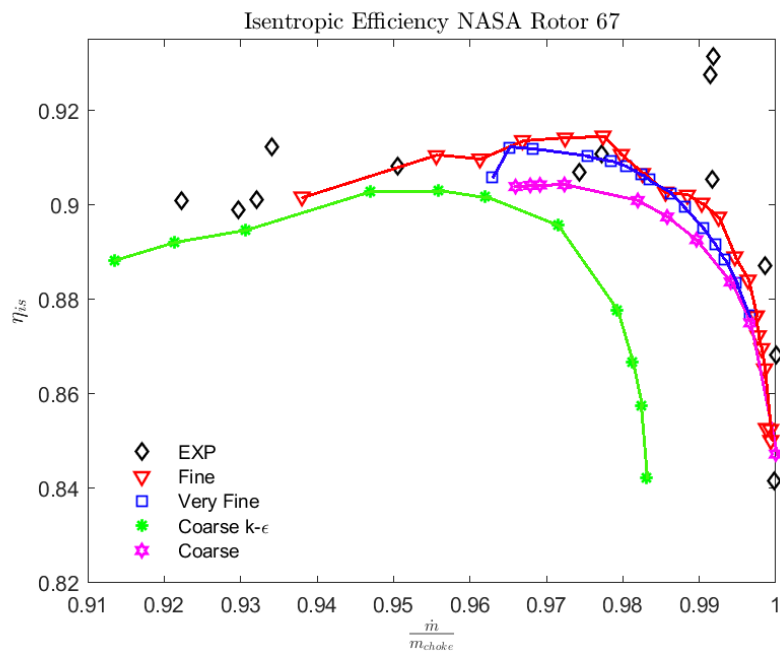


FIGURE 5.4: Isoentropic Efficiency with different mesh.

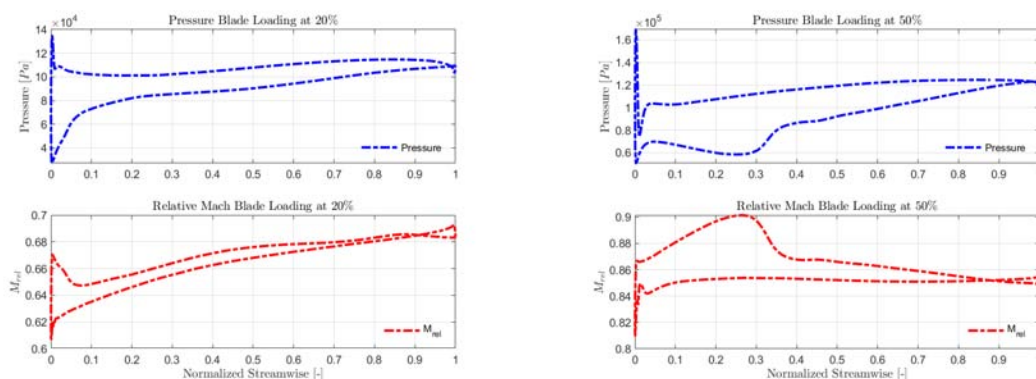
faithfully represents the phenomenon, and, from now on it will be used for further simulation since it is 1 million nodes lighter than the two fine meshes.

TABLE 5.3: Comparison of different type of mesh implemented

	Mass Flow Rate [$\frac{kg}{s}$]	Relative Error	PR	Relative Error
Design Point	33.25	-	1.63	-
Coarse $k - \epsilon$	33.4185	0.0051%	1.5929	0.022%
Coarse	33.2862	1.08e-3 %	1.6171	0.008 %
Fine	33.4047	0.0046 %	1.6272	0.0017 %
Very Refine	33.2366	4.03e-4%	1.6434	0.0082%

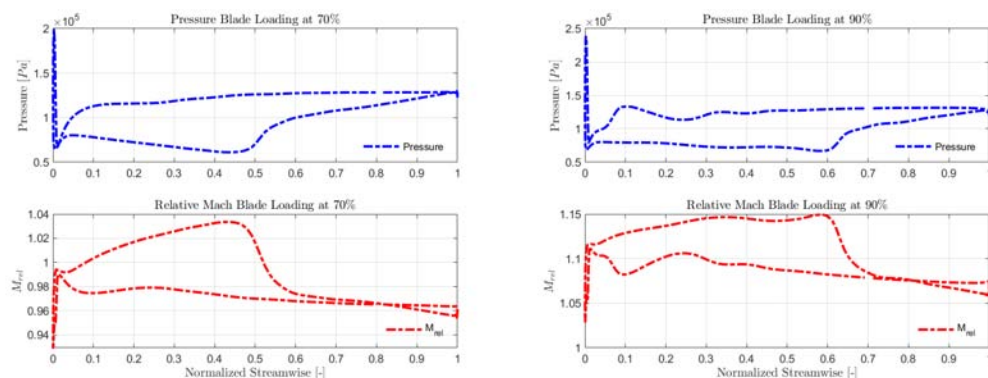
Now it is possible to analyse the behaviour of the shock waves and compare them with the experimental data.

In Figure 5.5, the curve of the Relative Mach and Pressure at different span



(a) Pressure and Relative Mach Blade Loading at 20.

(b) Pressure and Relative Mach Blade Loading at 50.



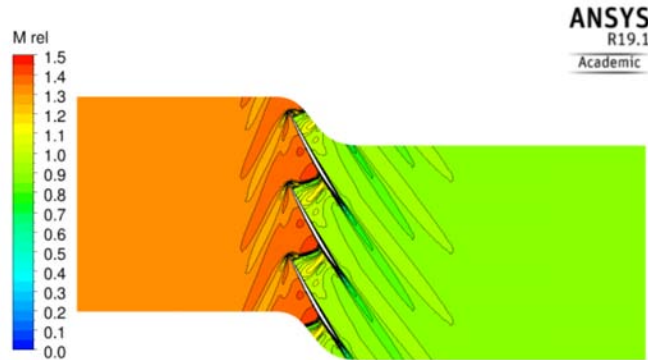
(c) Pressure and Relative Mach Blade Loading at 70.

(d) Pressure and Relative Mach Blade Loading at 90.

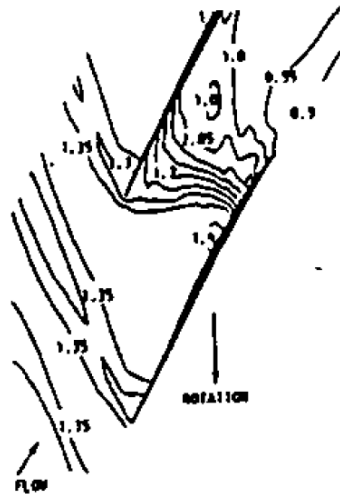
FIGURE 5.5: Pressure and Relative Mach Blade Loading at different span location.

location are represented. From the 50% of the span (Figure 5.5(b)), the shock wave phenomenon appear and grow stronger as the span increase due to the higher velocity ($(U = \omega \wedge r)$). This affects also the position of the shock as well; the wave,

indeed, tends to move towards the trailing edge as the % of span increases. Another important result can be seen in Figure 5.6. In fact, the shock wave behaviour perfectly matches the experimental results. The shock wave at the leading edge is able to reduce the number of Mach the unity, hence, no shock wave occurs in the channel. However in the choking condition the shock wave is not still enough to reduce the Mach below 1 and a second shock occurs between the blades as highlighted in Figure 5.7. In the end, the entire map of the compressor was



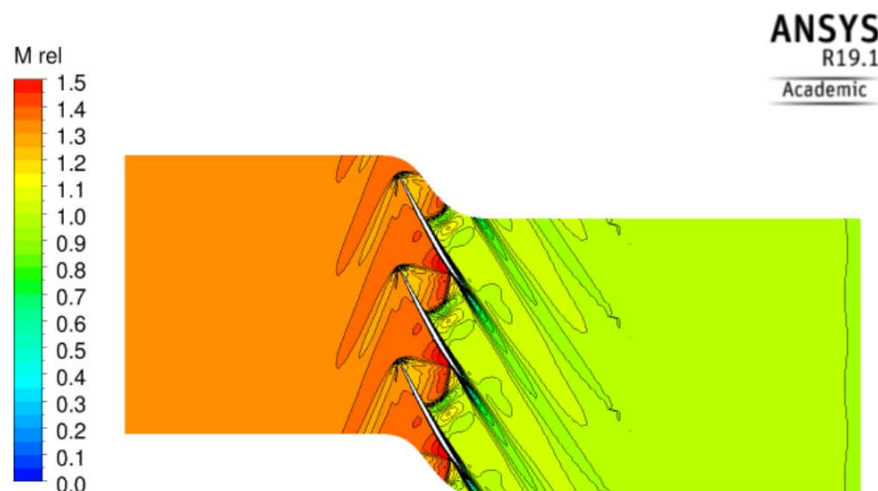
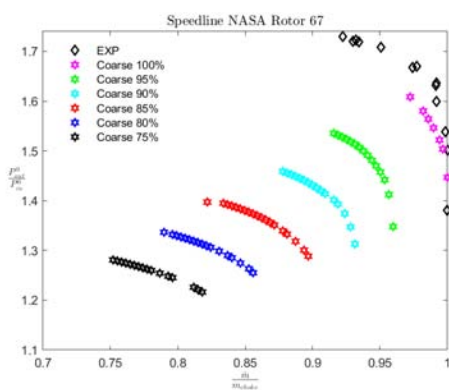
(a) Blade to blade Contour of M_{rel} near peak.



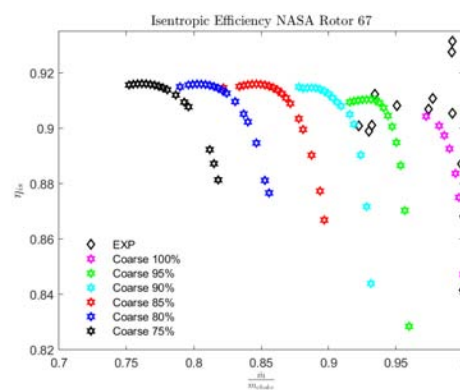
(b) Experimental blade to blade Contour of M_{rel} near peak.

FIGURE 5.6: Comparison between contours of M_{rel} of experimental and CFD near peak.

simulated (always with the coarse mesh) with the rotational speed ranging from 75% to 100%.

FIGURE 5.7: Contour of M_{rel} near choking condition.

(a) Compressor map NASA rotor R67.



(b) Isentropic efficiency NASA rotor R67.

FIGURE 5.8: Performance of the NASA rotor 67.

5.2 Full Annulus Validation

To match the S-duct and the fan, a full annulus simulation is required since the s-duct pressure profile at the outlet is not uniform. In this simulation the boundary conditions are the same as the single channel with a clean incoming flowfield (no distortion is generated), but the problem is the central hole that is created when the full annulus is assembled. For instance, when there is the revolution of the blades, the region of the shaft is left blank and this should be avoided. To close the hole, an ogive was implemented upstream of the fan to drive the air from the inlet towards the blades. The geometry was created on SolidWorks and the mesh was generated ANSYS workbench. Then the fan and the ogive were connected

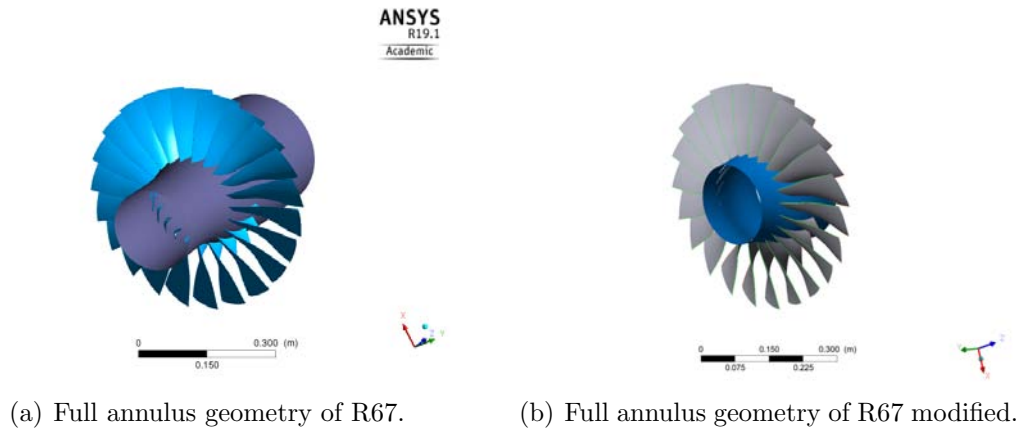


FIGURE 5.9: Full Annulus.

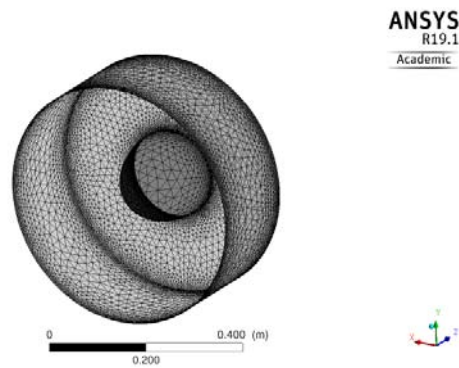


FIGURE 5.10: Ogive's mesh.

with the Frozen Rotor model because it has the lowest computational cost and because two frames remain in the exact relative same position. The drawback of this model is that transient effects are not taken into account. The pitch change option was set to Automatic to avoid errors. In Figure 5.11 it is possible to see the system assembled with three domains:

- Ogive: where the boundary conditions are set
- Rotor's blades
- Outlet: where the flow is analysed

The main problem of this type of simulation is the high computational cost. In fact, as reported in Table 5.4, to complete the simulation, it takes more than 14 hours with 16 processors (equivalent to 1 node on the cluster of Cranfield University).

Even for this validation a compressor map study was done but with only 95%

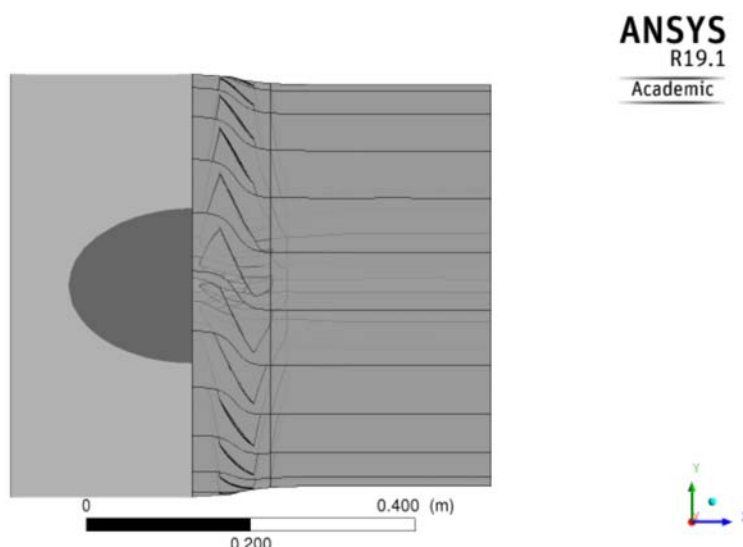


FIGURE 5.11: Full annulus simulation set-up.

TABLE 5.4: Single channel and full annulus simulation features

Simulation	Mesh Model	No. of Nodes	CPU Cost	No. of Iterations
Single channel	Coarse	900k	4 hrs	3200
Full annulus	Coarse	22 mln	14 hours	500

and 100% due to the high time required. The Figure 5.12 highlights the similarity between CFD and experimental data and the error is not so big taking in account that the number of the iteration is really low. In the end, Table 5.5, 5.6 and 5.7 report the massflow and efficiency errors compared to the experimental results.

TABLE 5.5: Single channel and full annulus simulations' comparison (Near Stall)

Simulation	\dot{m} [kg/s]	$\Delta\dot{m}$	η_{is}	$\Delta\eta_{is}$
Single Channel Fine	33.2366	-	0.905865	-
Single Channel Coarse	33.2202	+0.0164	0.903910	$1.955e - 3$
Full Annulus	33.1807	+0.0559	0.906602	$-7.37e - 4$

TABLE 5.6: Single channel and full annulus simulations' comparison (Near Peak)

Simulation	\dot{m} [kg/s]	$\Delta\dot{m}$	η_{is}	$\Delta\eta_{is}$
Single Channel Fine	33.4226	-	0.911848	-
Single Channel Coarse	33.4402	-0.0176	0.904349	$7.499e - 3$
Full Annulus	33.4088	+0.0138	0.907245	$4.603e - 3$

TABLE 5.7: Single channel and full annulus simulations' comparison (Near Choke)

Simulation	\dot{m} [kg/s]	$\Delta\dot{m}$	η_{is}	$\Delta\eta_{is}$
Single Channel Fine	34.2867	-	0.888468	-
Single Channel Coarse	34.2762	+0.0105	0.875048	+0.01342
Full Annulus	34.2976	-0.0109	0.871416	+0.013264

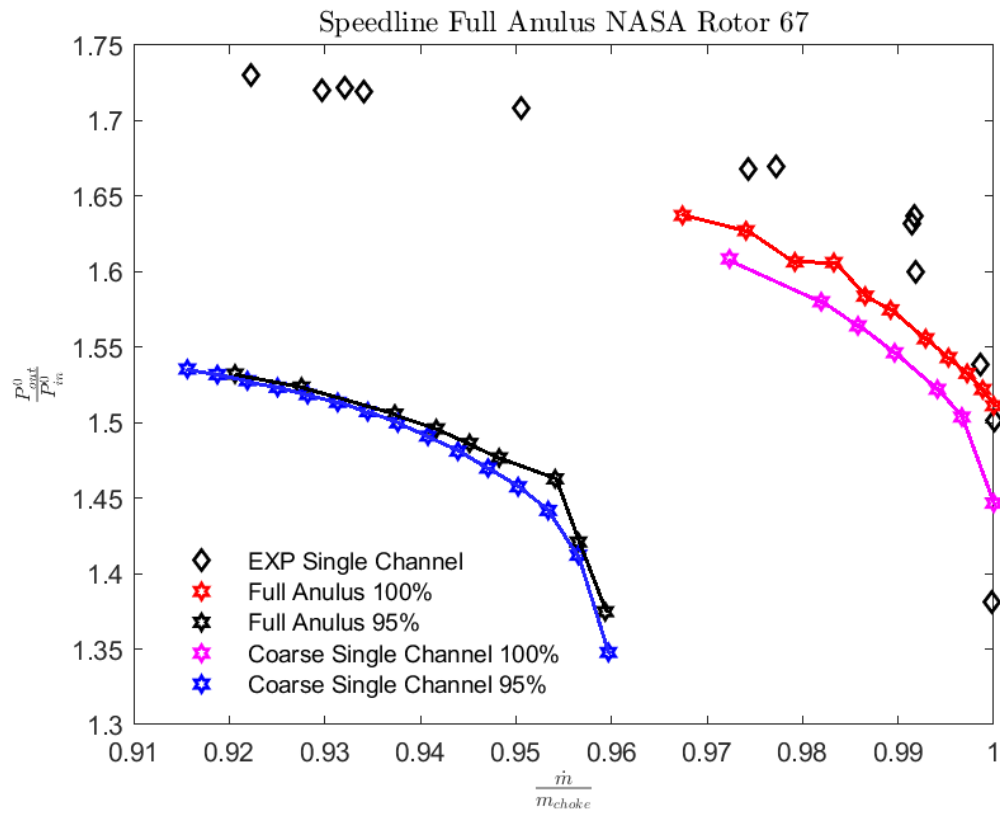


FIGURE 5.12: Comparison between full annulus simulation, single channel simulation and experimental data.

Chapter 6

Analysis of the Optimisation Results

In this chapter the results of three optimisations and the baseline will be discussed and compared. The three optimisations have different objective functions:

- The first one has the CP and the S.M.E.;
- The second one has the DC60 and the S.M.E.;
- The third one has the CP and the Swirl.

6.1 Baseline

It is important to analyse the baseline because it allows us to compare the results and verify the phenomena already described in chapter one. The Figure 6.1(a) underlines the presence of the two counter rotating vortices that occur in the lower part of the duct while Figure 6.1(b) highlights the swirl distortion. In Table 6.1 the baseline results are reported. Figure 6.1 shows how the Mach number evolve over the duct. It can be noticed that the flow tends to accelerate near the S-bend, reaching higher Mach number and generating a sonic bubble. This is due to the fact that the flow forms a strong and wide detached area.

TABLE 6.1: Baseline Results.

CP	DC60	S.M.E.
0.048042	0.48911	16531.8

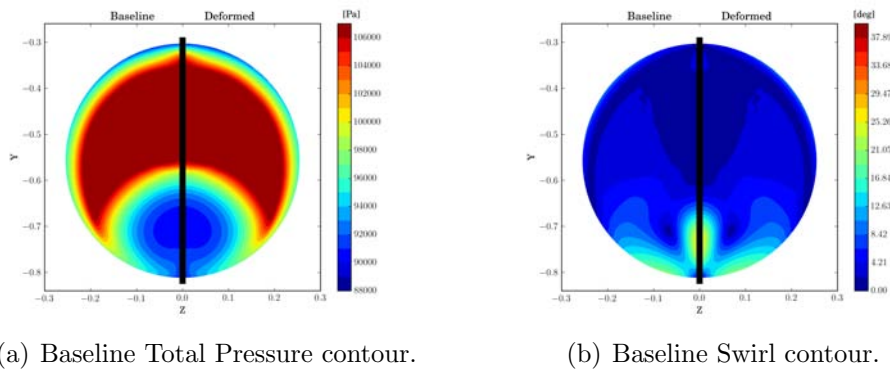


FIGURE 6.1: Baseline AIP contour.

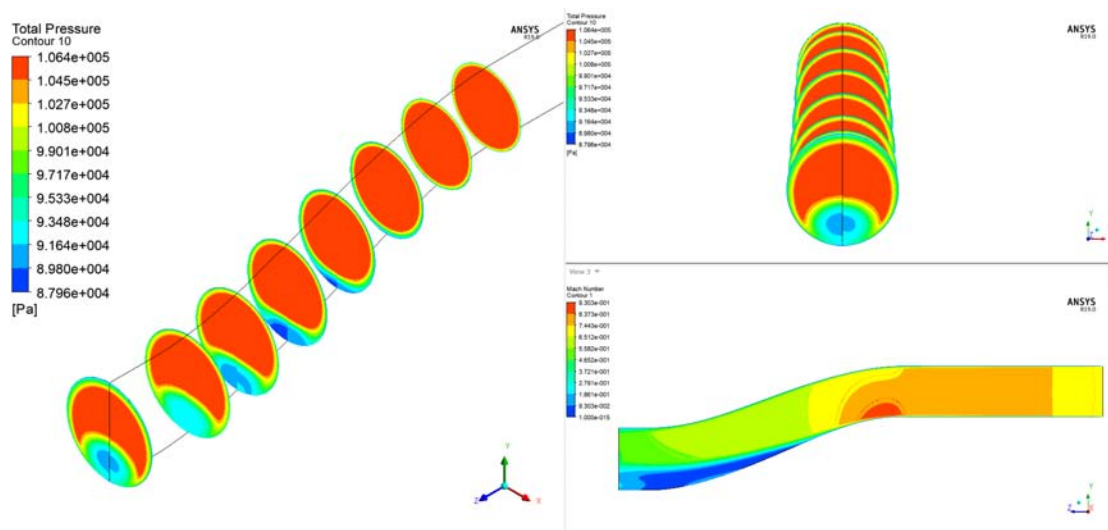


FIGURE 6.2: Baseline Total Pressure and Mach Number.

6.2 Optimisation with CP and S.M.E. Results

Using Davide's results[1] as starting point, after 250 iterations, the best results can be seen in Table 6.2. One important task that the S.M.E. function has achieved is the heavy reduction in the pressure losses. In fact, the best results found by Davide only reach a minimum of 0.043 while the new best one is 0.0397. The Figures 6.3,6.4 and 6.5 show where the position of the two vortices has move. With this three geometries the vortices are placed in the center of the duct and this leads to an high swirl component.

TABLE 6.2: CP and S.M.E. Results.

	CP	Improvement	S.M.E.	Improvement
Baseline	0.048042		16531.832	
Best CP	0.039766	+17.2%	6587.0	+60.1%
Best S.M.E.	0.043742	+8.95%	5091.6	+69.2%
Trade	0.041696	+13.2%	5961.7	+63.9%

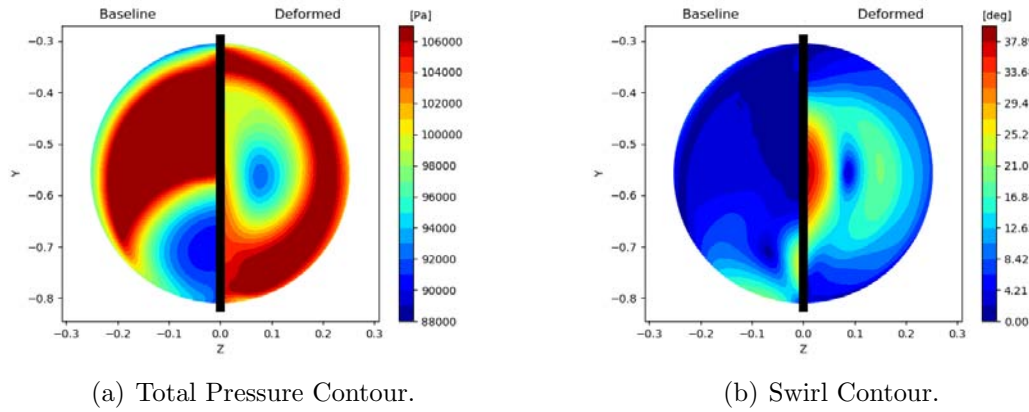


FIGURE 6.3: CP Best AIP Contour.

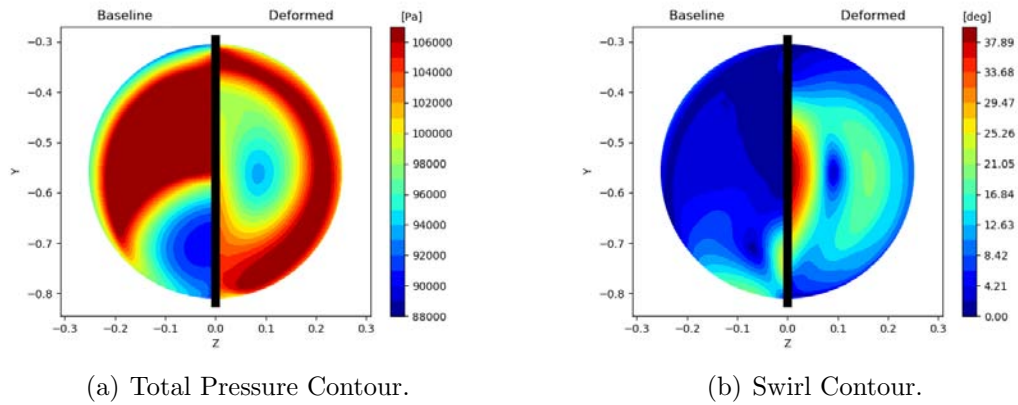


FIGURE 6.4: S.M.E. Best AIP Contour.

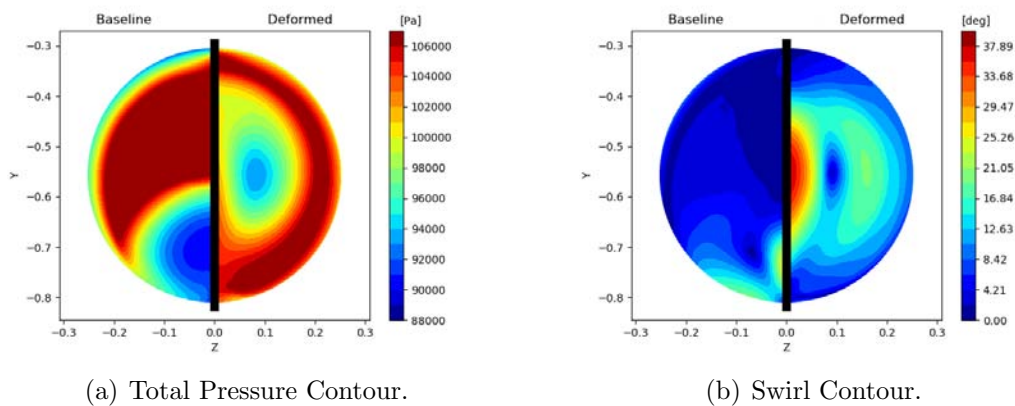


FIGURE 6.5: Trade AIP Contour.

To better understand how the flow behave in this three S-ducts it is important to analyse the cross-section shape and the Mach number. Figure 6.8, 6.9 and 6.10 show the different shape of the S-duct. The first thing that is important to notice is the Mach number. The difference with the baseline is massive. In fact there is no more the formation of the sonic bubble but instead the flow decelerate reaching an average of 0.45 Mach number in front of the ogiva. The deceleration of the flow is caused by the big increase of area of the cross section. All three geometries have the first five cross section that continue to rapidly increase the area and changing the shape, with the widest having a shape really close to an oval. Then the cross section slowly decreases the area to match the ogiva inlet area. Another important difference is the curvature of the S-duct. In Figure 6.6 the white curve represents the baseline, the blue one the best CP, the green one the best S.M.E. and the red one the trade off. It can be noticed that all three bottom line have an increase curvature, especially the blue one; while also the top line follows almost the same behaviour of the baseline.

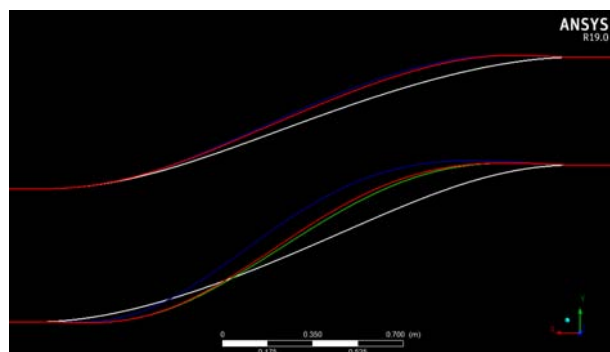


FIGURE 6.6: Baseline and Results S-bends.

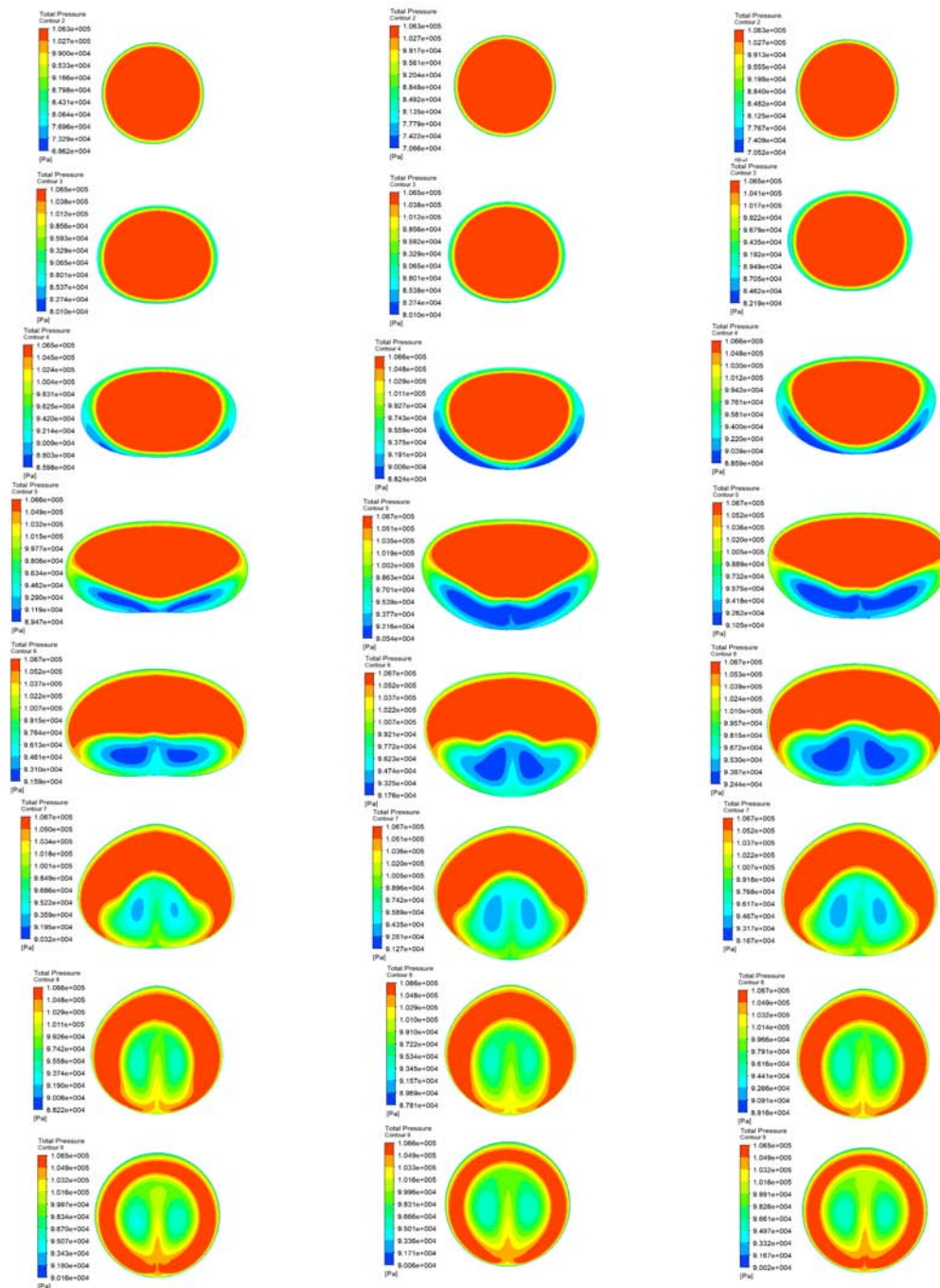


FIGURE 6.7: Cross-Section CP Best(Left) S.M.E. Best(Mid) Trade Off (Right).

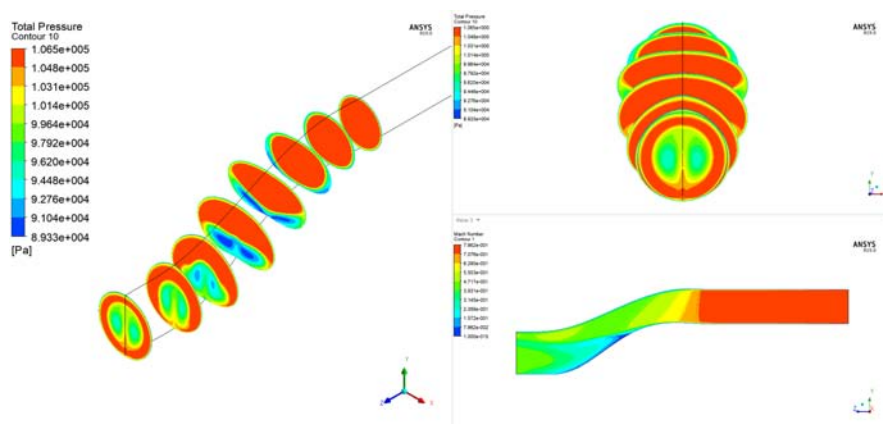


FIGURE 6.8: CP Best Total Pressure and Mach Number.

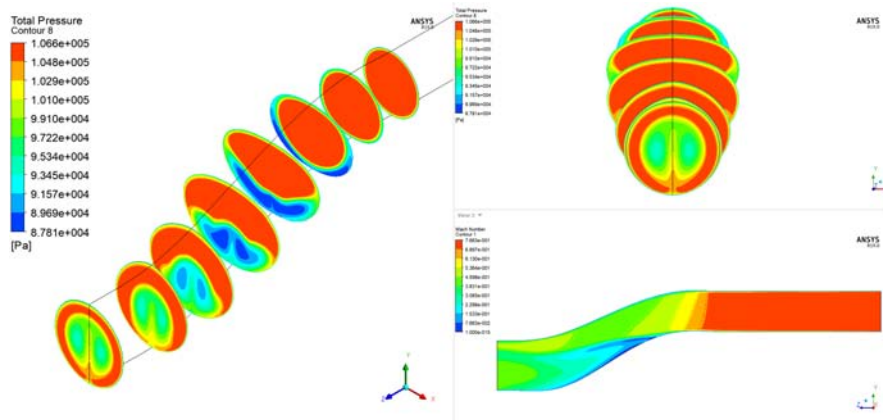


FIGURE 6.9: S.M.E. Best Total Pressure and Mach Number.

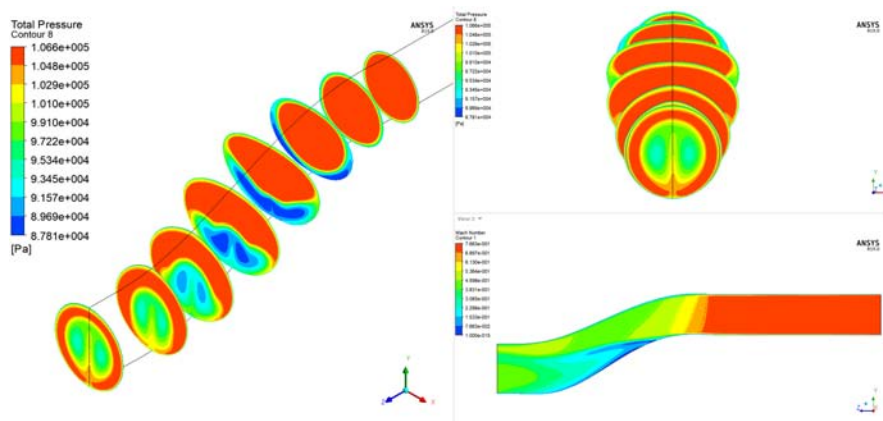


FIGURE 6.10: Trade Total Pressure and Mach Number.

6.3 Optimisation with DC60 and S.M.E. Results

Using Davide's results[1] as starting point, after 300 iterations, the best results can be seen in Table 6.3. Also in this optimisation the two vortices have move to the center part but compared to the previous optimisation the swirl component has slightly decrease. The curvature of the three duct compared to the baseline is pretty different. The bottom line of the DC60 is over the baseline while the other two are under.

TABLE 6.3: DC60 and S.M.E. Results.

	DC60	Improvement	S.M.E.	Improvement
Baseline	0.48911		16531.8	
Best DC60	0.00017	99.96%	8878.4	46.3%
Best S.M.E.	0.042068	91.4%	4744.1	71.3%
Trade	0.029569	93.95%	6107.8	63.1%

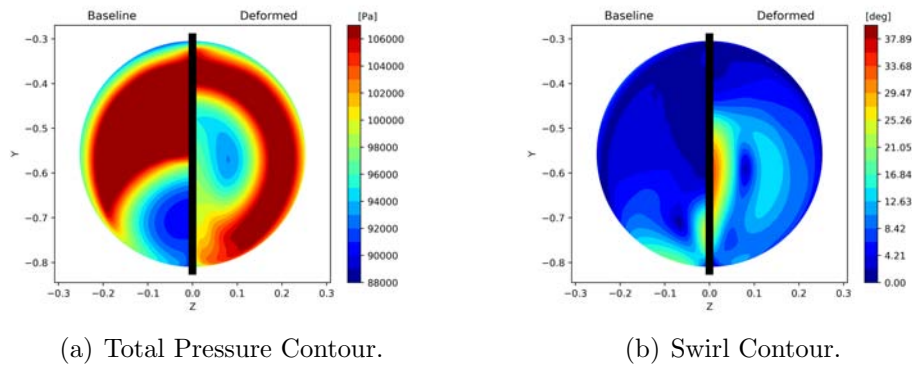


FIGURE 6.11: DC60 Best AIP Contour.

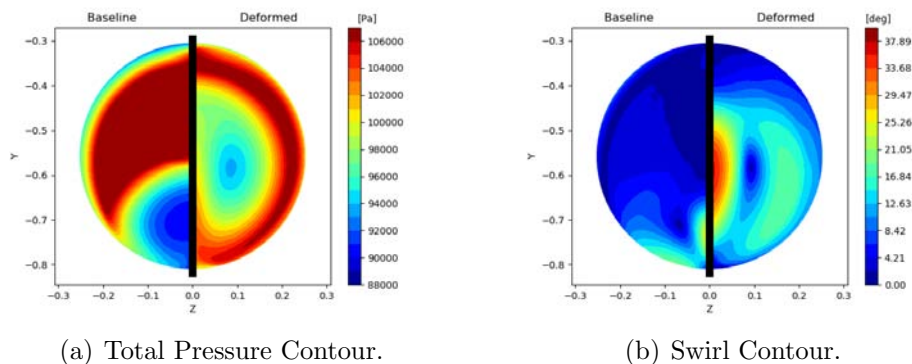


FIGURE 6.12: S.M.E. Best AIP Contour.

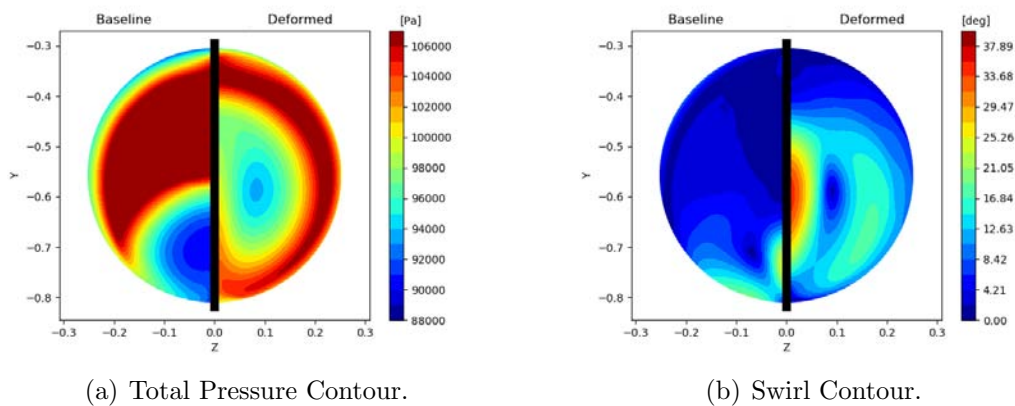


FIGURE 6.13: Trade AIP Contour.

To better understand how the flow behaves in this three S-ducts it is important to analyse the cross-section shape and the Mach number. Figure 6.16, 6.17 and 6.18 show the different shape of the S-duct. Also in this optimisation, the sonic bubble has dissapear due to the increase of the cross section area. The main difference with the previous optimisation is that the DC60 grown in area is reduced, so the cross sections are less large and more circular. Moreover, the last three cross section have radically changed, transforming into a rounded triangular shape. This shape is really particular and his contribution to the flow is really important. In fact a triangular shape bound and restrict the flow. The three wall configuration tend to compress and uniform the flow reducing a lot the swirl component in the middle part. In fact the core of the flow (in red) when is about to be cut by the detach flow (in blue) find a decrease in cross section and almost flat wall on both side. This leads to change the trajectory of the core that is compressed an guided by the wall itself. The Best S.M.E. has also a big oval cross section and near the ogive it has also a rounded triangle shape. The trade off instead has an almost square cross section.

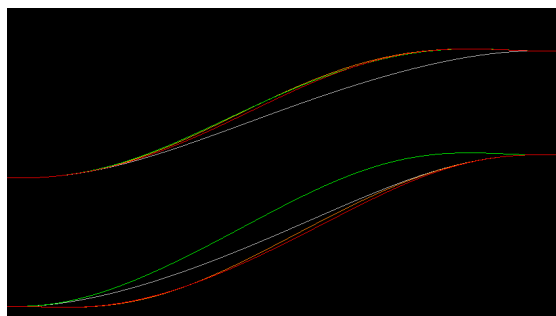


FIGURE 6.14: Baseline and Results S-bends.

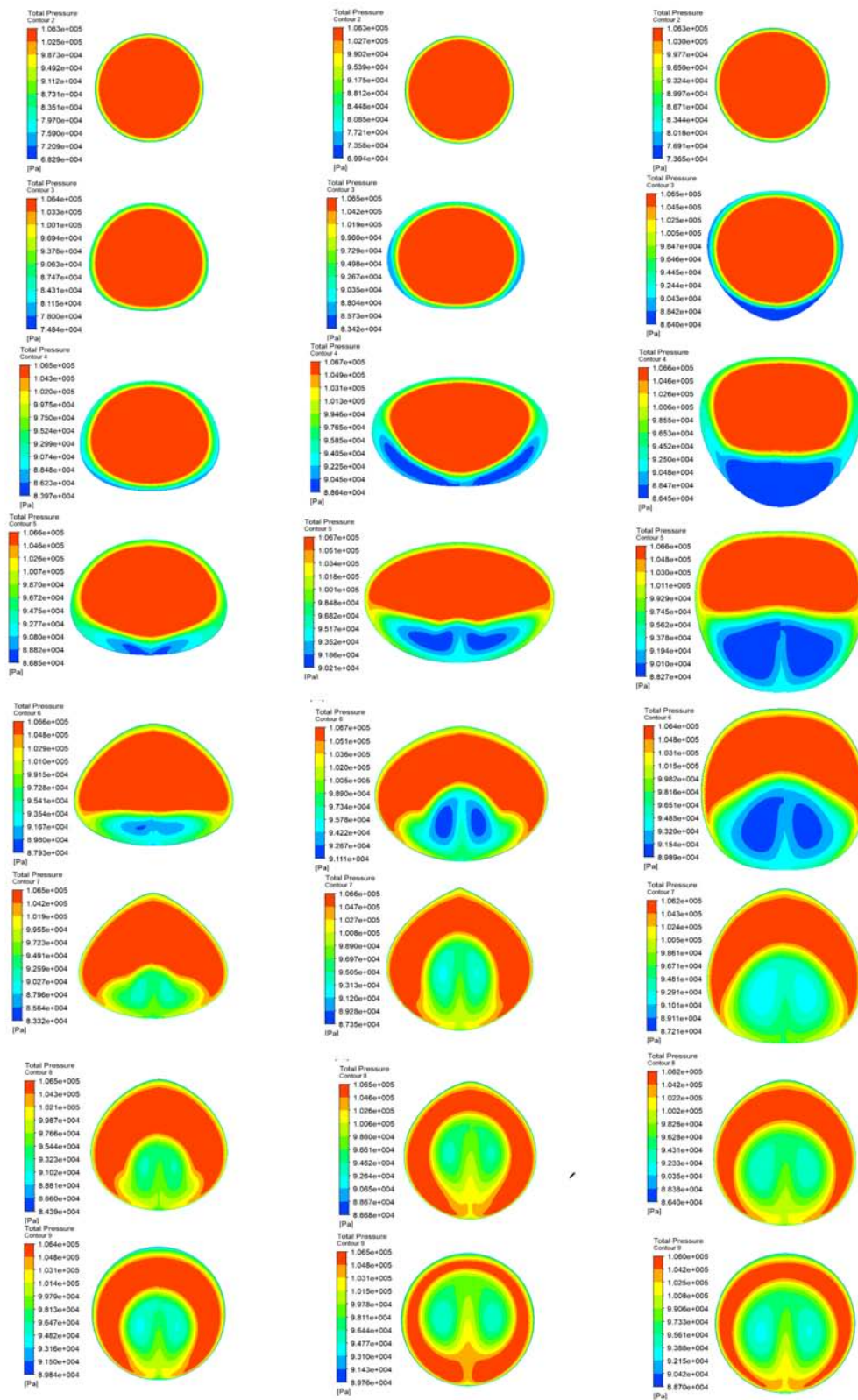


FIGURE 6.15: Cross-Section DC Best(Left) S.M.E. Best(Mid) Trade Off (Right).

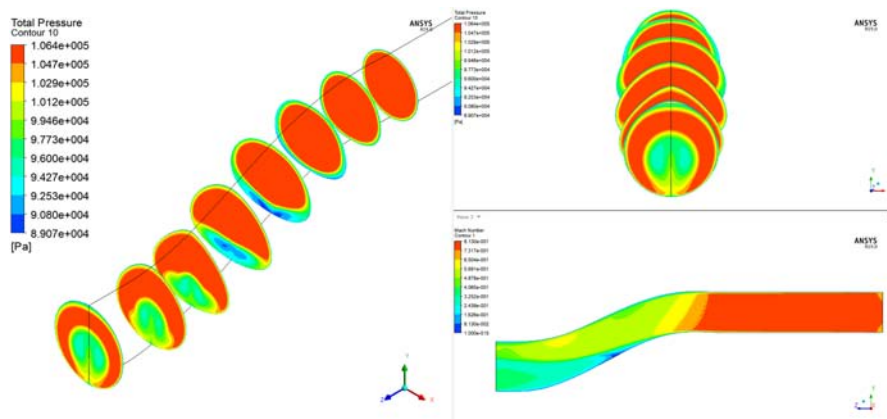


FIGURE 6.16: DC Best Total Pressure and Mach Number.

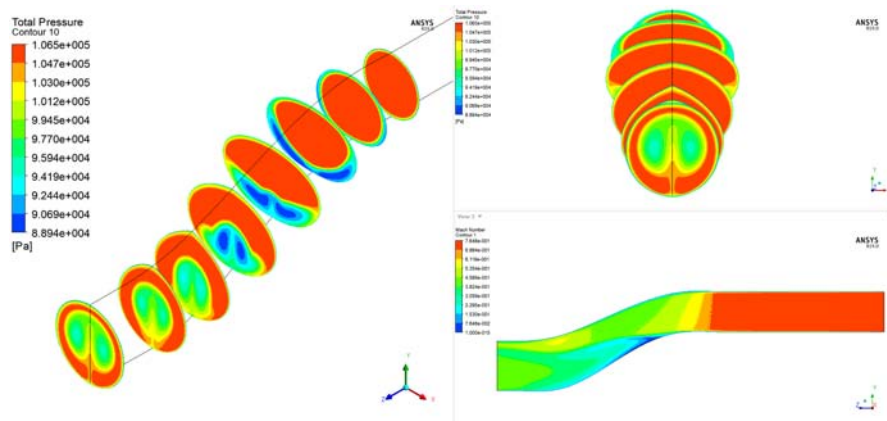


FIGURE 6.17: S.M.E. Best Total Pressure and Mach Number.

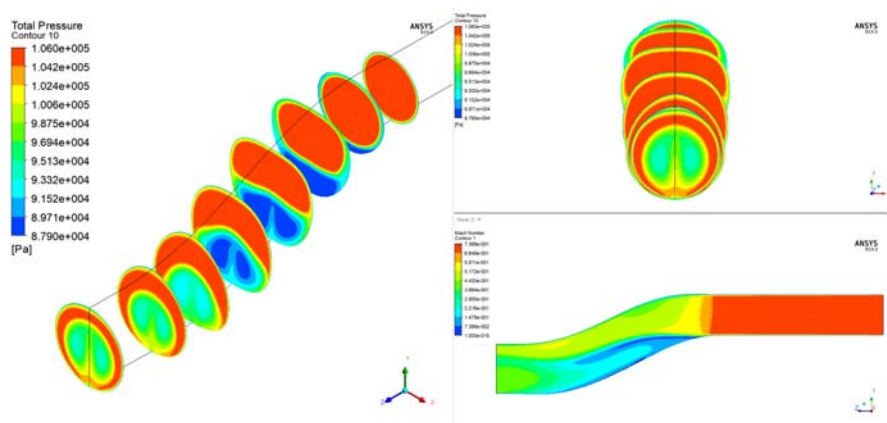


FIGURE 6.18: Trade Total Pressure and Mach Number.

6.4 Optimisation with CP and Swirl Results

This optimisation was carried out by Davide [1] and here it will be reported the results due to the will to study the interaction with the rotor 67. This optimisation is really interesting because, instead of having two counter rotating vortices on the AIP, four vortices are generated. Only two geometries will be analysed because the best CP geometry simulation is very unstable and no results have been possible to produce.

TABLE 6.4: CP and Swirl Results.

	CP	Improvement	Swirl	Improvement
Baseline	0.04804		4.73329	
Best Swirl	0.04829	-0.5%	2.51120	+46.9%
Trade Off	0.04707	+2.0%	2.58174	+45.5%

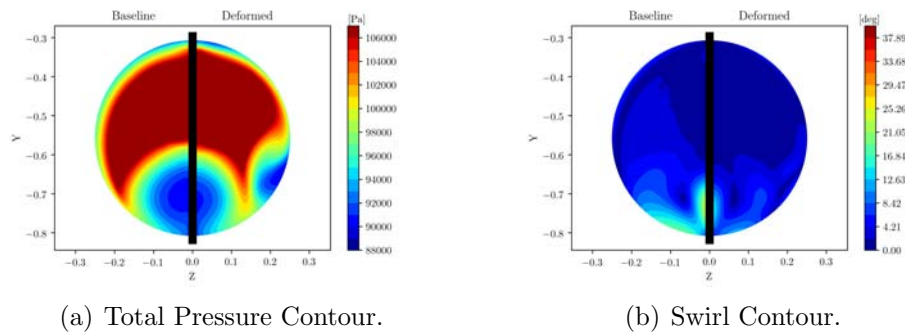


FIGURE 6.19: Swirl Best AIP Contour.

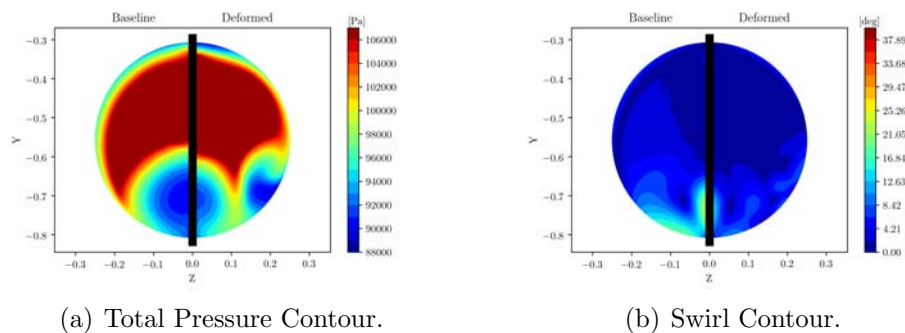


FIGURE 6.20: Trade Off AIP Contour.

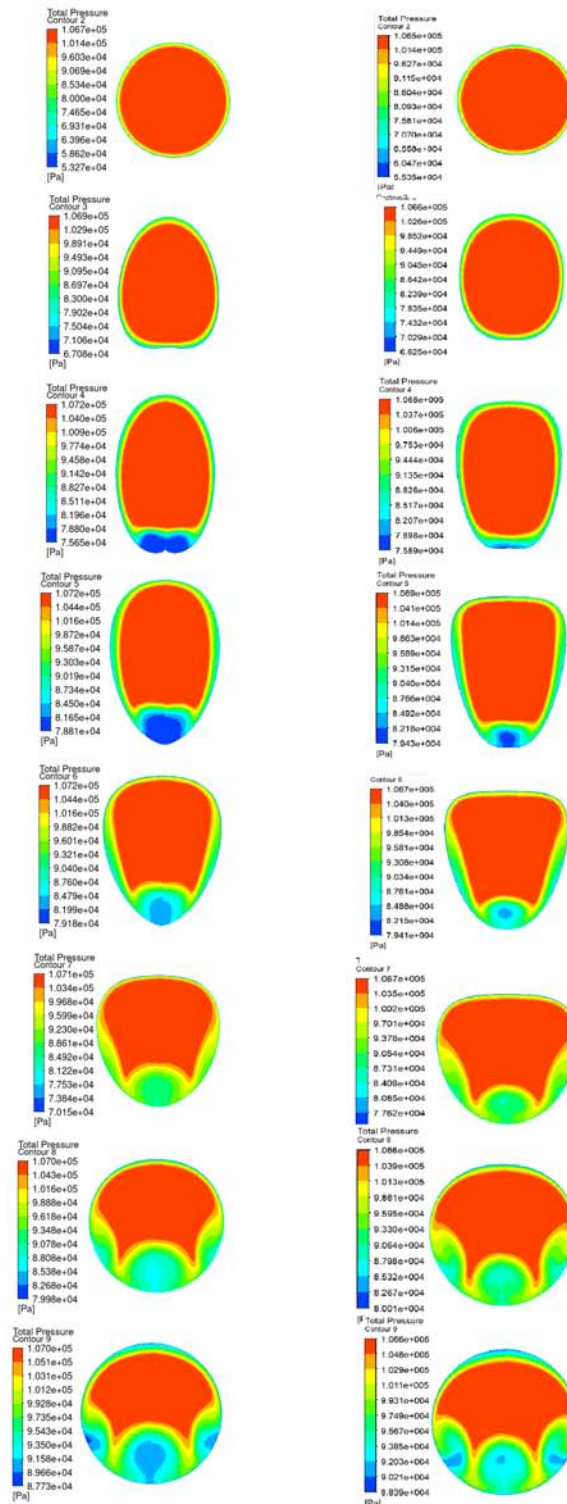


FIGURE 6.21: Cross-Section SW Best(Left) Trade Off (Right).

The cross section view shows how the geometry of the s-ducts has changed. The best swirl solution have the first three cross section that evolve into an almost vertical oval but then on the fifth and sixth cross section it becomes more triangular and in the end the last two section return circular to match the ogive. The trade off solution instead of having an oval shape on the fourth section, it has already a triangular section that in section five and six become more and more rounded. The problem with this inverted triangle cross section is that the flow form a sonic bubble right before the s-bend due to the wide detached flow area.

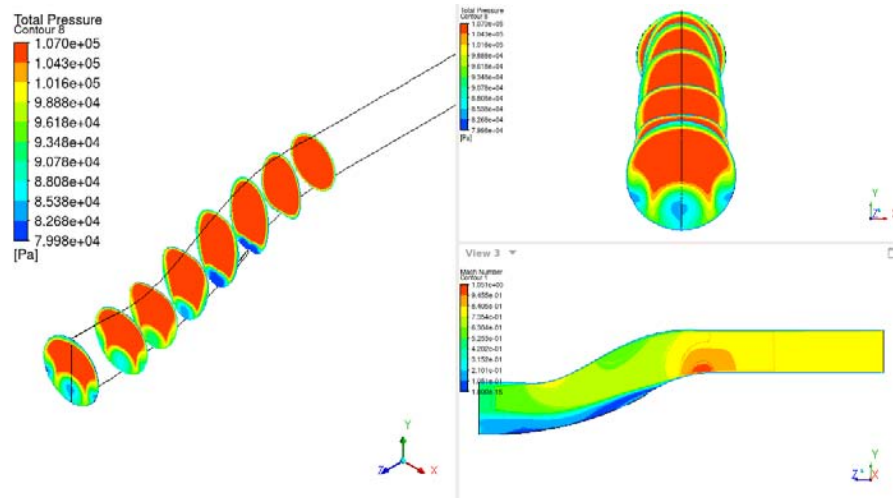


FIGURE 6.22: Swirl Best Total Pressure and Mach Number.

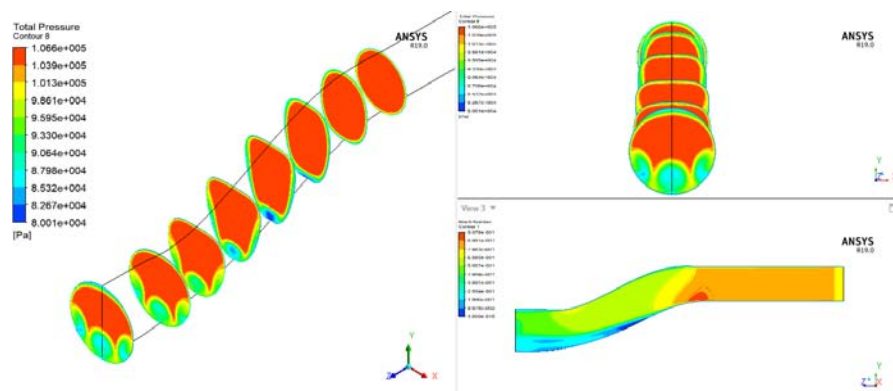


FIGURE 6.23: Trade Off Total Pressure and Mach Number.

Chapter 7

S-duct and R67 Interaction

From this chapter the simulations of the different s-ducts and the rotor 67 are carried out. The main purpose of this thesis is to understand how the s-duct deteriorate the transonic fan performance. As already described in chapter six, the s-duct creates inlet distortions and many studies have been done to replicate these inlet distortions. In literature total pressure and swirl distortion are analysed separately but in reality the two distortions coexist together and the main problem of the automatic generation of inlet distortions is to recreate the two distortions combined. On the other hand, in this thesis a full cfd simulation is conducted. Since the distortions involves swirl and total pressure a single blade simulation does not describe the full phenomenon but instead a full annulus simulation is required.

7.1 S-duct and R67 Simulation Set-Up

The entire simulation was carried out on CFX, by exploiting the cluster of Cranfield University. The parameters of the simulation are:

- No. of Nodes 23e+6
- No. of Domain 4
- No. of Iteration 1500
- No. of CPU 16 Core

- Computational Cost 2 days

Since the high computational cost and in accordance with the previous work done by Marco [15] it was decided to simulate just one speed line and in particular the 95% of the rotational speed. A big difference between this thesis and the previous studies conducted by Marco [15] is that the s-duct is connected with the ogiva at the AIP surface. So the mesh created from the optimisation was cutted at the AIP using ICEM CFD and then connected with the frozen rotor interface to the ogiva. This allows us to compare the results analysed in the optimisation with the rotor performance. In fact, if the final portion of the s-duct is not removed the flow has enough space to dissipate the vortices and the distortions become less and less.

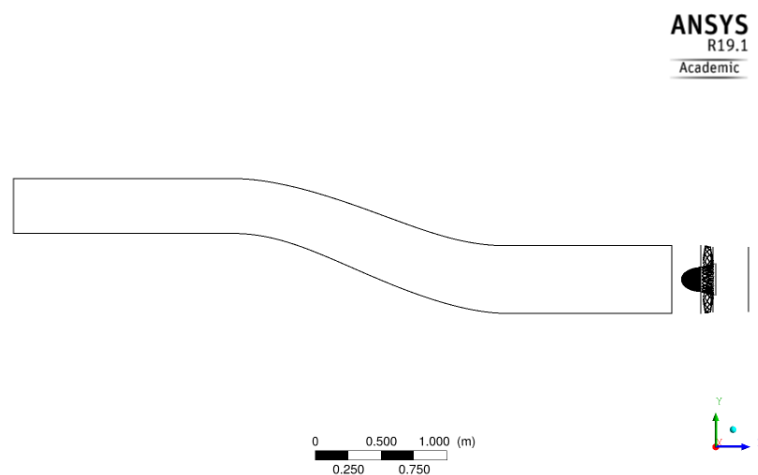


FIGURE 7.1: Marco's Configuration.

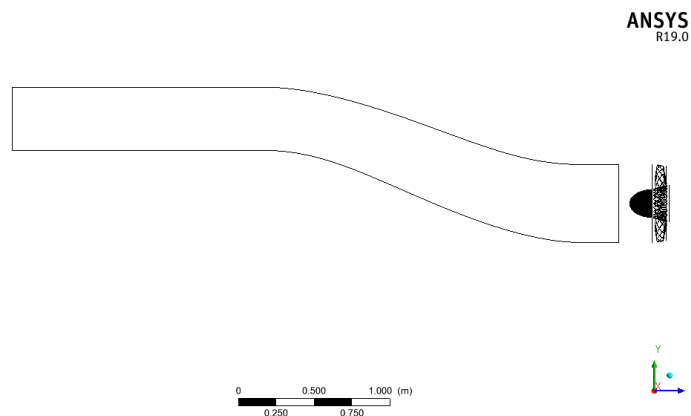


FIGURE 7.2: New Configuration.

As inlet condition, a total pressure boundary condition is set at 106300 [Pa] while the outlet static pressure varies every simulation due to the will to study the compressor map. Since many simulations have been done, to describe the interaction between each s-duct and the rotor 67 only the condition near the peak efficiency will be analysed.

7.2 Baseline and R67 interaction

Figure 7.3 shows the different performance between the ogiva and rotor 67 with the clean inlet flow and with the baseline. Since the total pressure at the inlet of the ogive is different for the two simulations in the x axis it is used the corrected mass flow rate with 101325 [Pa] as pressure reference and 288.2 [K] as temperature reference. The two graphs show that the s-duct drastically decrease the performance of the rotor 67. Moreover the mass flow rate has considerably decreased because the inlet area of the s-duct is smaller than the area of the fan. In fact, all the s-ducts that are analysed in this chapter are diffusive ducts. To better understand why there is a huge reduction in term of efficiency and pressure ratio it is important to analyse how the flow interact with the three domain: s-duct,ogive and fan.

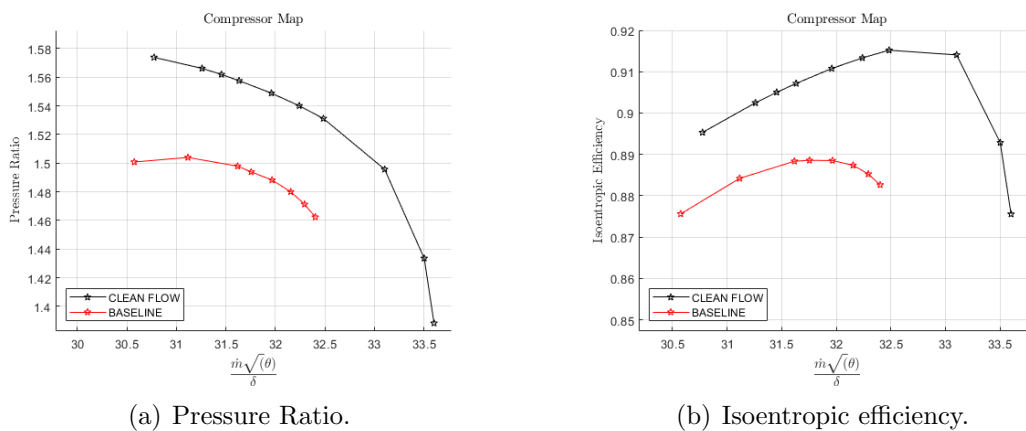


FIGURE 7.3: Compressor Map for the Clean Flow and the Baseline.

TABLE 7.1: Clean and Distorted Flow.

Model	\dot{m} [kg/s]	Error	η_{is}	$\Delta\eta_{is}$
Near Peak Clean	32.48		0.915197	
Near Peak Distorted	31.76	-2.25%	0.888567	-2.91%

7.2.1 S-duct Baseline

As already described in Chapter 6 and as Figure 7.4 shows, the baseline creates two counter rotating vortices in the low area of the duct leading to a formation of a low total pressure region. This leads to an high swirl component at the inlet of the ogive.

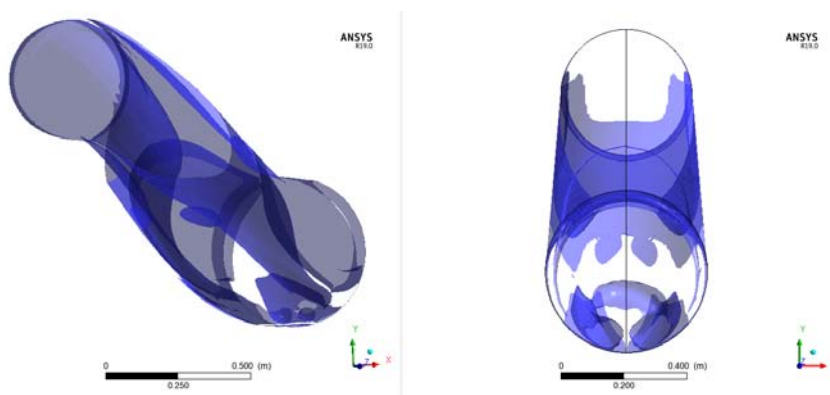


FIGURE 7.4: Vorticity of the S-duct Baseline.

7.2.2 Ogive Interaction with S-duct Baseline

After the formation of the two counter rotating vortices, the flow, when encounters the ogive domain, is affected by the rotor velocity. In Figure 7.5, it is important to remember that: the fan and the ogive are rotating in the counterclockwise direction, the vortex on the bottom left is rotating in the counterclockwise direction while the other one in the bottom right is rotating in the clockwise direction. Referring to Figure 7.5 it is clear how the vortices are affected by the fan. The counterclockwise vortex is push by the rotational speed of the fan, since both are rotating in the same direction, and merge with the clockwise vortex giving birth to a single strong vortex in the bottom right region. It is also important to notice how the absolute velocity field has changed in Figure 7.7. This new field is created because, when the flow positioned in the central part of the duct touch the ogive,

it starts to slip, but due to the position of the vortex, the right side attract more mass flow than the left side. So the flow tends to converge to right side of the ogive and increase his speed. Since the flow tends to travel the shortest distance to reach the vortex, the shortest way is the right side instead of the left side. The outlet velocity contour is dominated with high speed on the right side while the left lower side has lower speed.

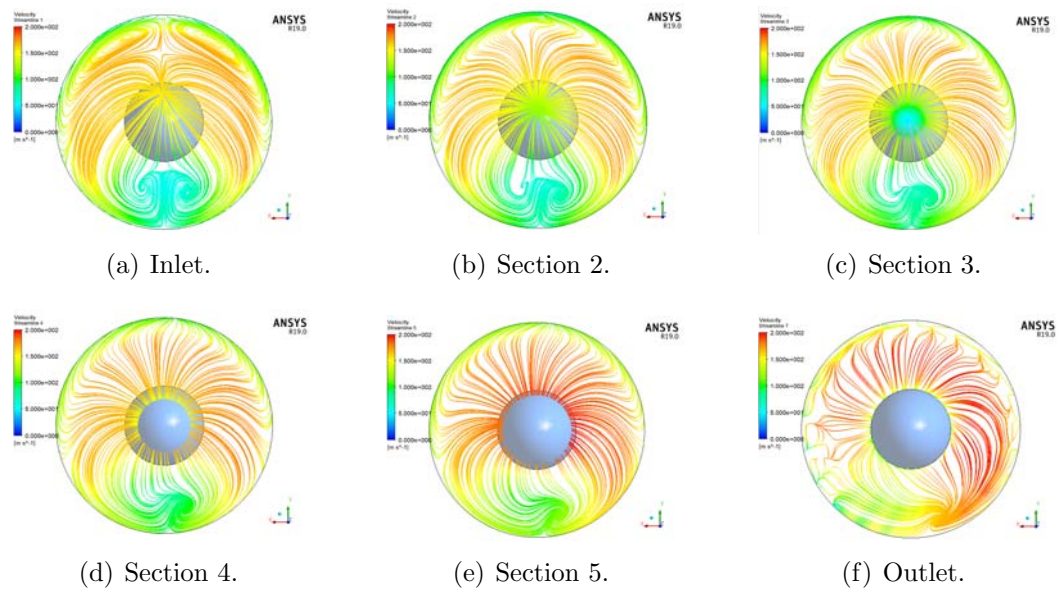


FIGURE 7.5: Velocity Streamline.

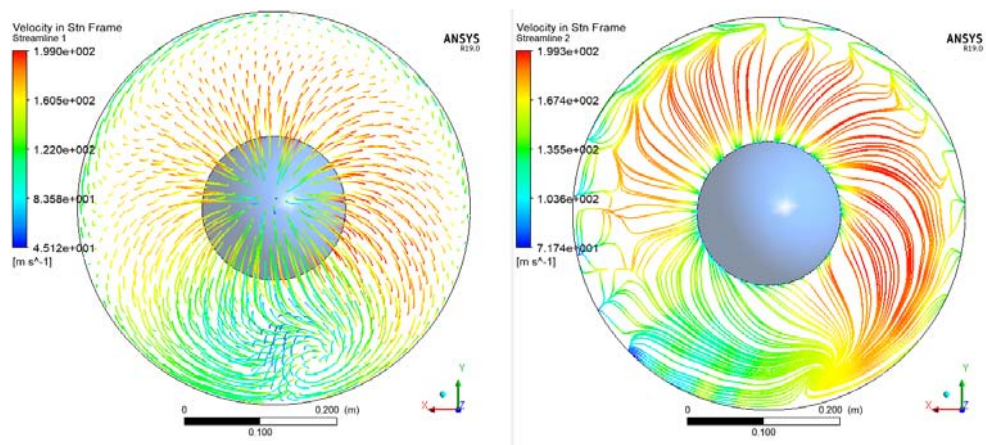


FIGURE 7.6: Velocity Streamline through the Ogive (Left) and at the Outlet (Right).

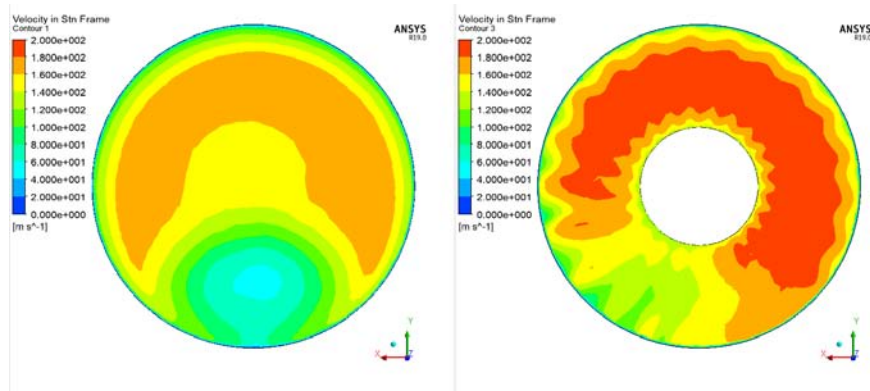


FIGURE 7.7: Inlet Velocity Contour (Left) and Outlet Velocity Contour (Right).

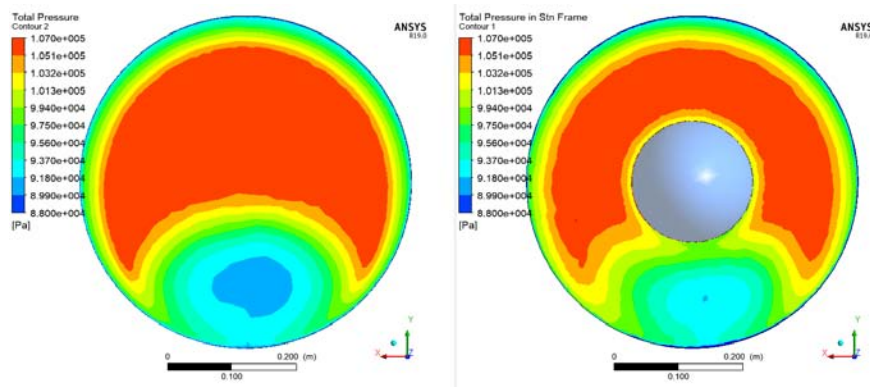


FIGURE 7.8: Total Pressure Contour at the Inlet (Left) and Outlet (Right) of the Ogive.

7.2.3 R67 Interaction with S-duct Baseline

To better understand how the inlet conditions affect the fan performance, it is important to compare the clean inlet flow condition near peak efficiency with the conditions created by the s-duct. First of all, Figure 7.10 and Figure 7.11 allow to compare the inlet Mach number for the clean and the distorted flow. Using Figure 7.6, the Mach number contour becomes clearer. Remembering that the fan is rotating in the counterclockwise direction, the flow in the lower left part also is rotating in that direction and so the relative Mach number is smaller. Instead in the lower right part the flow is rotating in the clockwise direction and so the relative Mach number is higher. The absolute Mach number has also two regions and it was described in the previous section. To better understand where theta starts and to introduce a blade numeration Figure 7.9 is used as reference.

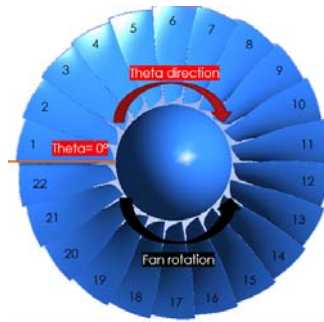


FIGURE 7.9: Theta Reference and Blade Number.

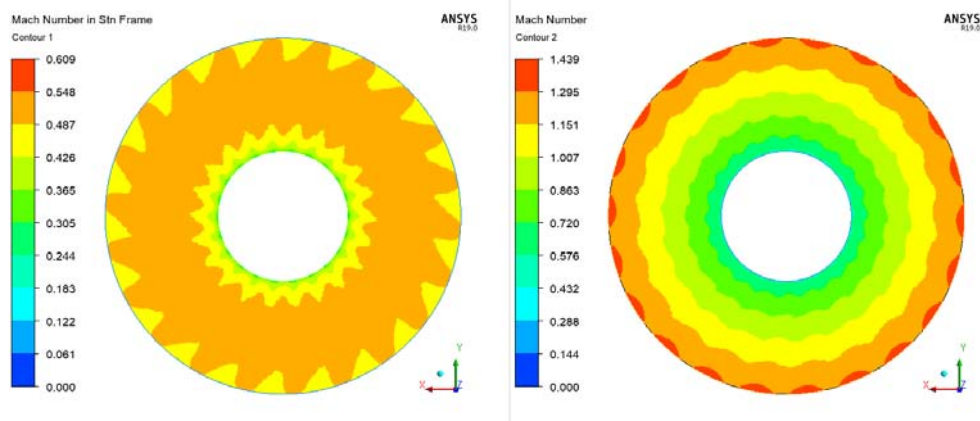


FIGURE 7.10: Inlet Mach Number Clean Conditions.

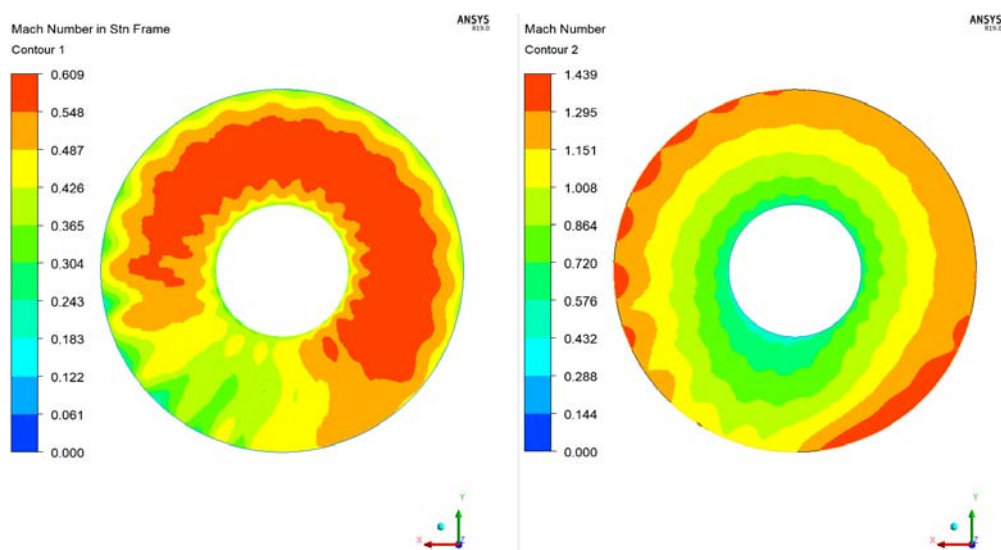


FIGURE 7.11: Inlet Mach Number Baseline.

After the analysis of the relative and absolute Mach, Figure 7.12 and Figure 7.13 show the different component of the absolute and relative velocities. To better understand these contours, Figure 7.14 and Figure 7.15, taken from ANSYS CFD-POST Guide, will be used as reference. The velocity streamwise and the velocity

blade to blade in standard frame are similar to the absolute Mach number due to the low circumferential velocity. The circumferential velocity (positive in theta direction) assumes positive value in the right side and in the top left side, and negative value in the bottom left side. The spanwise velocity assumes positive value near the hub, with the zone near the vortex having the highest values and zero or negative value near the tip. The absolute flow angle for the right side and the top left side is close to 90° while in the bottom left side the flow angle is more than 90° . This means that the absolute velocity changes quadrant on the blade to blade plane. In the end the relative blade to blade velocity and the relative circumferential velocity have the same trend of the relative Mach number and it can be related to the vortex position. Figure 7.16 gives a nice view of

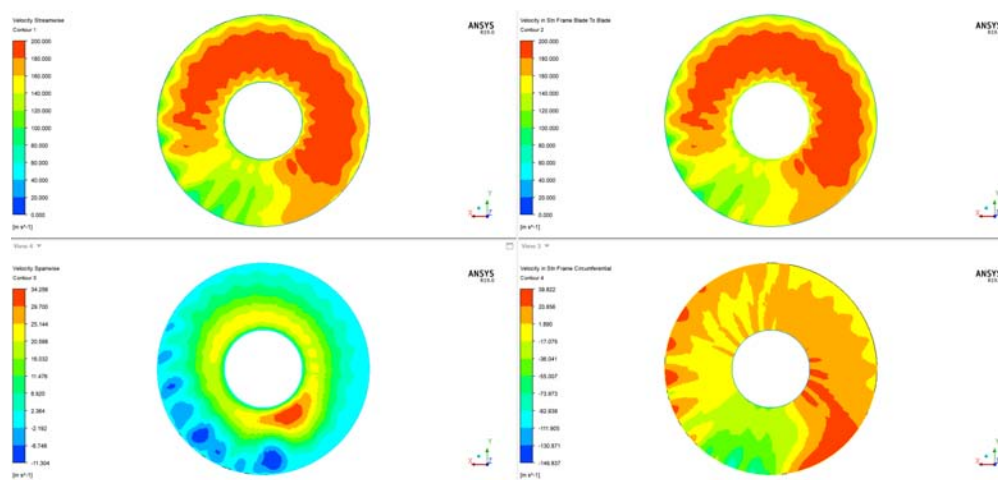


FIGURE 7.12: Streamwise(Top Left),Blade to Blade Abs (Top Right), Spanwise(Bot Left), Crf Abs(Bot Right).

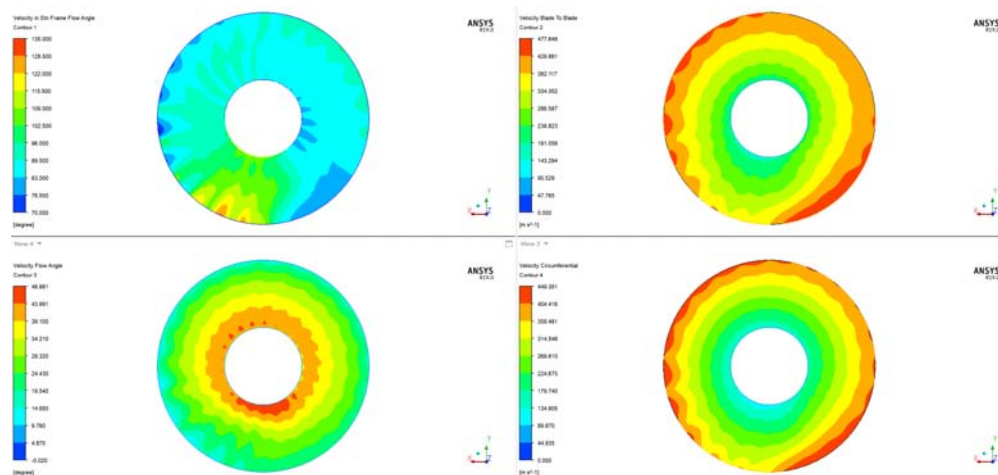


FIGURE 7.13: Flow Angle Abs(Top Left),Blade to Blade Rel(Top Right), Flow Angle Rel(Bot Left), Crf Rel(Bot Right).

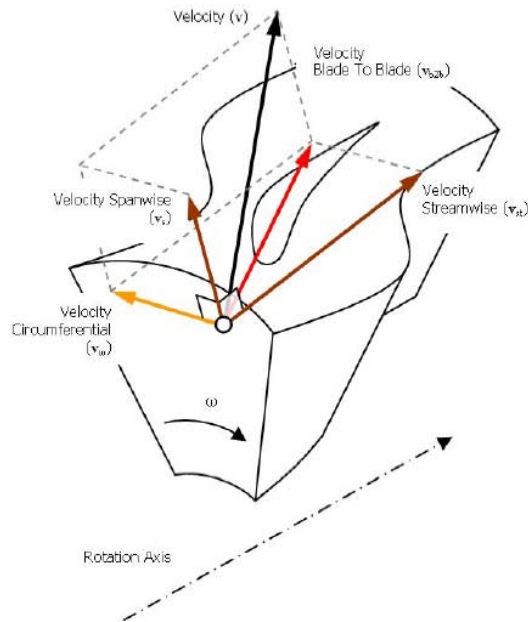


FIGURE 7.14: Velocity Components

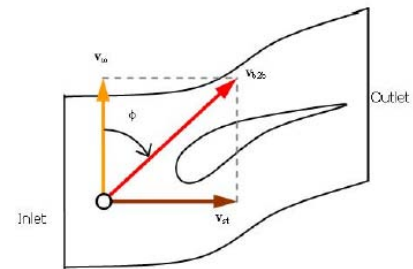


FIGURE 7.15: Velocity Components in Blade-To-Blade Plane

the position of this shocks for three different span: 0.2, 0.5 and 0.8 and highlight how the distorted flow affect the shock position. In particular referring to Figure 8.13(c) and remembering that blade number 1 is at the top, and the fan is rotating in the direction bottom to top, blade number from 3 to 16 experience a choking condition where the shock is highly oblique due to the high inlet Mach number; blade number 1, 2, 21 and 22 experience a normal shock and blade number from 17 to 20, due to the low inlet relative velocity almost under the speed of sound, create just a sonic bubble. This velocity observation can be extend to the other two figures 8.13(b) and 8.13(a). In fact, the fan can be divided into three regions: The first one is from blade number 3 to 16 where the inlet Mach number is higher than the clean flow condition. The second one is from blade number 21 to 2 where the inlet Mach number is close to the peak efficiency. The last one is from blade 17 to 20 where the inlet Mach number is lower than the clean flow condition and the blade can't generate a schok. To resume, the s-duct creates two counter-rotating vortex that merge together due to the rotational speed of the fan. The single vortex generated affects the relative and absolute velocity field that moves the position of the shock wave inside or outside the blade or creates just a sonic bubble.

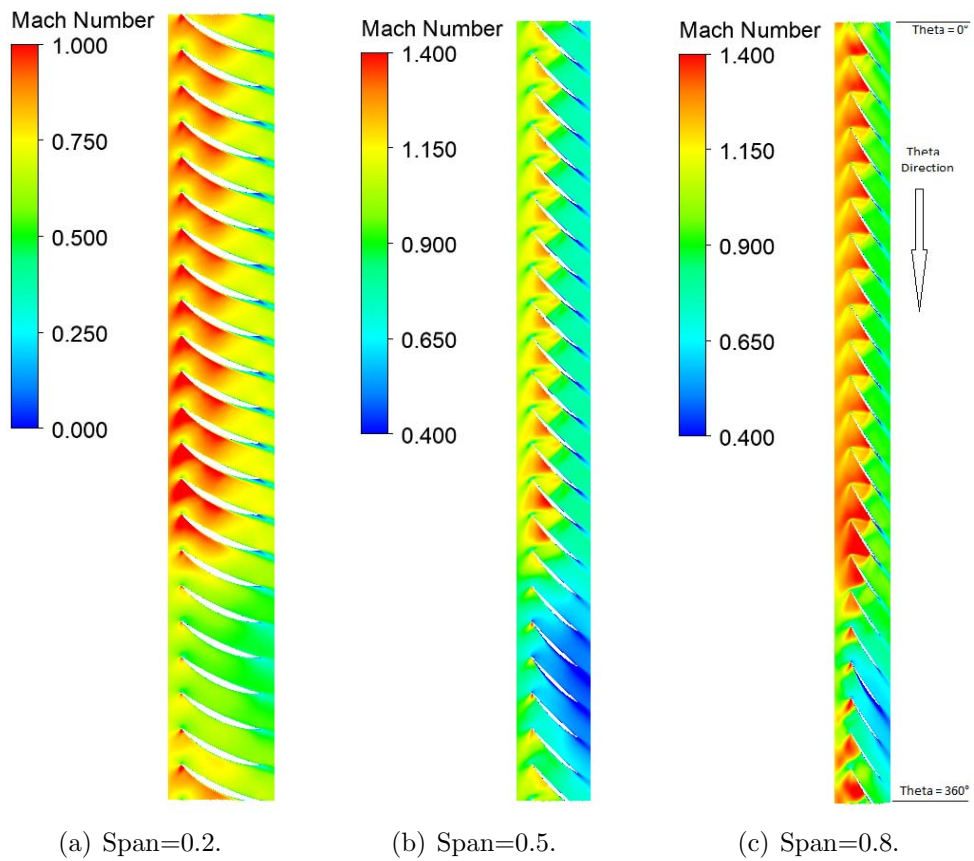


FIGURE 7.16: Blade to Blade Contour.

Chapter 8

S-duct Optimisation and R67 Interaction

8.1 CP/S.M.E. optimisation and R67 interaction

Figure 8.1 shows the different performance between the baseline and the optimisation results. The graphs show that the new s-ducts obtained by the optimisation give better inlet conditions to the fan allowing it to work more efficiently. In fact, in Table 8.1 the performance of each s-duct near the peak condition are reported. The best results reach +0.834464% over the polytropic efficiency of the baseline. To understand why these s-ducts have better performance it is important to understand how the flow has changed compared to the baseline.

TABLE 8.1: Baseline and Optimisation Performance Near Peak.

Model	\dot{m} [kg/s]	η_{is}	$\Delta\eta_{is}$	η_{pol}	$\Delta\eta_{pol}$
Baseline	31.76	0.888567		0.894706	
Best CP	31.40	0.896349	+0.88%	0.902172	+0.83%
Best S.M.E.	31.32	0.895800	+0.81%	0.901689	+0.78%
Trade Off	31.27	0.895013	+0.73%	0.900959	+0.70%

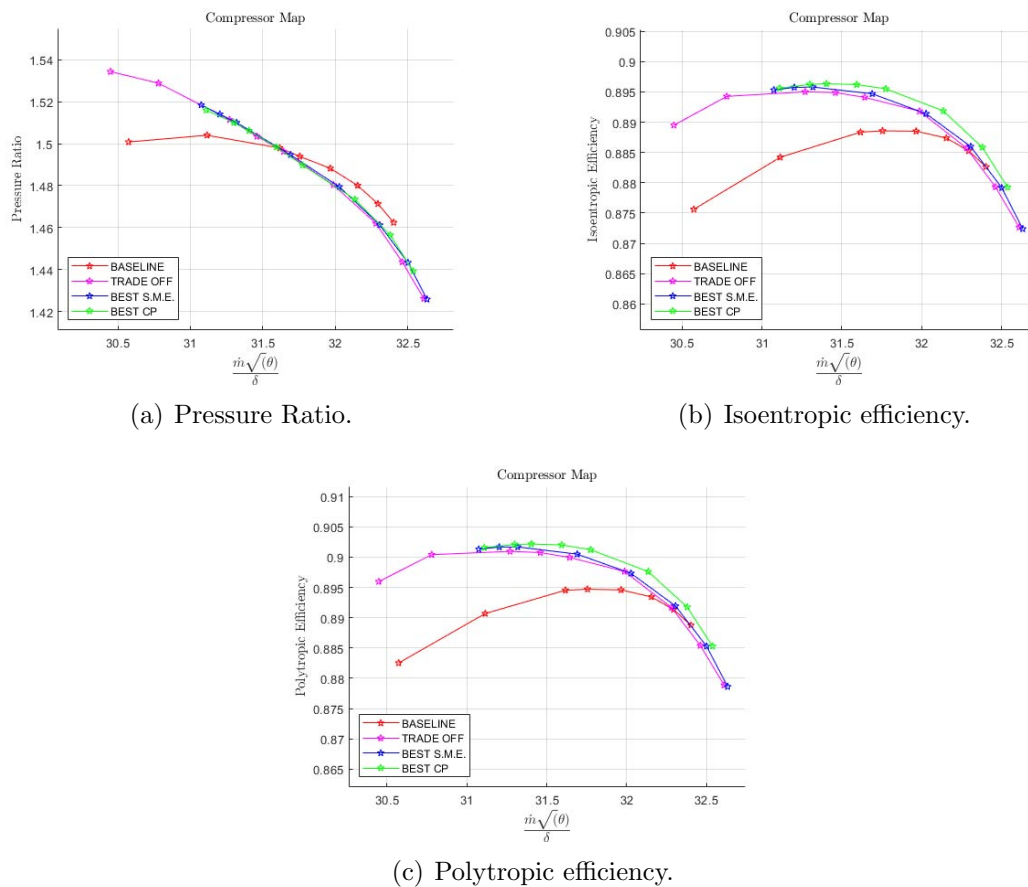


FIGURE 8.1: Compressor Map Comparison Between Baseline and Optimisation Results.

8.1.1 S-duct Best CP

As already described in Chapter 6, the CP best geometry creates two counter-rotating vortices placed on the middle part of the duct. Figure 8.2 shows the vortices structure inside the duct.

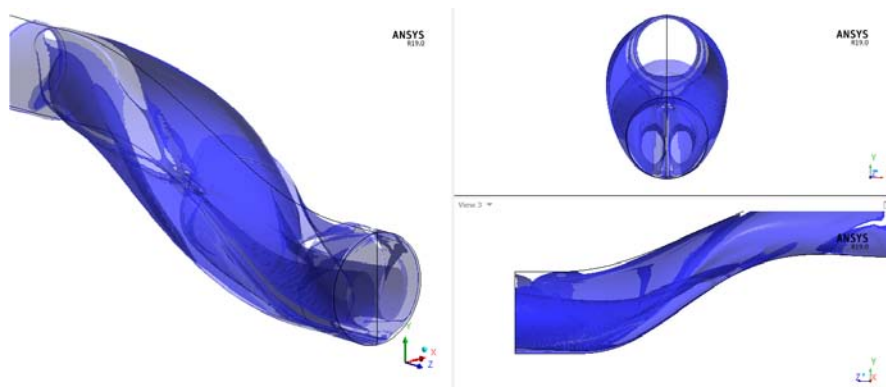


FIGURE 8.2: Vorticity of the S-duct Best CP.

8.1.2 Ogive Interaction with S-duct CP Best

After the formation of the two counter rotating vortices, the flow, when encounter the ogive domain, is affected by the rotor velocity. Figure 8.3 shows that the vortices structure evolve in the ogive. When the two counter rotating vortices reach the ogive, since their core is placed slightly under the center of the ogive, they start to move downward. After this movement the two vortices follow the same phenomena that occur in the baseline simulation. In fact the two vortices start to merge and in the end a single vortex is created on the bottom of the ogive. The main difference with the baseline is that now the core of the vortex is placed almost in the bottom center. Another important difference is the distance between the two core vortices. The more distant they are, the less influence the right vortex will have. In the end it has to be analyse how the velocity field has evolved. As Figure 8.5 shows, the velocity field is more homogeneous and has less distorsion. This is due to the fact that when the flow touch the ogiva the two vortex are still present and both attract almost the same mass flow, with the right vortex attracting a little big more since it's stronger.

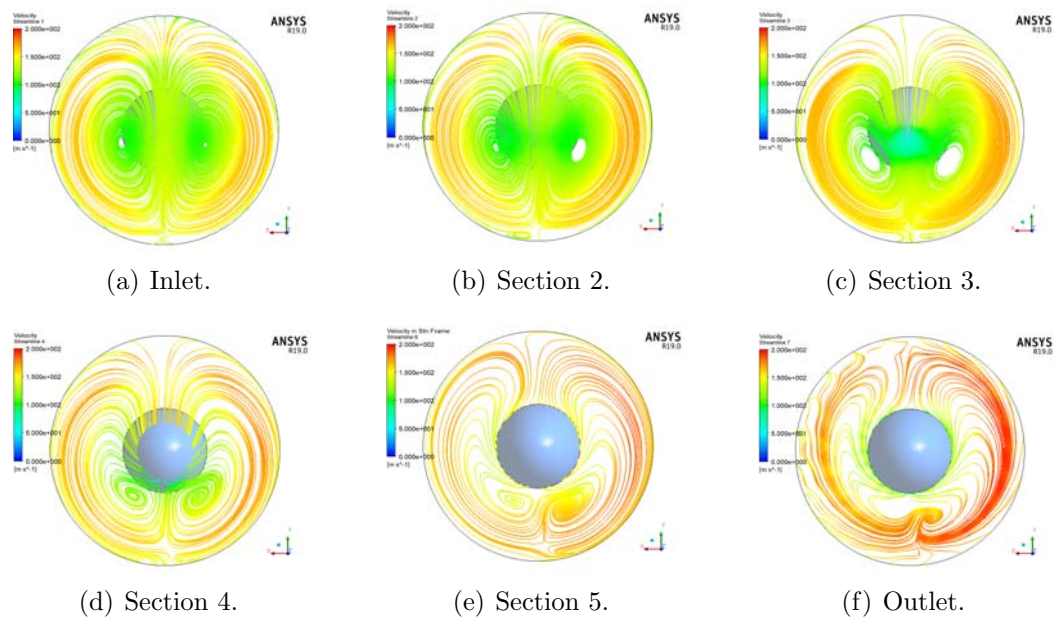


FIGURE 8.3: Velocity Streamline.

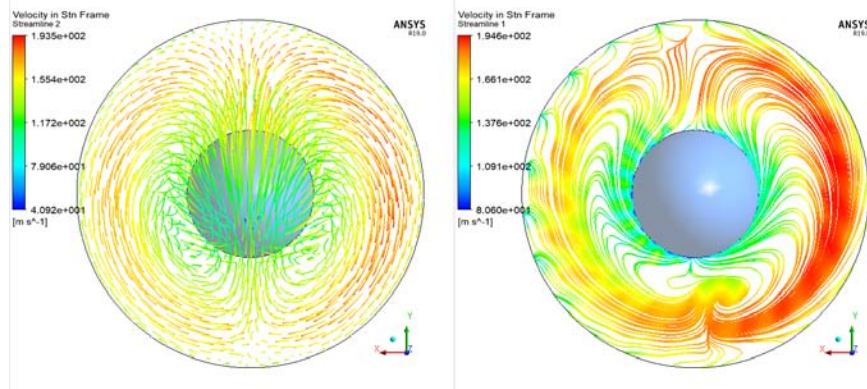


FIGURE 8.4: Velocity Streamline through the Ogive (Left) and at the Outlet (Right).

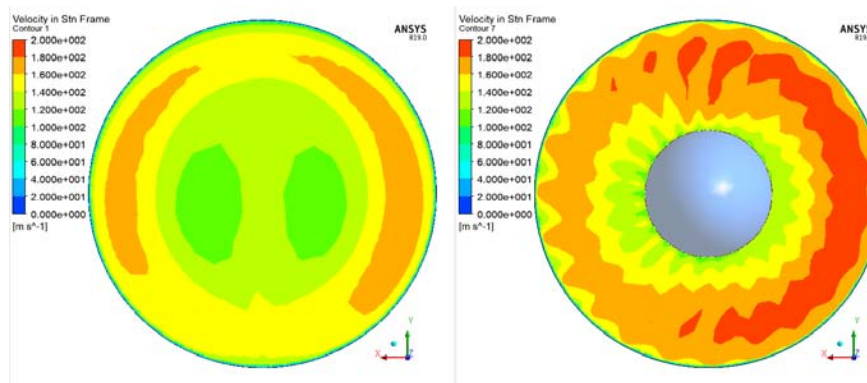


FIGURE 8.5: Inlet Velocity Contour (Left) and Outlet Velocity Contour (Right).

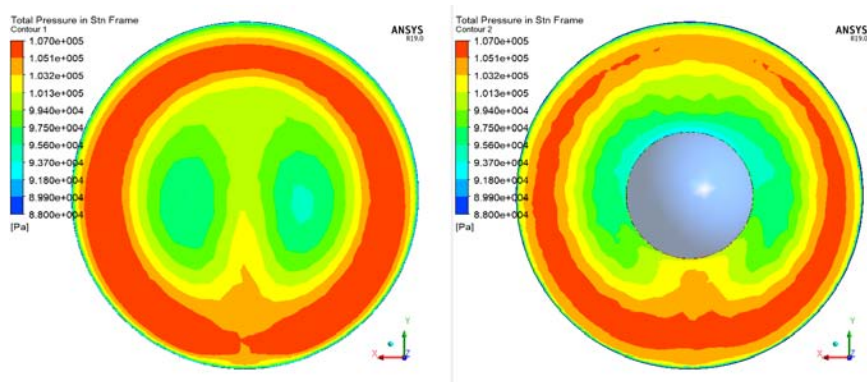


FIGURE 8.6: Total Pressure Contour at the Inlet (Left) and Outlet (Right) of the Ogive.

8.1.3 R67 Interaction with S-duct CP Best

Figure 8.7 and Figure 8.8 compare the inlet Mach number. Comparing to the baseline simulation it is clear that the cp best s-duct provide a better velocity field. The rotor can be divided in two side: The right side which is dominated by high inlet velocities; the left side with is dominated by velocities that are close to the peak efficiency. This is due to the central position of the vortex that is rotating in the cloackwise direction.

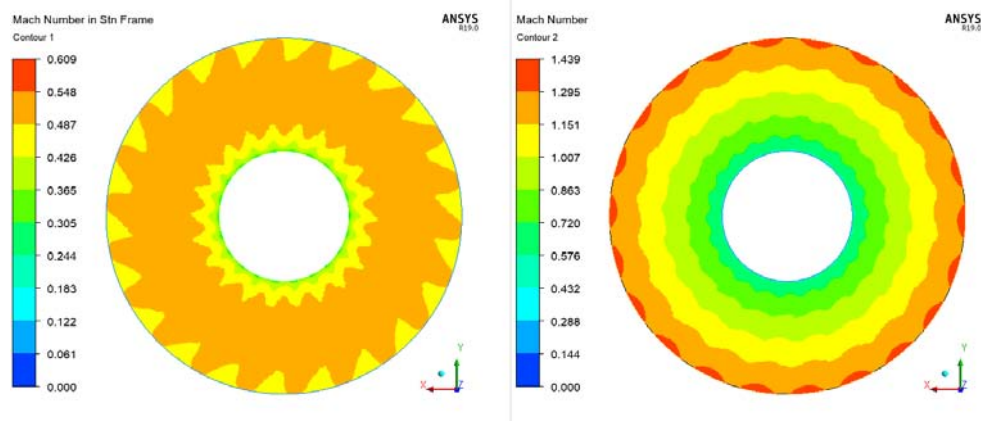


FIGURE 8.7: Inlet Mach Number Clean Conditions.

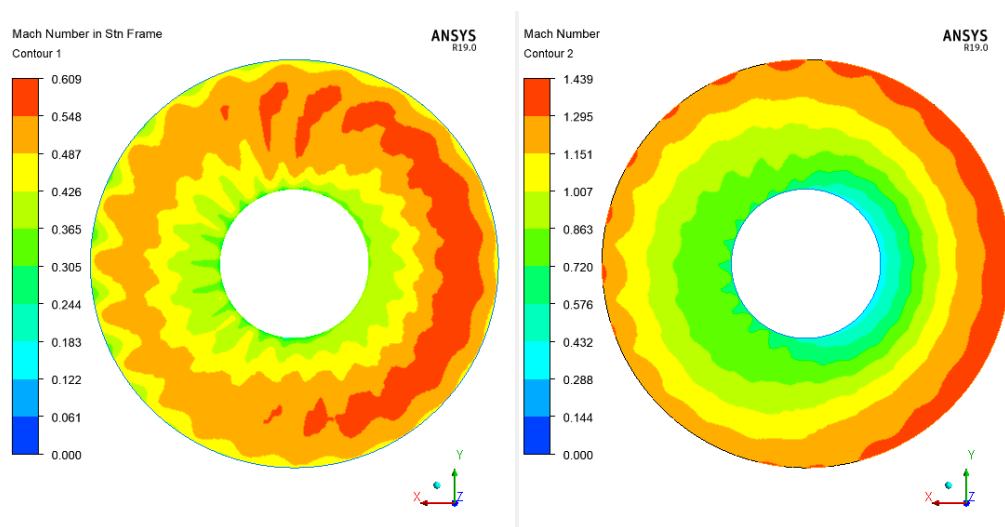


FIGURE 8.8: Inlet Mach Number CP Best.

Figure 8.11 and 8.9 describe the absolute and relative components. What is important to notice is how all the components have improved compared to the baseline and they are really closer to the components present in the clean flow simulation. Figure 8.9 and 8.10 show how the components have improved but still there are some distortions. In particular the velocity streamwise has higher velocities in the right side. The velocity spanwise has two opposite region, one on the top where the flow has the velocity component in the direction of the tip while the other one in the bottom side where the flow has the velocity component in the direction of the hub. In the end the absolute circumferential velocity is the one who has the better improvement but still due to the presence of the vortex form an inlet distortion. It can be seen that on the outer region the circumferential velocity has drastically decrease reaching value around -20 [m/s] on the left side and $+20$ [m/s] while in the inner part the velocities reach higher value and change sign meaning that the flow change direction. Figure 8.11 and 8.12 compare the absolute flow angle and the relative component. Also here it can be seen how the flow angle has drastically improve having value close to 90° meaning that the inlet absolute velocity is almost axial. In the end also the relative components has seen a big improvement with the circumferential velocity being the very close to the clean condition.

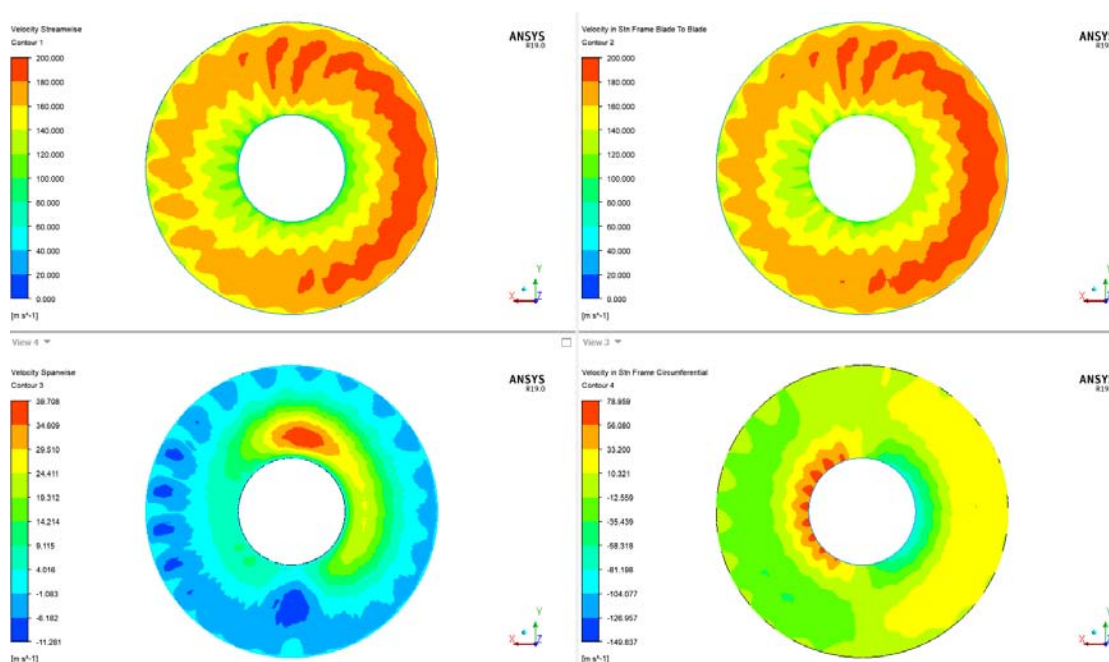


FIGURE 8.9: Streamwise(Top Left),Blade to Blade Abs (Top Right), Spanwise(Bot Left), Crf Abs(Bot Right).

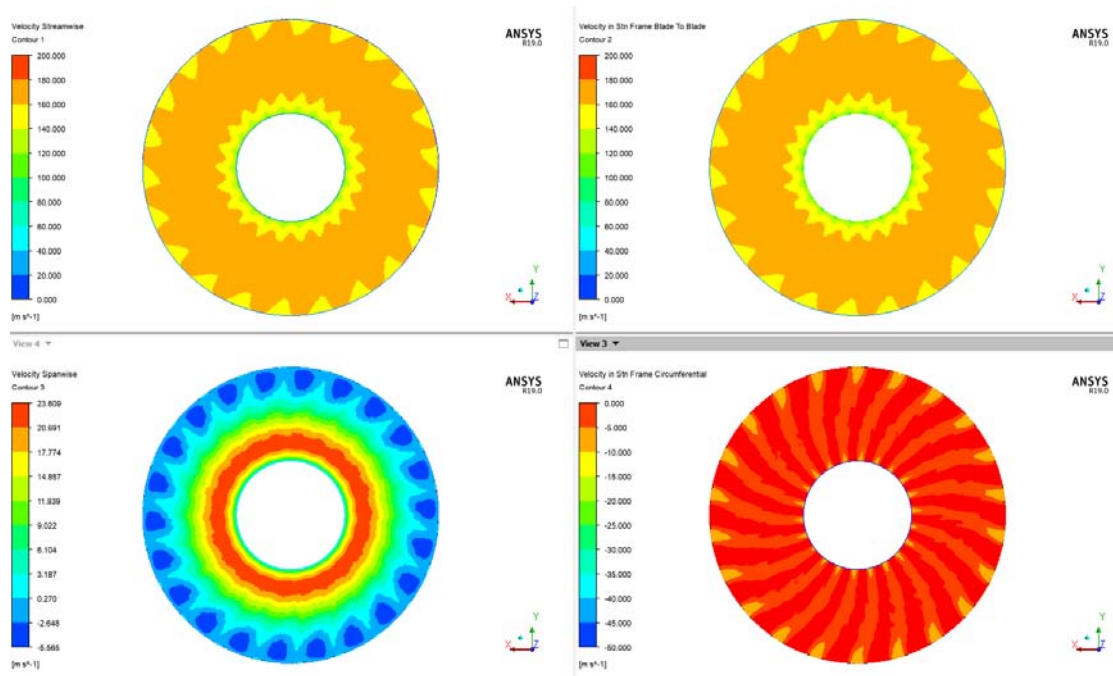


FIGURE 8.10: Streamwise(Top Left),Blade to Blade Abs (Top Right), Spanwise(Bot Left), Crf Abs(Bot Right)Clean Flow.

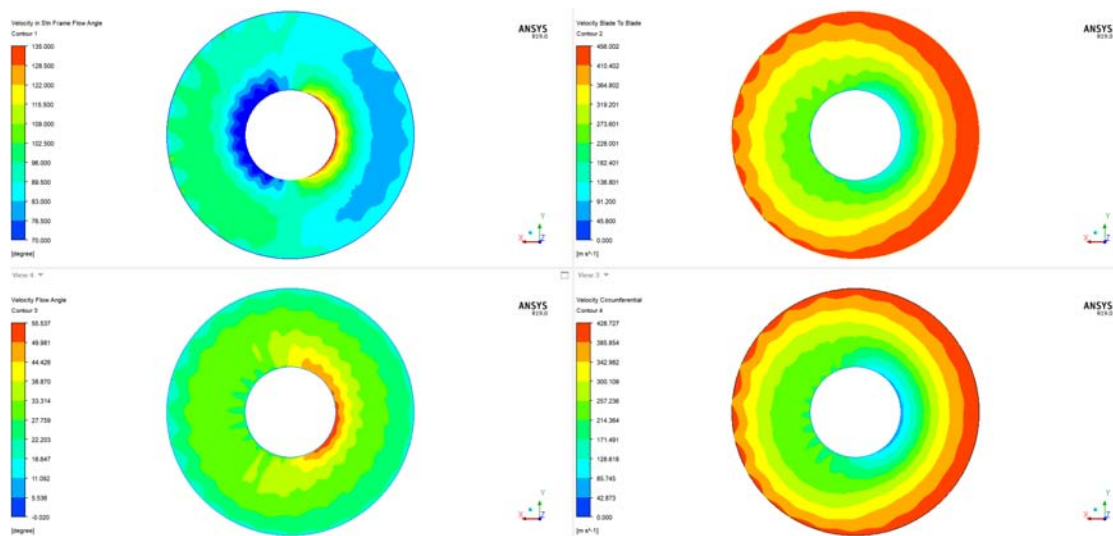


FIGURE 8.11: Flow Angle Abs(Top Left),Blade to Blade Rel(Top Right), Flow Angle Rel(Bot Left), Crf Rel(Bot Right).

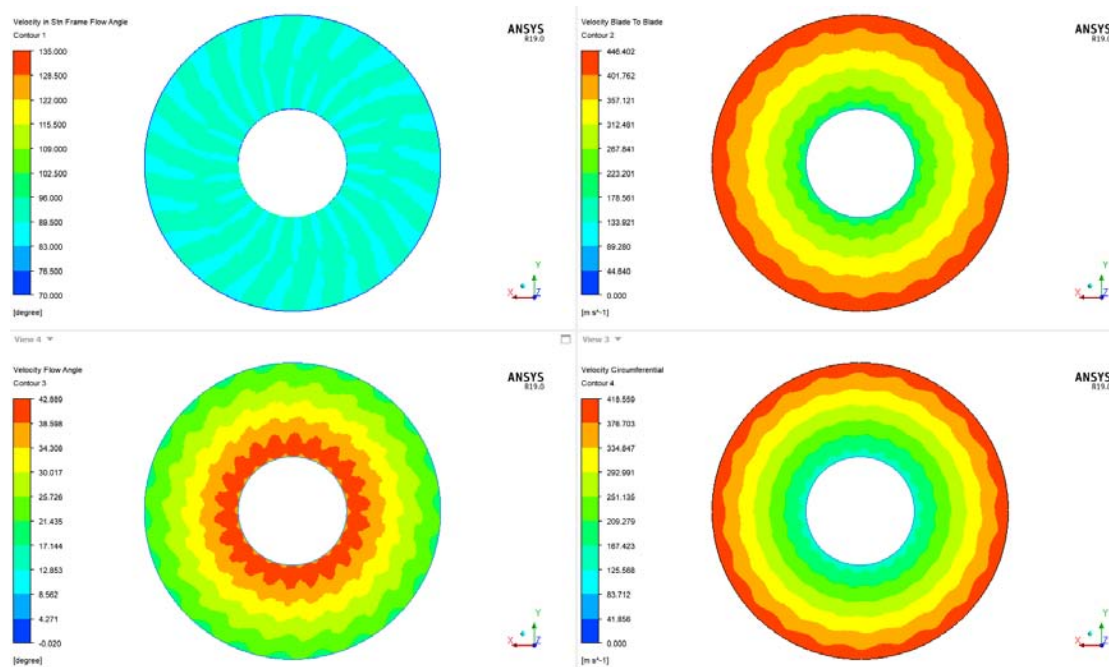


FIGURE 8.12: Flow Angle Abs(Top Left),Blade to Blade Rel(Top Right), Flow Angle Rel(Bot Left), Crf Rel(Bot Right) Clean Flow.

After the absolute and the relative components analysis, Figure 8.13 shows the blade to blade contour. It is clear now why this s-duct provide better performance compared to the baseline. Referring to span=0.8 the position of the shock waves has drastically improved. Now the fan can be divided into two region. The right side from blade 6 to blade 17 is characterized by oblique shock waves due to the higher inlet Mach number. The opposite side from blade 18 to blade 5 is characterize by normal shock waves near the leading edge that is the best condition for a transonic compressor. Near the hub the blade to blade countour is different. In the right side is dominated by low inlet velocities while on the left side it has higher velocities compared to the clean conditions. To resume the right side of the fan near the hub is dominated by lower velocities than the clean flow. Near the tip the right side of the flow is dominated by higher velocities than the clean flow. The left side has the opposite characteristic of the right side.

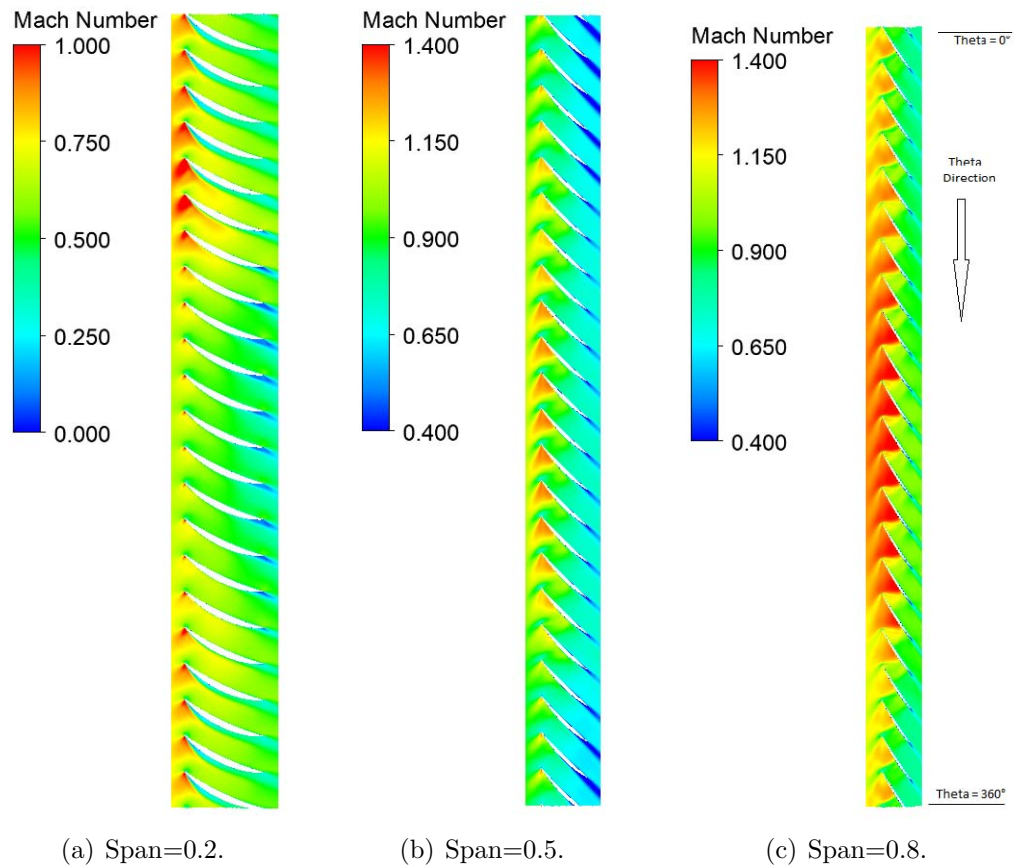


FIGURE 8.13: Blade to Blade Contour CP Best.

8.1.4 S-duct S.M.E. Best and Trade

Due to his similarity with the s-duct best CP for the all S.M.E. best and trade simulation, it will be reported only the main conotur without a deep description. From the picture below it can be seen that both duct create two counter rotating vortices in the middle part of the duct.

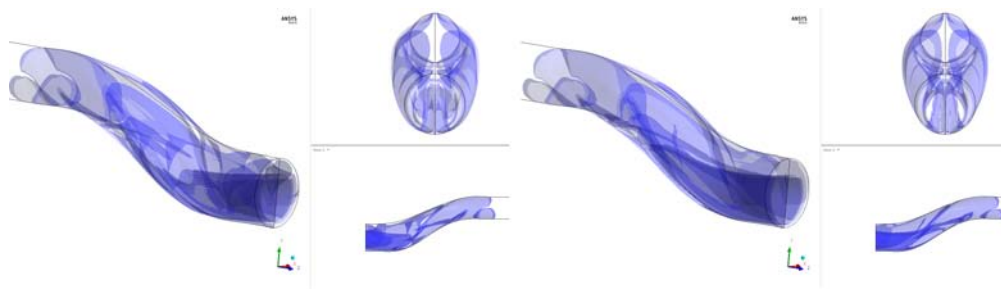


FIGURE 8.14: Vorticity Trade(Left) and S.M.E Best(Right).

8.1.5 Ogive Interaction with S-duct S.M.E. Best and Trade

As Figure 8.15 and 8.16 show the streamline and the velocity contour. The single vortex formation phenomena has been already described in section 8.1.2. While the velocity contour are pretty much the same as the best CP simulation. In the end the last contour reports the total pressure distortion.

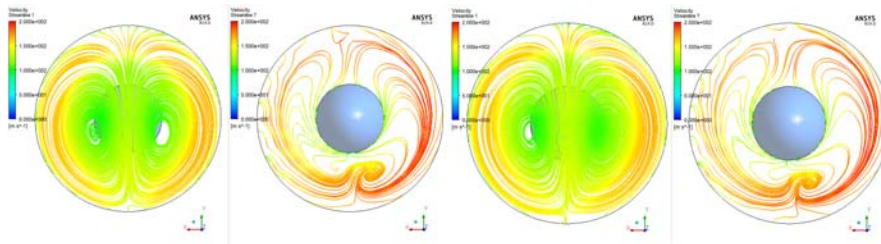


FIGURE 8.15: Streamline Inlet and Outlet S.M.E Best(Left) and Trade(Right).

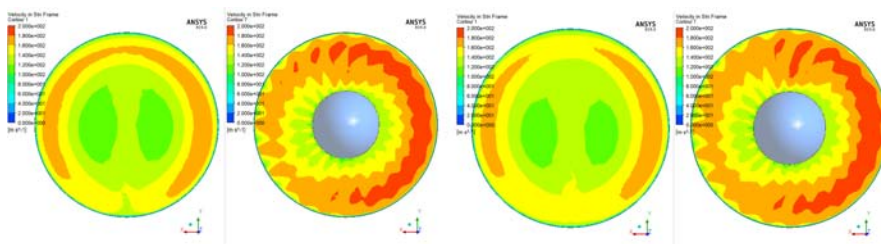


FIGURE 8.16: Velocity Inlet and Outlet S.M.E Best(Left) and Trade(Right).

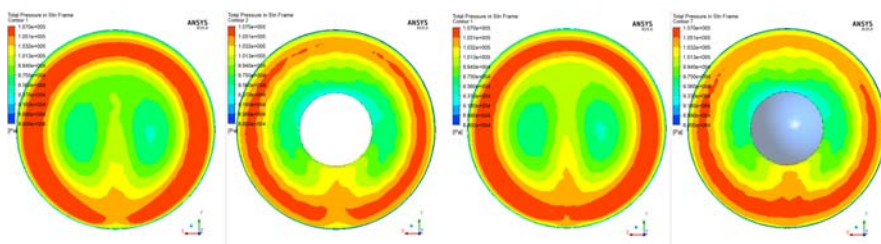


FIGURE 8.17: Total Pressure Inlet and Outlet S.M.E Best(Left) and Trade(Right).

8.1.6 R67 Interaction with S-duct S.M.E. Best and Trade

The blade to blade view reports the relative Mach number and as already said, there are two regions that are working in two different conditions, one near peak and the other one with oblique shock waves.

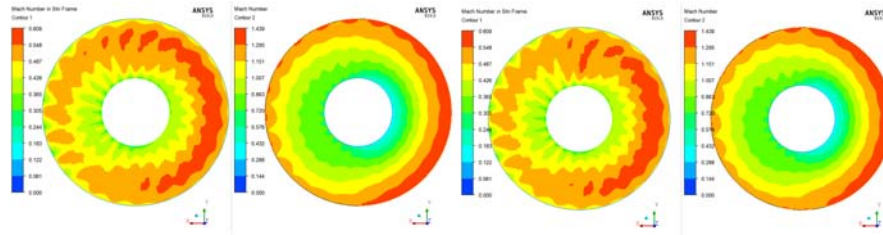


FIGURE 8.18: Mach Abs and Rel S.M.E Best(Left) and Trade(Right).

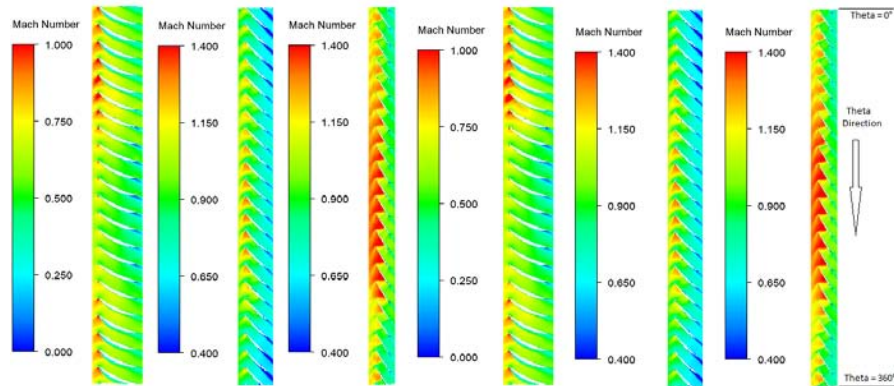


FIGURE 8.19: Blade-to-Blade span=0.2,0.5 and 0.8 S.M.E Best(Left) and Trade(Right).

8.2 DC60/S.M.E. optimisation and R67 interaction

Figure 8.20 shows the different performance between the baseline and the optimisation results. The graphs show that the new s-ducts obtained by the optimisation give better inlet conditions to the fan allowing it to work more efficiently. In fact, in Table 8.2 are reported the performance of each s-duct near the peak condition. The best results reach +0.98% over the polytropic efficiency of the baseline and it is also a huge improvement compare to the previous optimisation.

TABLE 8.2: Baseline and Optimisation Performance Near Peak.

Model	\dot{m} [kg/s]	η_{is}	$\Delta\eta_{is}$	η_{pol}	$\Delta\eta_{pol}$
Baseline	31.76	0.888567		0.894706	
Best DC60	31.74	0.896039	0.84%	0.901773	0.79%
Best S.M.E.	31.49	0.897677	1.03%	0.903506	0.98%
Trade Off	31.45	0.894769	0.70%	0.900665	0.67%

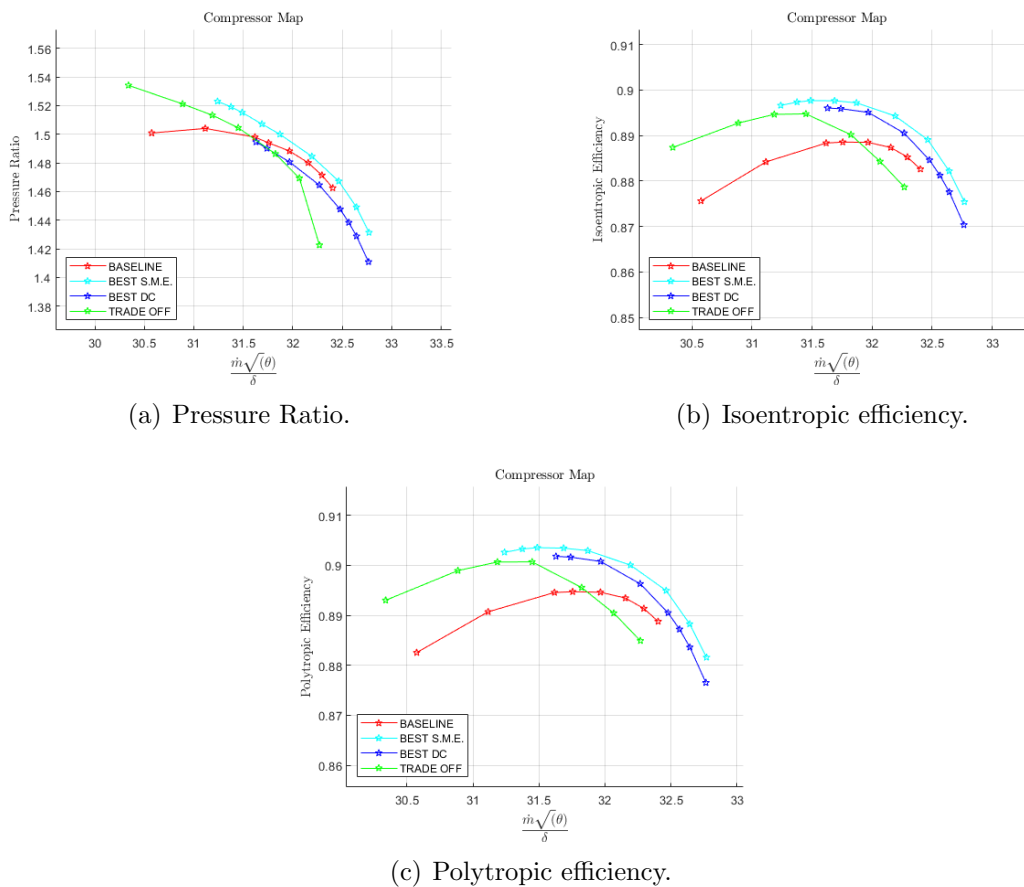


FIGURE 8.20: Compressor Map Comparison Between Baseline and Optimisation Results.

8.2.1 *S*-duct Best DC

As already described in Chapter 6 the DC60 best geometry creates two counter-rotating vortices placed on the middle part of the duct. Figure 8.21 shows the vortex structure inside the duct.

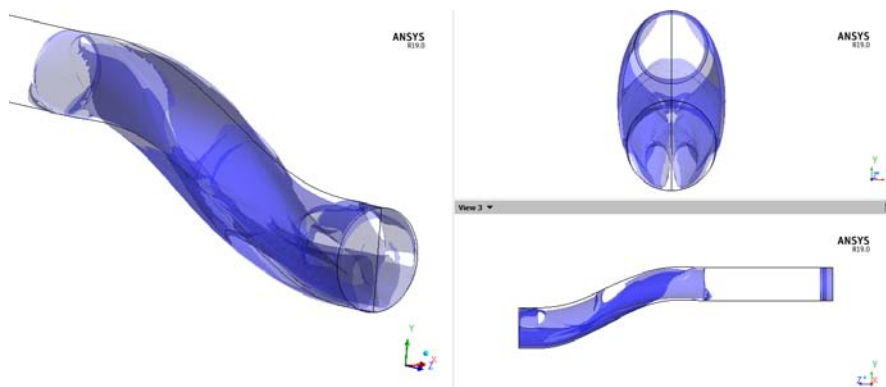


FIGURE 8.21: Vorticity of the *S*-duct Best DC.

8.2.2 Ogive Interaction with S-duct DC Best

In Figure 8.22, the velocity streamline for each section are reported. It can be noticed how the inlet conditions are different from the cp best simulation. In fact, the two counter-rotating vortices that enter in the ogiva domain have their core in a much lower position respect to the cp best and also the distance between the two vortices is lower. This anticipates the formation of the single vortex and leads to a more distorted velocity field. If the vortex merging phenomenon is anticipated, more mass flow will be attracted to the right and to the top left side giving as a result a velocity distribution represented in Figure 8.23.

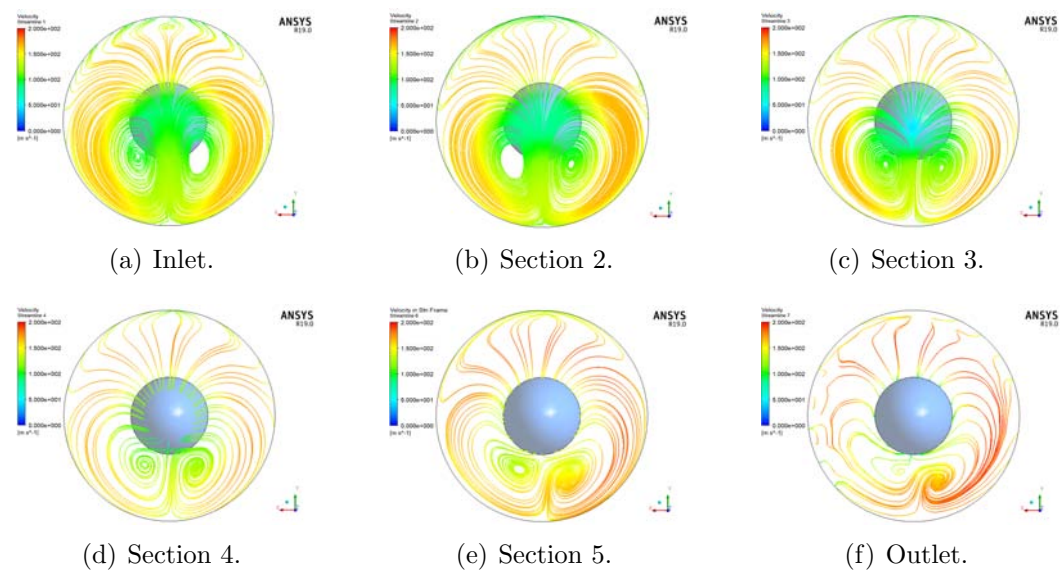


FIGURE 8.22: Velocity Streamline.

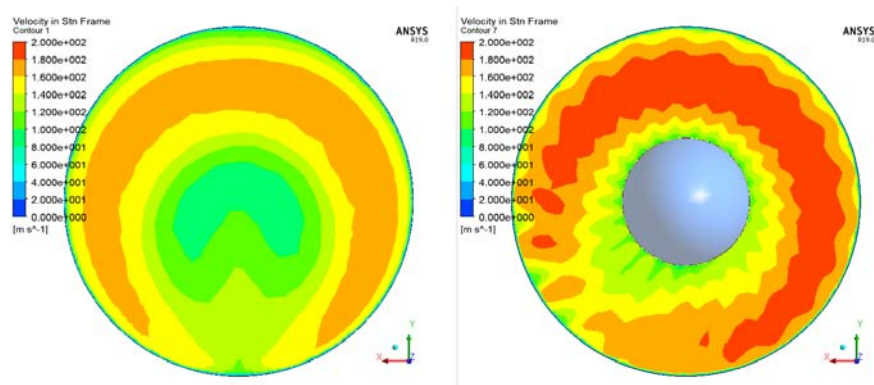


FIGURE 8.23: Inlet Velocity Contour (Left) and Outlet Velocity Contour (Right).

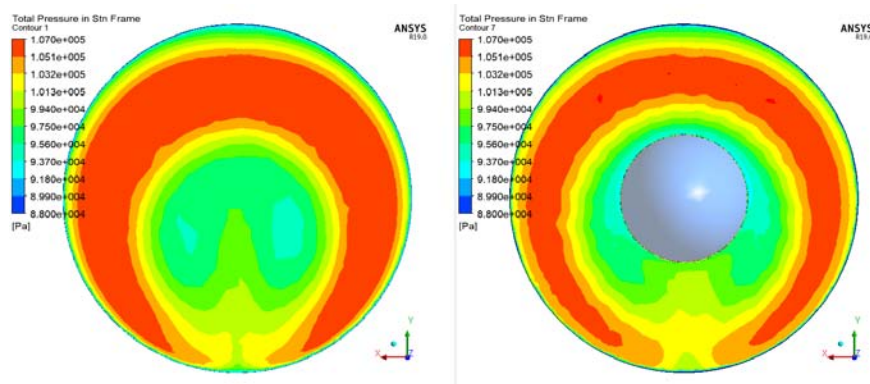


FIGURE 8.24: Total Pressure Contour at the Inlet (Left) and Outlet (Right) of the Ogive.

8.2.3 R67 Interaction with S-duct DC Best

From Figure 8.25 it is possible to see how the anticipated formation of the single vortex affect the inlet relative Mach number. The region with an higher velocity has shift position toward the low side compare to the best cp simulation and on the lower left side the Mach number is lower than the clean condition. This leads to have more blades that work with oblique shock wake or detached rather than normal and close to the tip, decreasing the overall efficiency. As for the previous optimisation, the fan can be divided in two regions. In fact from the blade to blade view it is clear that from blade number 1 to 18 the shock is oblique while from blade number 19 to 22 the shock is almost normal but detached from the blade. This means that only few blades are working near the peak efficiency while on the best cp simulation almost 10 blades had the normal shock wave. So the main conclusion is that to have better inlet condition to the fan, not only the size and the position of the 2 vortex is important, but also the distance between the two core of the vortices when they touch the ogive and start splitting.

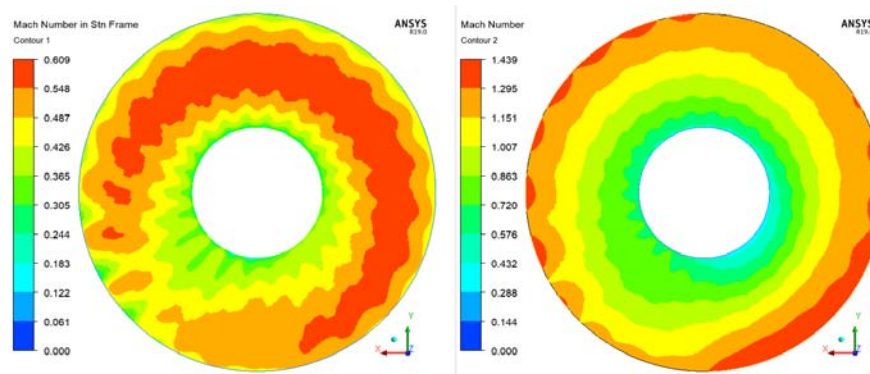


FIGURE 8.25: Inlet Mach Number DC Best.

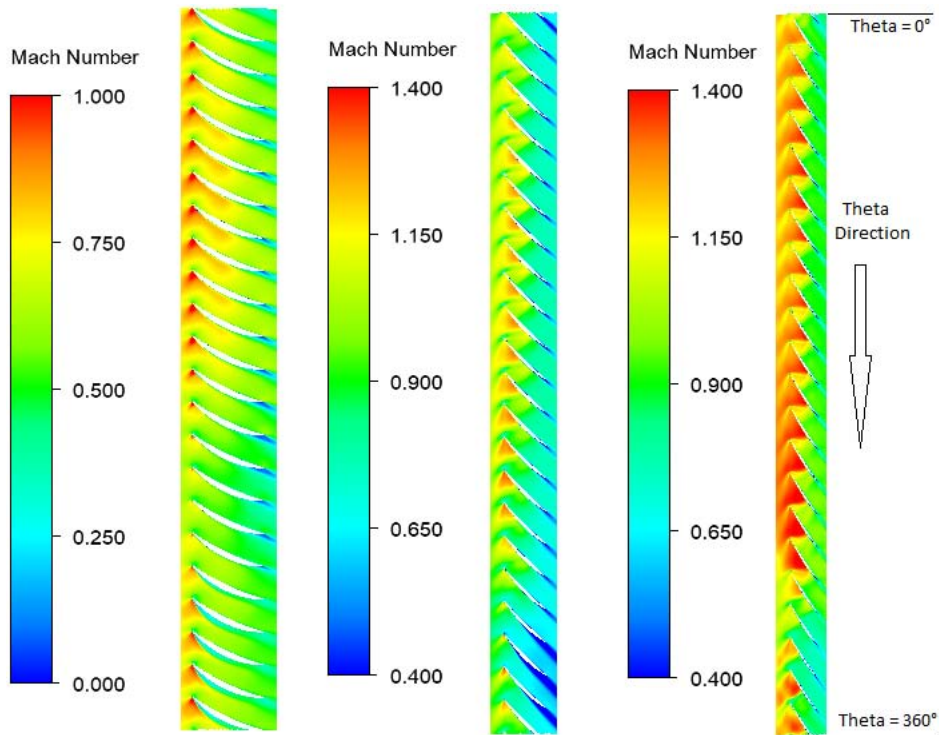


FIGURE 8.26: Blade-to-Blade span=0.2,0.5 and 0.8 DC best.

8.2.4 S-duct Best S.M.E.

As already described in Chapter 6 the S.M.E. best geometry create two counter-rotating vortices placed on the middle part of the duct that are highlighted in Figure 8.27 below.

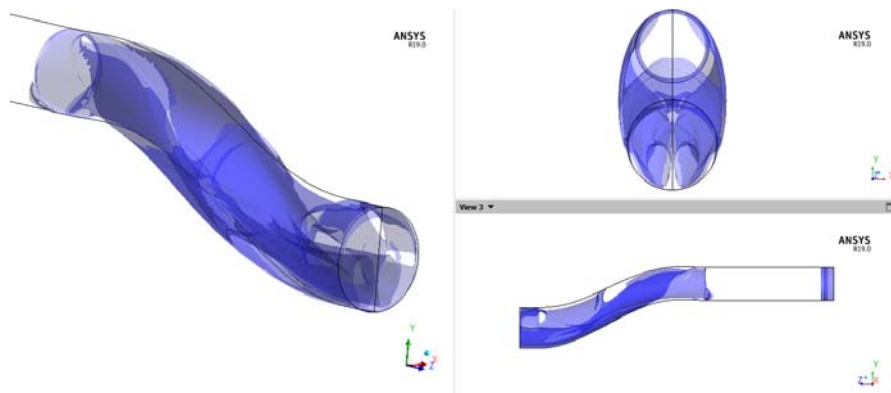


FIGURE 8.27: Vorticity of the S-duct Best S.M.E..

8.2.5 Ogive Interaction with S-duct S.M.E. Best

Figure 8.28 helps to understand why this s-duct provides better inlet conditions to the fan. It can be noticed that the two vortices are placed in a more center position and the distance between the 2 core is higher compared to the dc best and cp best simulation. This initial position of the two vortices delays the merging phenomena. In fact, if the vortices have their core distance increased, the influence that the right vortex has on the left one is much less. To destroy the left vortex and start the merge phenomena, two main actor give their contribution. The first one is the rotational speed of the fan and it is constant for every s-duct simulation. The second one is the right vortex that acts stronger or weaker depending on the relative position of the two vortices and his position change depending on the s-duct shape. From the last section the merging vortex phenomenon has almost finish but his position is pretty central.

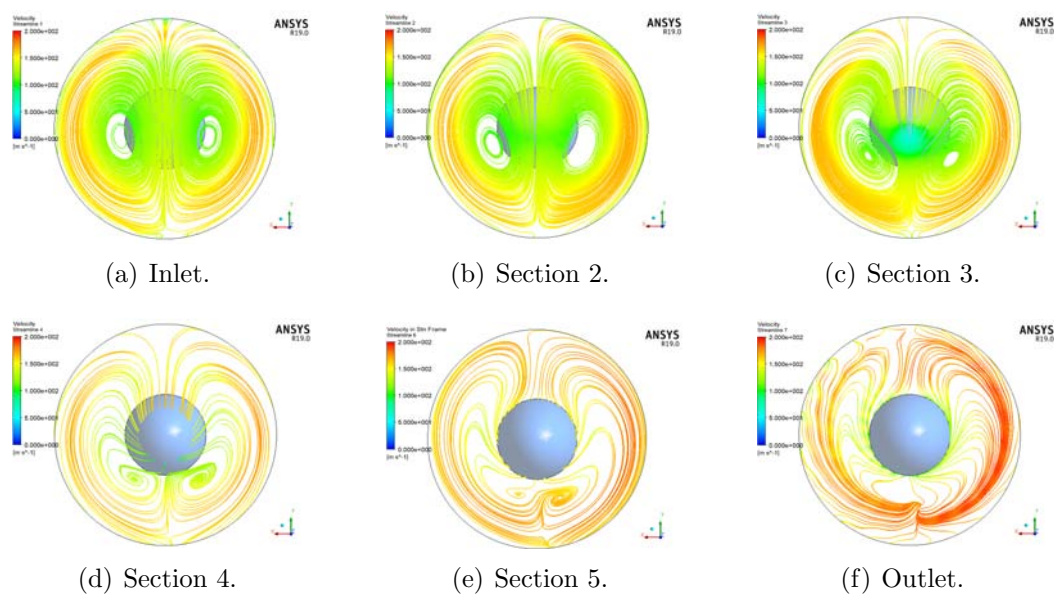


FIGURE 8.28: Velocity Streamline.

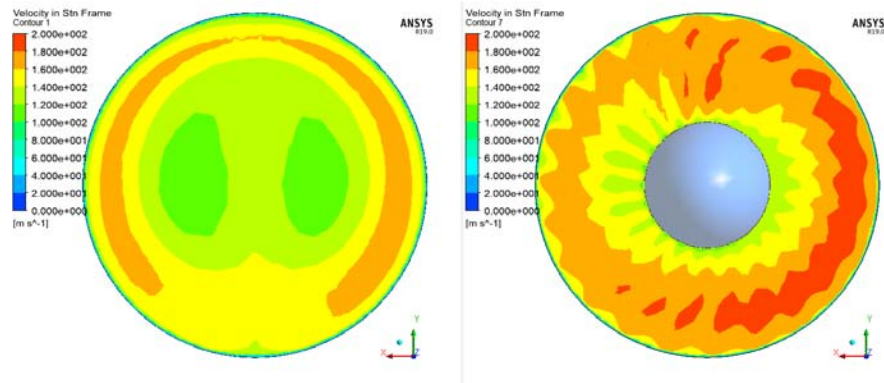


FIGURE 8.29: Inlet Velocity Contour (Left) and Outlet Velocity Contour (Right).

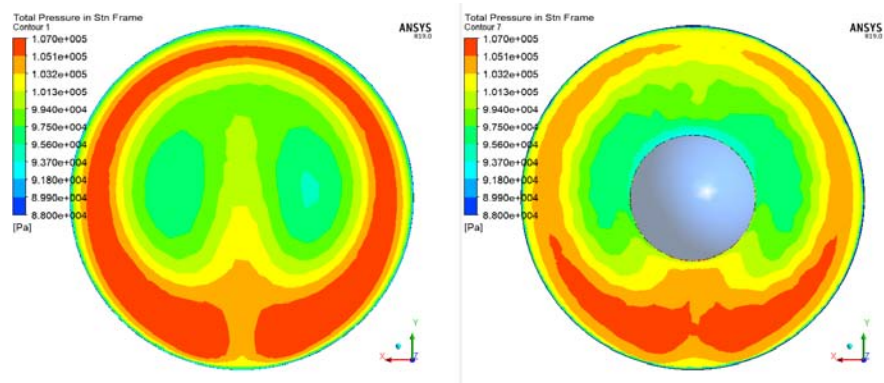


FIGURE 8.30: Total Pressure Contour at the Inlet (Left) and Outlet (Right) of the Ogive.

8.2.6 R67 Interaction with S-duct SME Best

Figures 8.31, 8.32, 8.33 and 8.34 show the inlet condition and the blade to blade view. It is important to notice how the inlet mach number has become more symmetric and how the shock wave distribution has improved. More than half of the fan is working with normal shock while the rest is working with oblique shock. This increase the efficiency of the fan since it is directly related to the shock wave position.

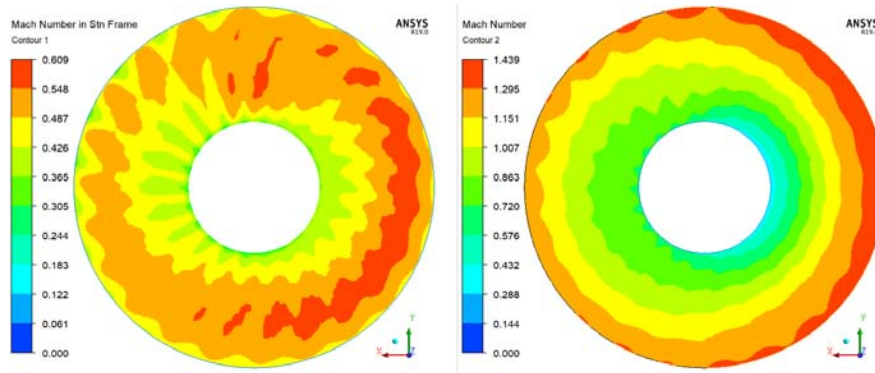


FIGURE 8.31: Inlet Mach Number SME Best.

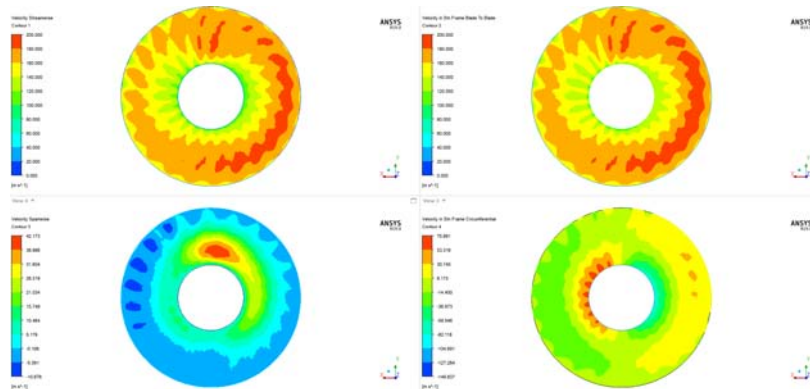


FIGURE 8.32: Streamwise(Top Left),Blade to Blade Abs (Top Right), Spanwise(Bot Left), Crf Abs(Bot Right).

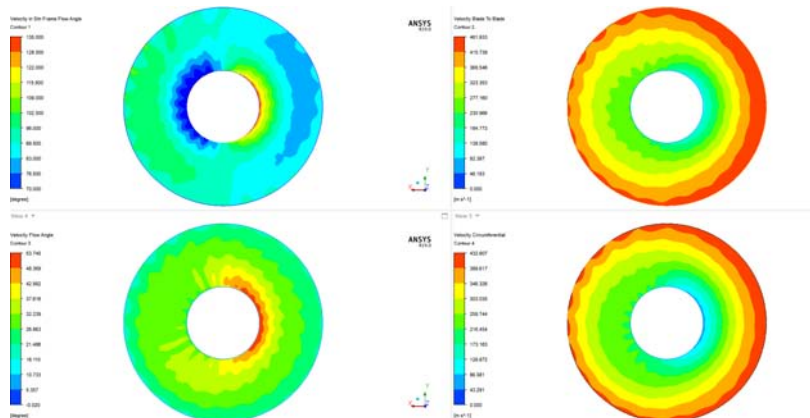


FIGURE 8.33: Flow Angle Abs(Top Left),Blade to Blade Rel(Top Right), Flow Angle Rel(Bot Left), Crf Rel(Bot Right).

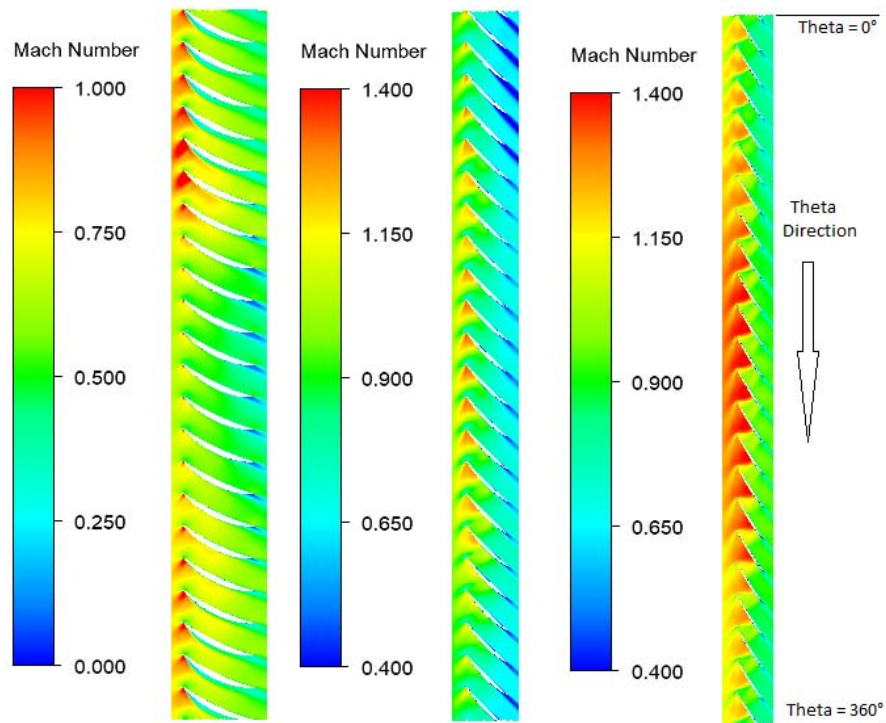


FIGURE 8.34: Blade-to-Blade span=0.2,0.5 and 0.8 S.M.E. best.

8.2.7 S-duct Trade Off

In the Figure below it is highlight the vortex structure inside the s-duct already described in Chapter 6.

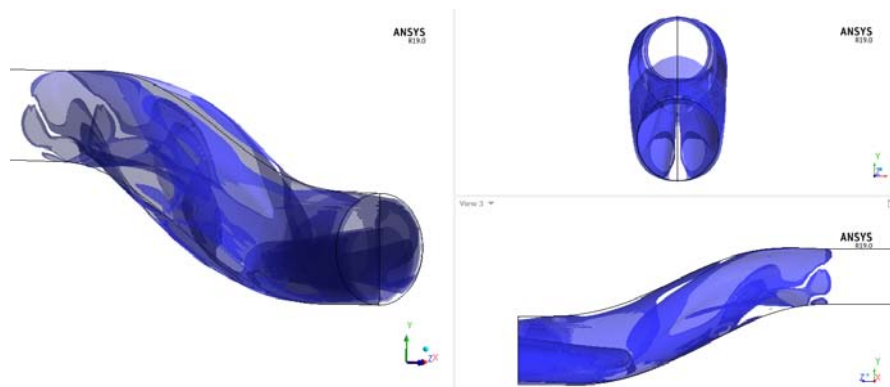


FIGURE 8.35: Vorticity of the S-duct Trade Off.

8.2.8 Ogive Interaction with S-duct Trade Off

Figure 8.36 shows the formation of the single vortex. As already said, the two counter rotating vortices have their core position under the center of the ogive. This leads to an anticipated vortex formation that causes a more distorted flow to the fan.

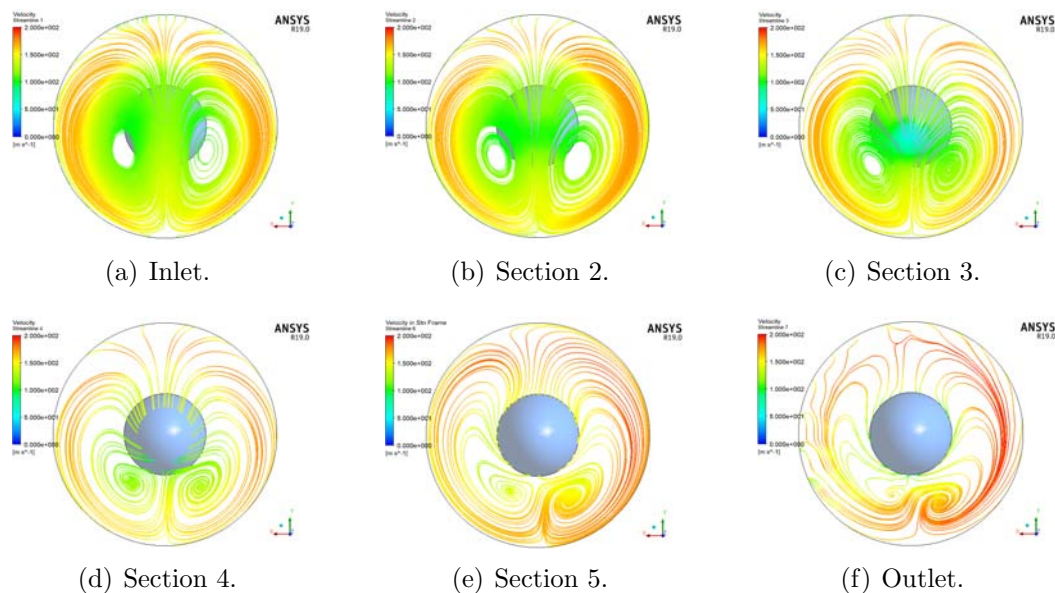


FIGURE 8.36: Velocity Streamline.

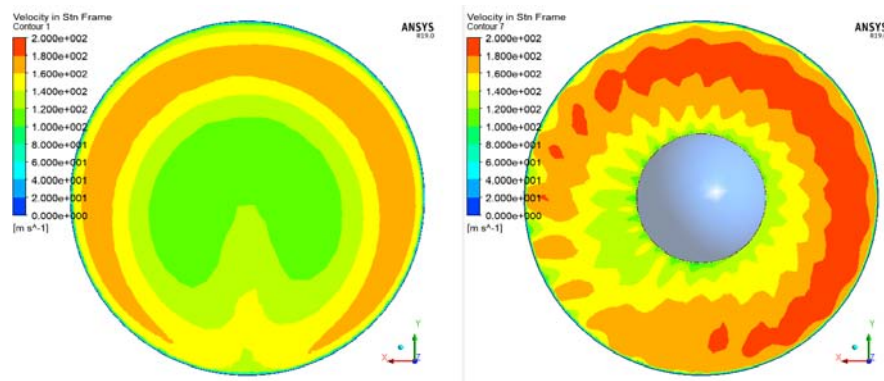


FIGURE 8.37: Inlet Velocity Contour (Left) and Outlet Velocity Contour (Right).

8.2.9 R67 Interaction with S-duct Trade Off

As Figure 8.40 shows, the efficiency of the fan is deteriorated due to the high speed on right side of the fan and the low speed on the bottom left.

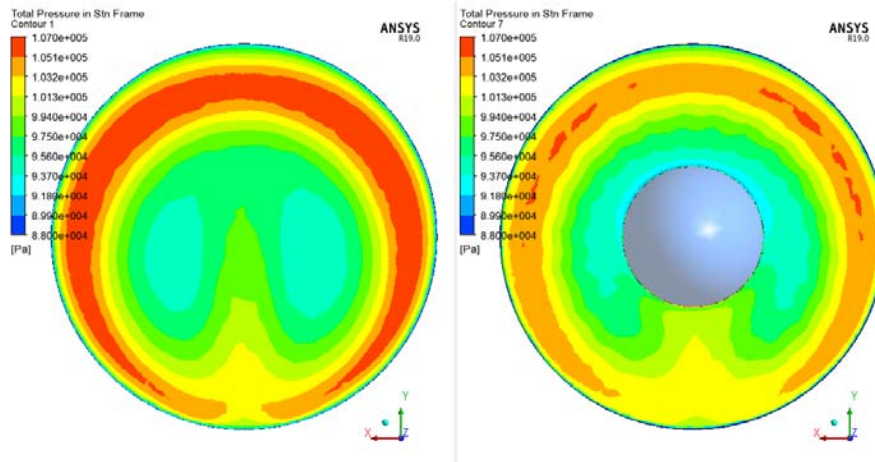


FIGURE 8.38: Total Pressure Contour at the Inlet (Left) and Outlet(Right)of the Ogive.

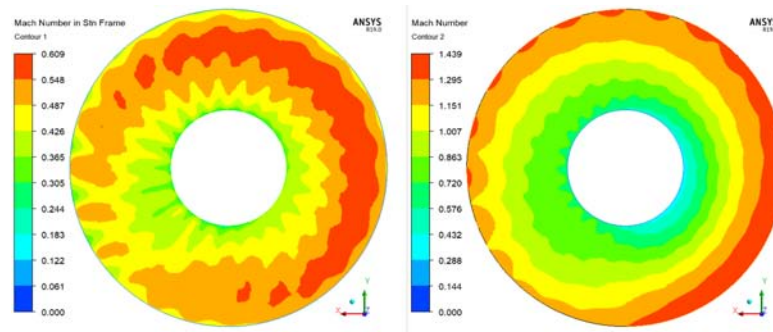


FIGURE 8.39: Inlet Mach Number Trade Off.

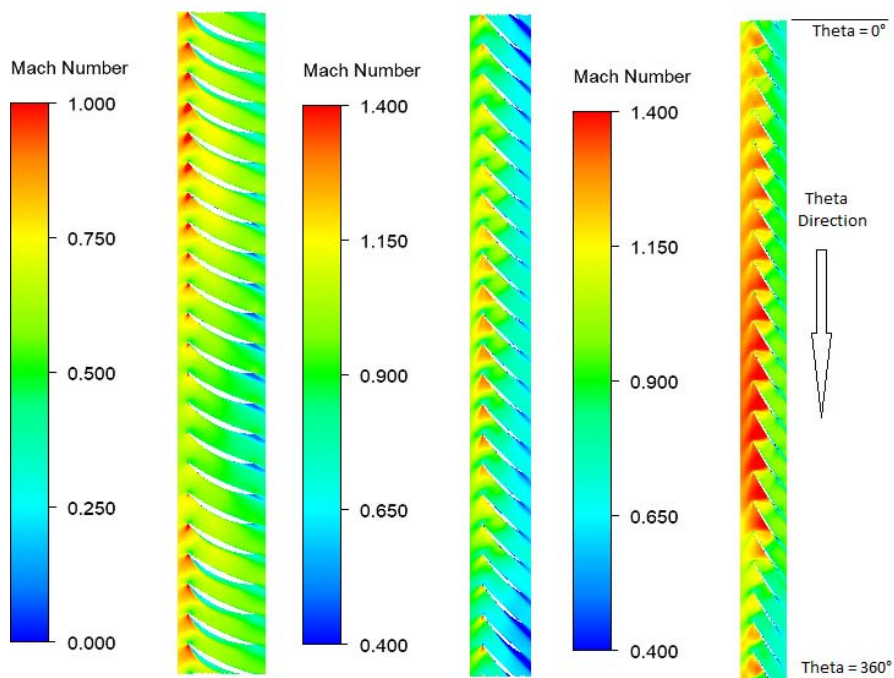


FIGURE 8.40: Blade-to-Blade span=0.2,0.5 and 0.8 Trade Off.

8.3 CP/Swirl Optimisation and R67 interaction

As it is possible to notice from Table 8.3 the trade off simulation give good results while the best swirl seem to be inefficient. To better understand how the flow evolve in the next sections it will be analyse the interaction with the ogive and the rotor 67.

TABLE 8.3: Baseline and Optimisation Performance Near Peak.

Model	\dot{m} [kg/s]	η_{is}	$\Delta\eta_{is}$	η_{pol}	$\Delta\eta_{pol}$
Baseline	31.76	0.888567		0.894706	
Best Swirl	32.46	0.89086	+0.26%	0.896814	+0.24%
Trade Off	32.67	0.898006	+1.06%	0.903649	+1.00%

8.3.1 S-duct Best Swirl

As it is possible to notice from Figure 8.41, the s-duct creates four vortices on the AIP. Two that rotate in the counterclockwise direction on the left side and two that rotate in the clockwise direction on the right side.

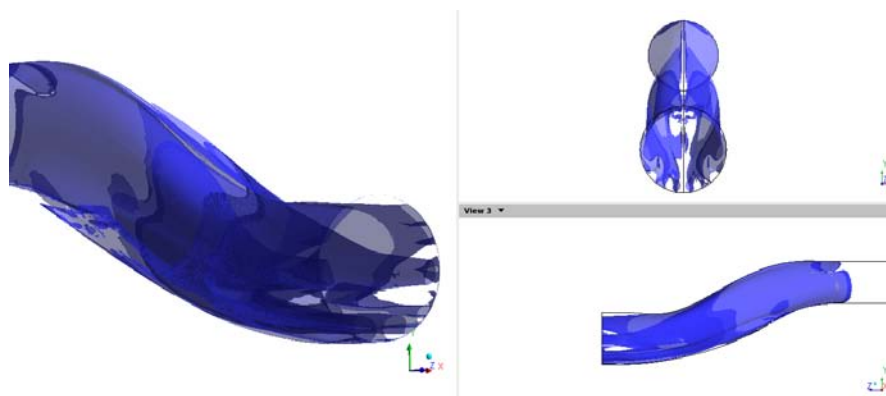


FIGURE 8.41: Vorticity of the S-duct Best Swirl.

8.3.2 Ogive Interaction with S-duct Swirl Best

From Figure 8.42 it can be seen how the flow evolves in the ogive domain. The two counter rotating vortices in the middle follow the same phenomena described in Chapter 7 with the baseline simulation. These two vortices merge together and

form a single vortex rotating in the clockwise direction. The two external vortices are also affected by the rotational speed of the fan but since they are rotating in opposite direction their behaviour is different. The external left vortex, since is rotating in the same direction of the fan, is compressed towards the outer perimeter and then almost destroyed by the rotational speed of the fan and by the influence of the central vortex that has been generated. The external right vortex is also affected by the central vortex that is stronger and attracts the little vortex. In the end a single vortex on the bottom right side of the rotor is generated and the velocity field is pretty similar to the baseline with the lower left side having lower velocities compared to the clean flow.

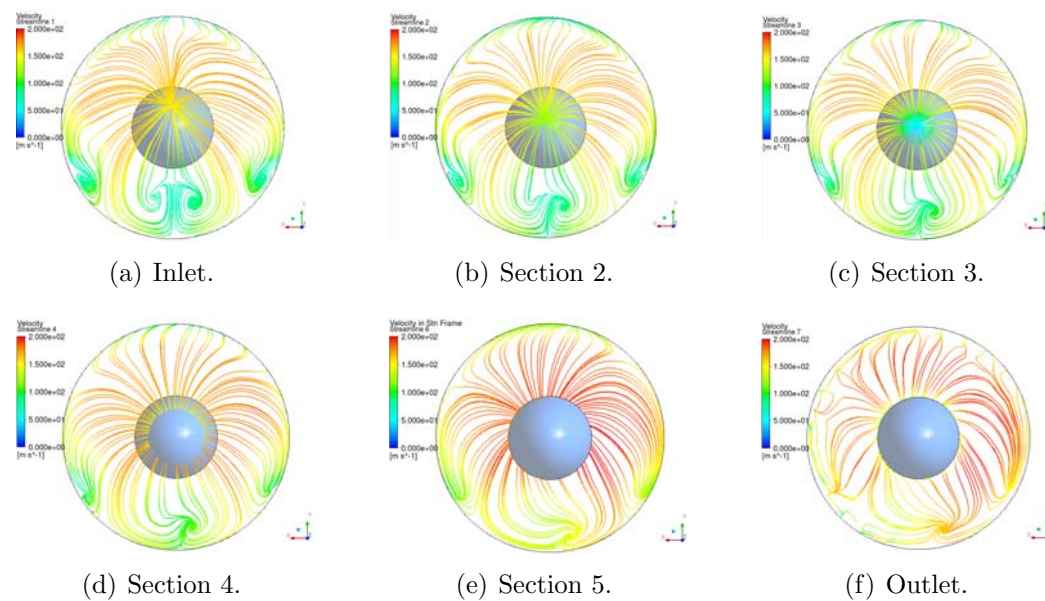


FIGURE 8.42: Velocity Streamline.

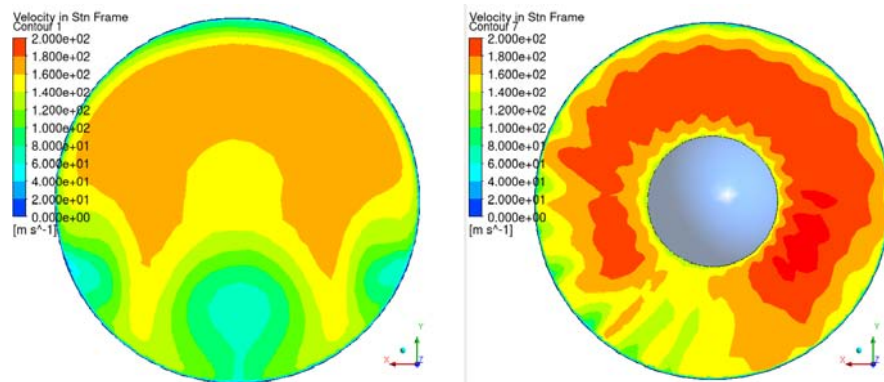


FIGURE 8.43: Inlet Velocity Contour (Left) and Outlet Velocity Contour (Right).

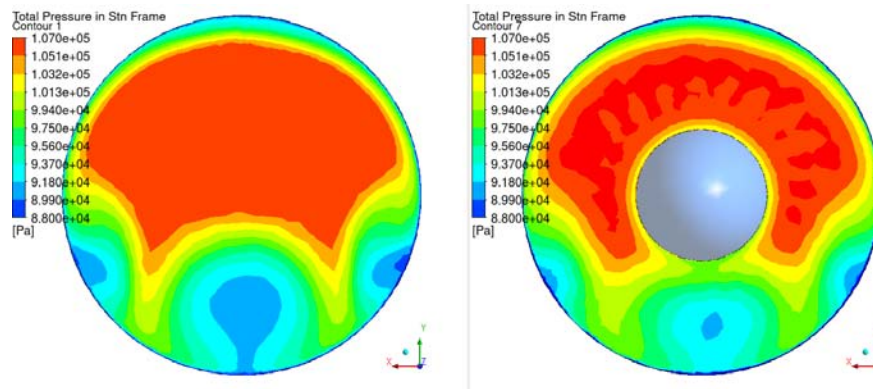


FIGURE 8.44: Total Pressure Contour at the Inlet (Left) and Outlet (Right) of the Ogive.

8.3.3 R67 Interaction with S-duct Swirl Best

Figure 8.45 shows the relative inlet Mach number. The trend of the relative Mach number is really close to the baseline simulation, with the lower left side dominated by low inlet velocities. This bad inlet conditions affect the fan performance and in the Figure 8.48 the shock waves are very different for each blade. In the blade to blade view it is clear why the efficiency of this simulation is so low. Many blades are working in a almost choking conditions while some other blades experience only a sonic bubble without the shock wave.

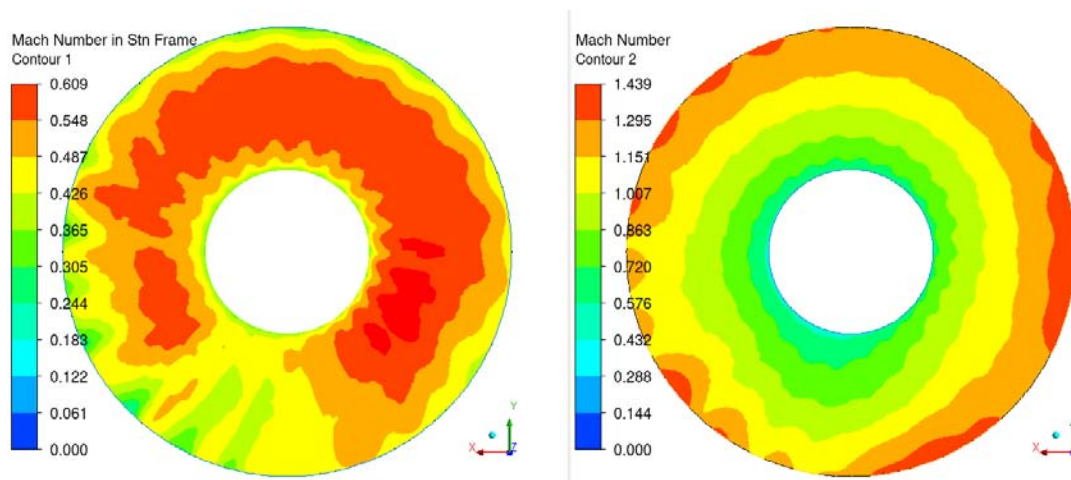


FIGURE 8.45: Inlet Mach Number Swirl Best.

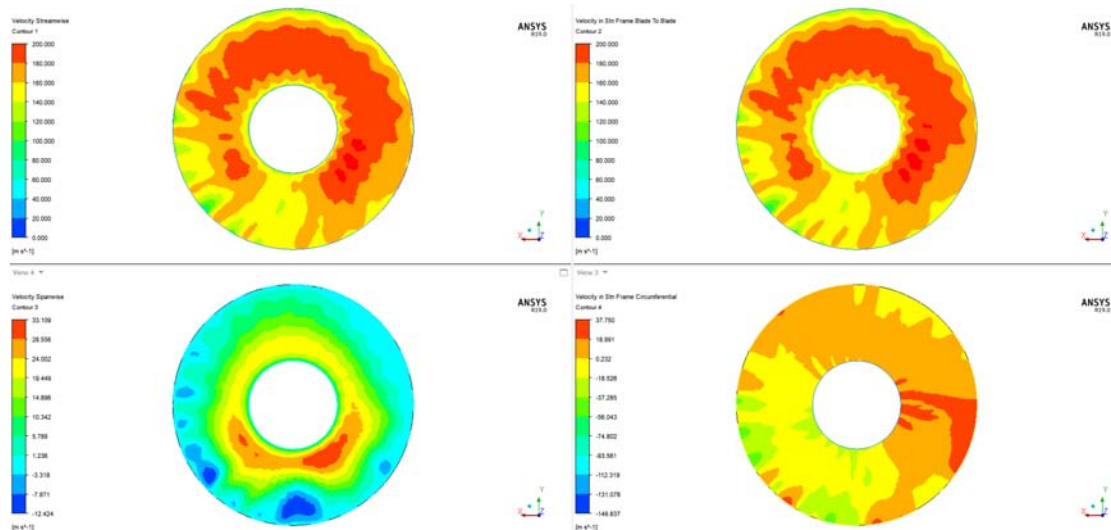


FIGURE 8.46: Streamwise(Top Left),Blade to Blade Abs (Top Right), Spanwise(Bot Left), Crf Abs(Bot Right).

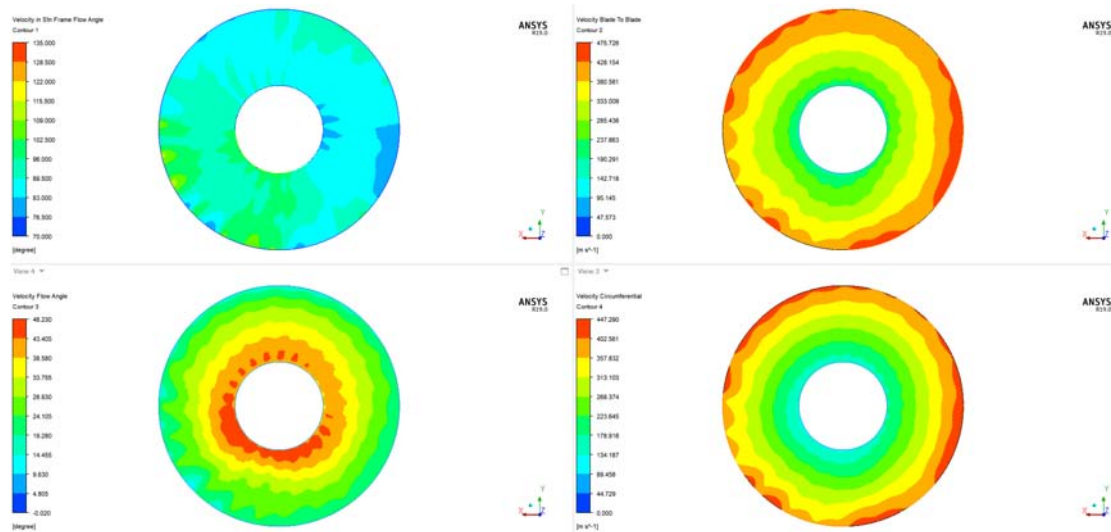


FIGURE 8.47: Flow Angle Abs(Top Left),Blade to Blade Rel(Top Right), Flow Angle Rel(Bot Left), Crf Rel(Bot Right).

8.3.4 S-duct Trade Off

As already described in chapter 6 the s-duct create 6 vortices on the AIP surface and the vorticity is highlight on Figure 8.49.

8.3.5 Ogive Interaction with S-duct Trade Off

From Figure 8.50 the structure of the vortices can be analysed. In the inlet condition 6 vortices are generated by the s-duct. The two little vortice right after the

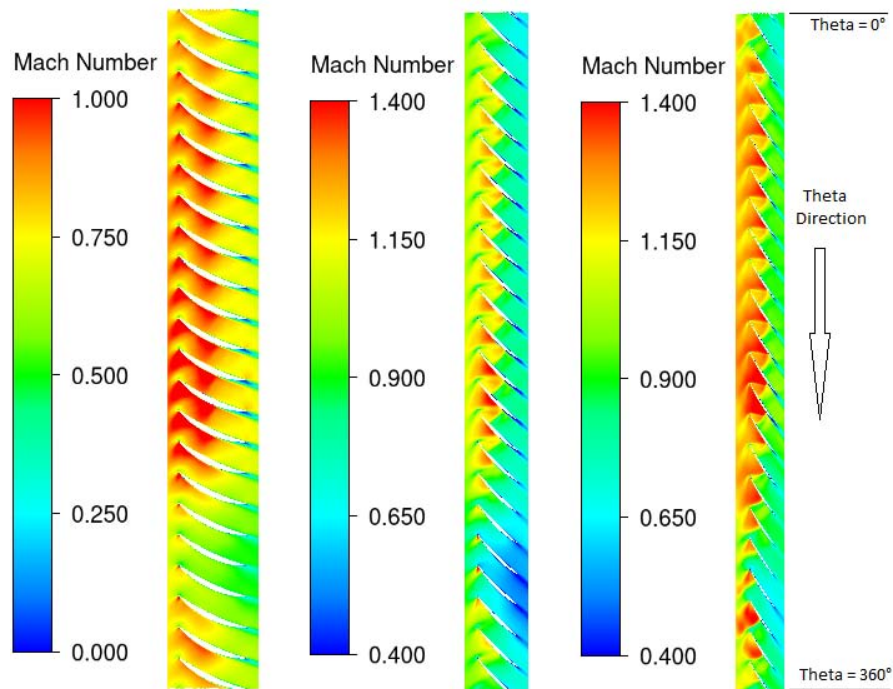


FIGURE 8.48: Blade-to-Blade span=0.2,0.5 and 0.8 Trade Off.

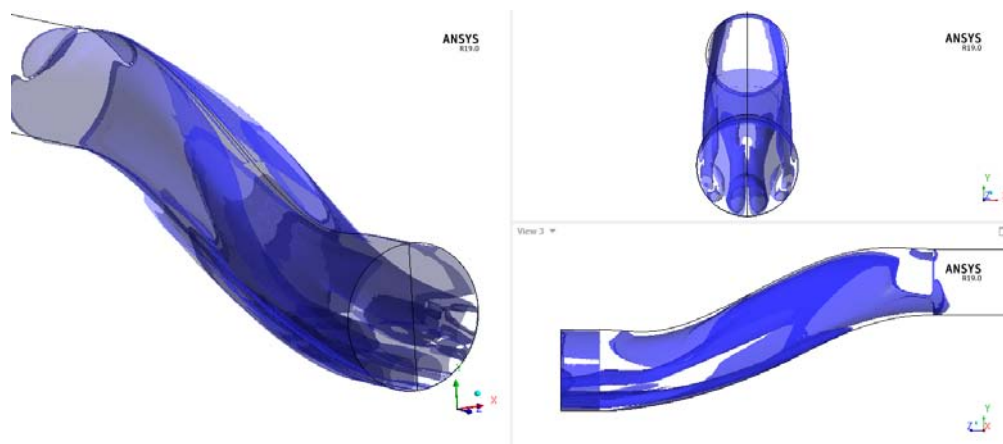


FIGURE 8.49: Vorticity of the S-duct Trade Off.

inlet domain of the ogive and before the ogive it self merge with the two external vortices. While the two vortices in the middle starts to merge as already described in Chapter 7. After touching the ogive the 4 vortices starts to converge and merge towards the bottom center. But unlike the previous simulation the vortices can't merge in time before the fan and three vortices are still present.

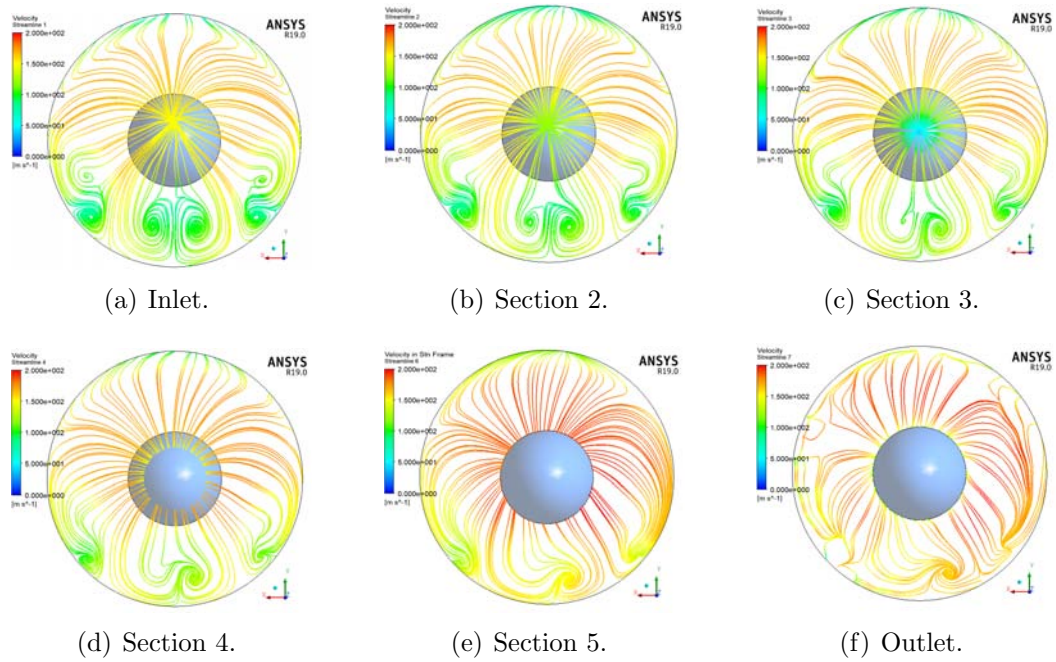


FIGURE 8.50: Velocity Streamline.

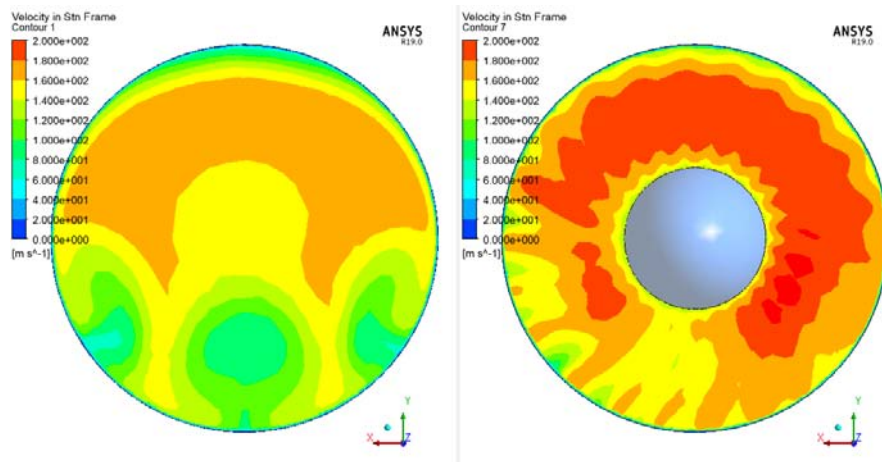


FIGURE 8.51: Inlet Velocity Contour (Left) and Outlet Velocity Contour (Right).

8.3.6 R67 Interaction with S-duct Trade Off

The three vortices create an inlet relative Mach number reported in Figure 8.53. As is possible to see the region near the hub has improve a lot but the outer region has the same distorsion as the trade off from the previous section. From the blade to blade view it important to notice that many blades are working with almost normal shock wave and from Figure 8.54 the velocity span wise has the velocities distorsion concentred on the bottom side of the fan.

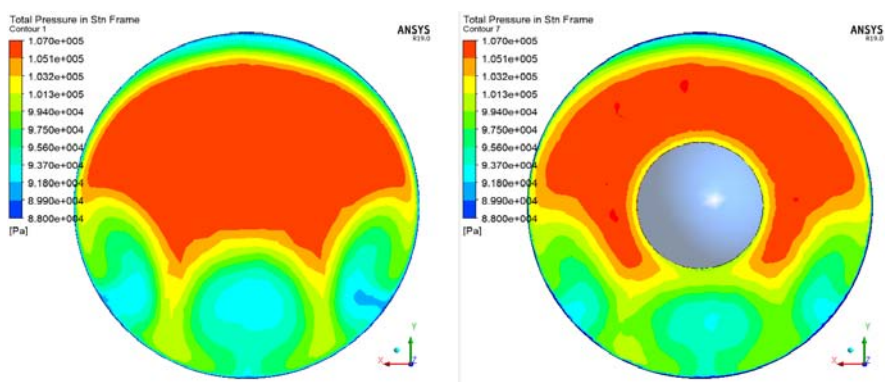


FIGURE 8.52: Total Pressure Contour at the Inlet (Left) and Outlet(Right)of the Ogive.

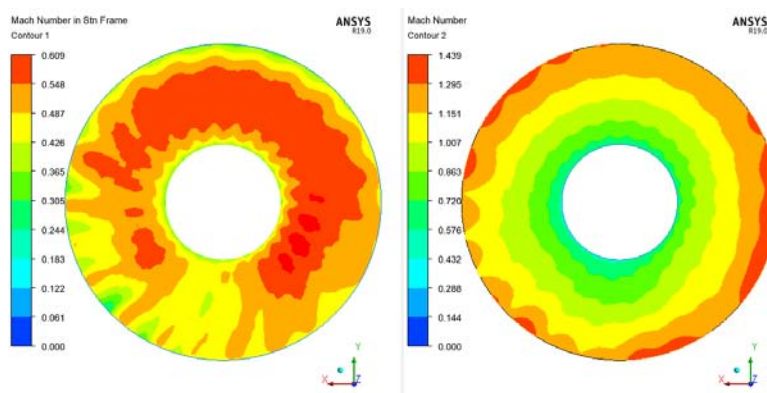


FIGURE 8.53: Inlet Mach Number Trade Off.

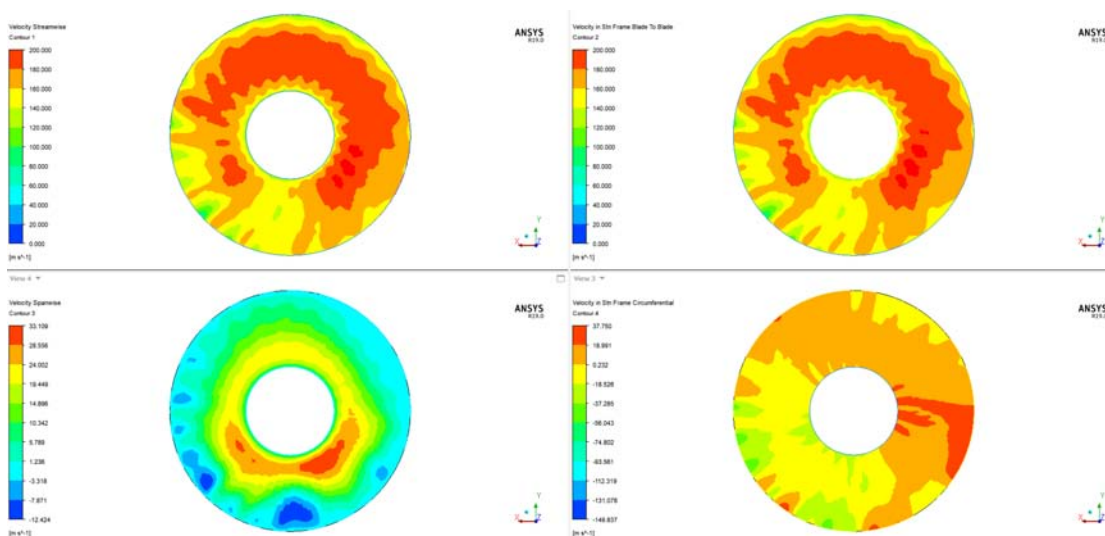


FIGURE 8.54: Streamiwise(Top Left),Blade to Blade Abs (Top Right), Spanwise(Bot Left), Crf Abs(Bot Right).

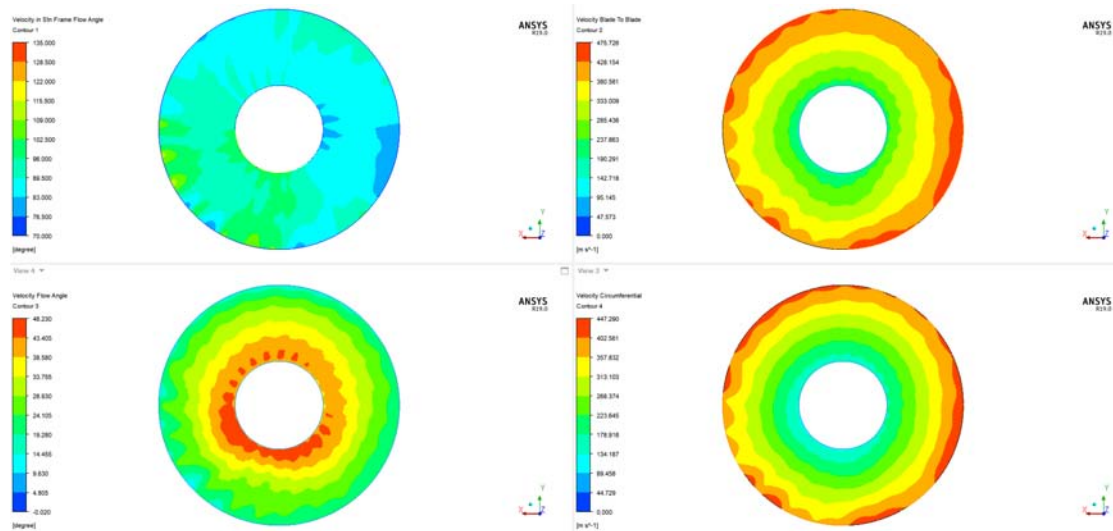


FIGURE 8.55: Flow Angle Abs(Top Left), Blade to Blade Rel(Top Right), Flow Angle Rel(Bot Left), Crf Rel(Bot Right).

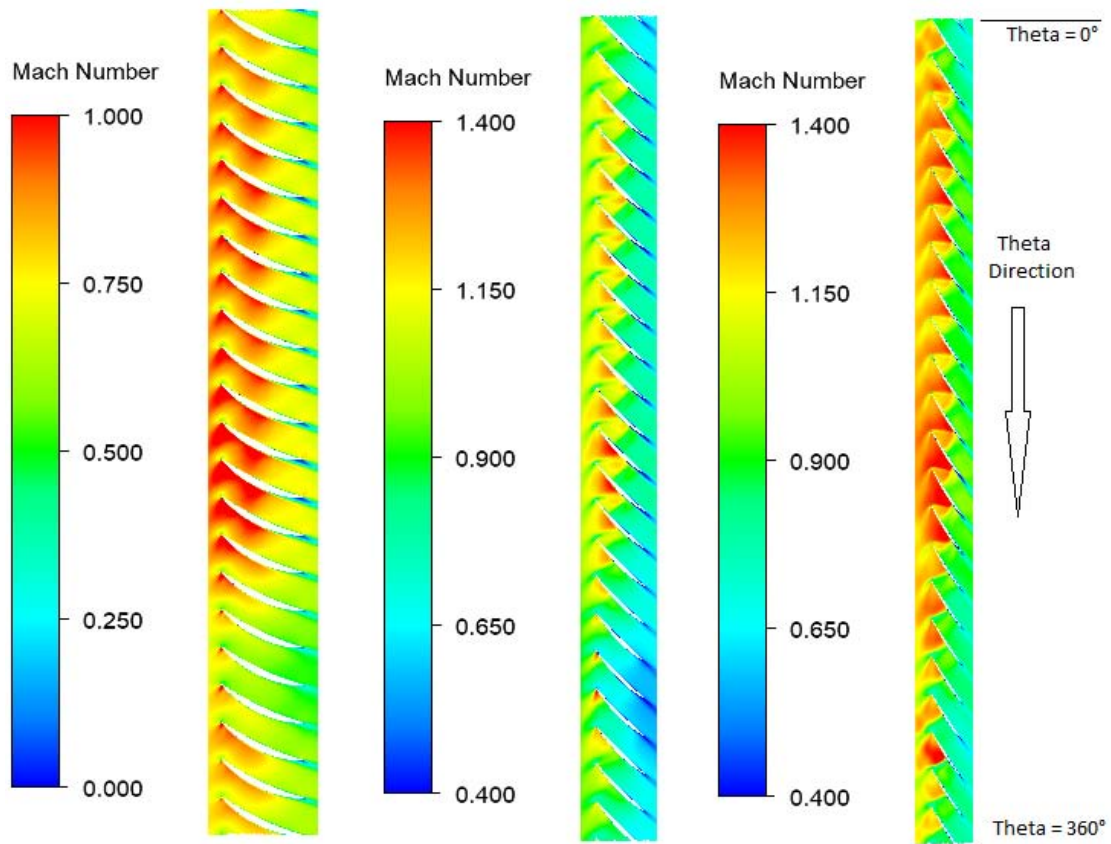


FIGURE 8.56: Blade-to-Blade span=0.2,0.5 and 0.8 Trade Off.

Chapter 9

Conclusions

The aim of the thesis was to understand the interactions between different S-ducts intake and a transonic fan. At the beginning, the first step was the study of the baseline geometry interaction. Since the high computational cost and in accordance with the previous work done by Marco [15] it was decided to simulate just one speed line and in particular the 95% of the rotational speed. The results show that the s-duct baseline drastically decrease the performance of the rotor 67. The baseline creates two counter rotating vortices in the low area of the duct leading to a formation of a low total pressure region. The two vortices, under the effect of the rotational speed of the fan, merge together in the ogive domain. The single vortex created on the bottom part of the fan creates a velocity inlet distortion that negatively affect the shock wave near the tip. After the baseline three different optimisation were conducted with a new objective function called S.M.E.. The new function proved to be successful in the reduction of the CP value. In Chapter 6 the different geometry of the optimisations are reported and compared. In particular the S.M.E. has the ability to create, in the first 5 cross-section, geometry with a wide and oval shape developed in the horizontal direction. The DC60 instead in the last 3 cross-section seems to create geometry with a rounded triangular shape. On the contrary, the swirl objective function creates inverse triangular shape that develop in the vertical direction. In the end in Chapter 8 are reported the CFD simulation of the optimised s-duct. The results show that the vortices structure affects in different way the performance of the fan. In particular the first 6 geometries (first two optimisation) show that the two big counter-rotating vortices increase the performance compared to the baseline. The increase in the performance depend on the vortex absolute and relative position.

In fact for the absolute position the best one seems to be the one with the two vortices positioned in the middle of the ogive (Best C_p). But also the relative position of the two vortices has to be taken into account. In fact, as proven on the seventh simulation (Best S.M.E.), the vortices have to be as far as possible. In fact, if the vortices have their core distance increased, the influence that the right vortex has on the left one is much less. To destroy the left vortex and start the merge phenomena, two main actors give their contribution. The first one is the rotational speed of the fan and it is constant for every s-duct simulation. The second one is the right vortex that acts stronger or weaker depending on the relative position of the two vortices and his position change depending on the s-duct shape. In the end the last two simulation show the 4 vortices interaction. The best swirl gives bad conditions to the fan but the trade off improves a lot the efficiency of the rotor.

Bibliography

- [1] Davide Dal Magro. Implementation of uncertainty management techniques in the design of s-ducts intakes. Master's thesis, Padova University, 2019.
- [2] John David Anderson Jr. *Fundamentals of aerodynamics*. Tata McGraw-Hill Education, 2010.
- [3] AM Abdel-Fattah and YY Link. Wind tunnel tests on jindivik air intake duct with and without an auxiliary intake. Technical report, AERONAUTICAL RESEARCH LABS MELBOURNE (AUSTRALIA),, 1992.
- [4] Ahmed F El-Sayed and Mohamed S Emeara. Intake of aero-engines: A case study.
- [5] Nicholas Fredrick and Milt Davis. Investigation of the effects of inlet swirl on compressor performance and operability using a modified parallel compressor model. In American Society of Mechanical Engineers, editor, *In ASME 2011 Turbo Expo: Turbine Technical Conference and Exposition*,, page pages 177–187, 2011.
- [6] L. Guglielmi. Aerodynamic s-duct intake shape multi-objective optimization for distributed propulsion. Master's thesis, Cranfield University, 2015.
- [7] Norbert C. Bissinger and Thomas Breuer. Basic principles–gas turbine compatibility–intake aerodynamic aspects. *Encyclopedia of Aerospace Engineering*, 2010.
- [8] F. Caruso. S-duct aerodynamics; evaluation of uncertainties for s-duct experimental campaigns. Master's thesis, Cranfield University, 2015.
- [9] Theodore H. Okiishi Steven R. Wellborn and Bruce A. Reichert. A study of the compressible flow through a diffusing s-duct. Technical report, National Aeronautics and Space Administration, 1993.

-
- [10] M. Barison. Shape optimization of highly convoluted intakes using genetic algorithms and metamodels. Master's thesis, Cranfield University, 2016.
- [11] E. Manca. Unsteady aerodynamic investigation of the flow within an optimized s-duct intake. Master's thesis, 2016.
- [12] A. Rigobello. A multi-objective shape optimization of an s-duct intake through nsga-ii genetic algorithm. Master's thesis, Cranfield University, 2016.
- [13] R. Tridello. Comparison of genetic and tabu search algorithms in aerodynamic design of s-ducts. Master's thesis, Padova University, 2017.
- [14] Pavlos Zachos Mark Savill Alessio D'Ambros, Timoleon Kipouros and Ernesto Benini. Computational design optimization for s-ducts. *Designs*, 2018.
- [15] Marco Tridente. Cfd study on the effect of a transonic fan downstream of an s-shape duct. Master's thesis, Padova University, 2019.
- [16] Meherwan P. Boyce. Axial flow compressor. *ResearchGate*, 2012.
- [17] Marco Danieli. Multi-objective aerodynamic optimization of a transonic axial compressor rotor. Master's thesis, Cranfield University, 2015.
- [18] A. Scaramuzzi. Extend the robust design optimisation for s-ducts considering more input and output uncertainties. Master's thesis, Padova University, 2020.
- [19] F. Glover and M. Laguna. Tabu search. *ResearchGate*, 1997.
- [20] C. Blum and A. Roli. Metaheuristics in combinatorial optimization: Overview and conceptual comparison. *ResearchGate*, 2003.
- [21] Xin-She Yang. Metaheuristic optimization. *ResearchGate*, 2011.
- [22] William N. Dawes Geoffrey T. Parks A. Mark Savill Timoleon Kipouros, Daniel M. Jaeggi and P. John Clarkson. Biobjective design optimization for axial compressors using tabu search. *AIAA journal*, 2008.